

The Mopra Southern Galactic Plane CO Survey — Data Release 3

Catherine Braiding^{1,8}, G. F. Wong^{1,2}, N. I. Maxted^{1,2}, D. Romano¹, M. G. Burton^{1,3}, R. Blackwell⁴, M. D. Filipović², M. S. R. Freeman¹, B. Indermuehle⁵, J. Lau⁴, D. Rebolledo^{6,7}, G. Rowell⁴, C. Snoswell⁴, N. F. H. Tothill², F. Voisin⁴, and P. de Wilt⁴

¹School of Physics, University of New South Wales, Sydney, NSW 2052, Australia

²School of Computing Engineering and Mathematics, Western Sydney University, Locked Bay 1797, Penrith, NSW 2751, Australia

³Armagh Observatory and Planetarium, College Hill, Armagh BT61 9DG, UK

⁴School of Physical Sciences, University of Adelaide, Adelaide, SA 5005, Australia

⁵CSIRO Astronomy & Space Science, Australia Telescope National Facility, PO Box 76, Epping, NSW 2121, Australia

⁶Joint ALMA Observatory, Alonso de Córdova 3107, Vitacura, Santiago, Chile

⁷National Radio Astronomy Observatory, 520 Edgemont Road, Charlottesville, VA 22903, USA

⁸Email: catherine.braiding@gmail.com

Abstract

We present observations of fifty square degrees of the Mopra carbon monoxide (CO) survey of the Southern Galactic Plane, covering Galactic longitudes $l = 300\text{--}350^\circ$ and latitudes $|b| \leq 0.5^\circ$. These data have been taken at 0.6 arcminute spatial resolution and 0.1 km s^{-1} spectral resolution, providing an unprecedented view of the molecular clouds and gas of the Southern Galactic Plane in the 109–115 GHz $J = 1\text{--}0$ transitions of ^{12}CO , ^{13}CO , C^{18}O and C^{17}O .

We present a series of velocity-integrated maps, spectra and position-velocity plots that illustrate Galactic arm structures and trace masses on the order of $\sim 10^6 \text{ M}_\odot$ per square degree; and include a preliminary catalogue of C^{18}O clumps located between $l = 330\text{--}340^\circ$. Together with information about the noise statistics of the survey these data can be retrieved from the Mopra CO website, the PASA data store and the Harvard Dataverse.

Keywords: Galaxy: kinematics and dynamics – Galaxy: structure – ISM: clouds – ISM: molecules – radio lines: ISM – surveys

1 INTRODUCTION

Since its astronomical discovery in 1970 (Wilson et al., 1970), the carbon monoxide (CO) molecule has been utilised as a key tracer of molecular gas in the Galaxy. Second in numerical abundance only to the H_2 molecule, the large abundance ($\sim 10^{-4}$) and low electric dipole moment (0.122 D) of CO allows cold molecular gas to be well-traced by the $J=1\text{--}0$ rotational transition. CO surveys of the molecular gas in the Galactic Plane can help shape an understanding of star formation, dynamics, and chemistry within the Milky Way.

The Mopra Galactic Plane CO survey¹ is the highest resolution large-scale 3-dimensional molecular gas survey of the inner Galactic Plane so far. With this paper, we

publicly release CO^2 , ^{13}CO and $\text{C}^{18}\text{O}(1\text{--}0)$ data³ for the region from $l = 300$ to 350° , and $b = \pm 0.5^\circ$ (see Figure 1). This release encompasses updated reductions of data contained within the previous Mopra CO data releases (Burton et al., 2013; Braiding et al., 2015) and, along with the Mopra CO maps of the Carina/Gum 31 region (Rebolledo et al., 2016) and the Central Molecular Zone (CMZ, Blackwell et al., 2018), will eventually be incorporated into a larger mosaic with coverage spanning longitude $l \sim 260$ to $+11^\circ$ and a latitudinal range of $\pm 1^\circ$. Additional targeted extensions beyond 1° will also be included.

²To avoid confusion we henceforth refer to this isotopologue as ^{12}CO , using ‘CO’ to refer to the molecule more generally.

³We have also surveyed the $\text{C}^{17}\text{O}(1\text{--}0)$ transition, but it is too weak to be detected above a $1\text{-}\sigma$ level over most of the surveyed region and will be excluded from our discussion; nevertheless the fully-reduced data is being made publicly available in DR3.

¹<http://newt.phys.unsw.edu.au/moprac/>

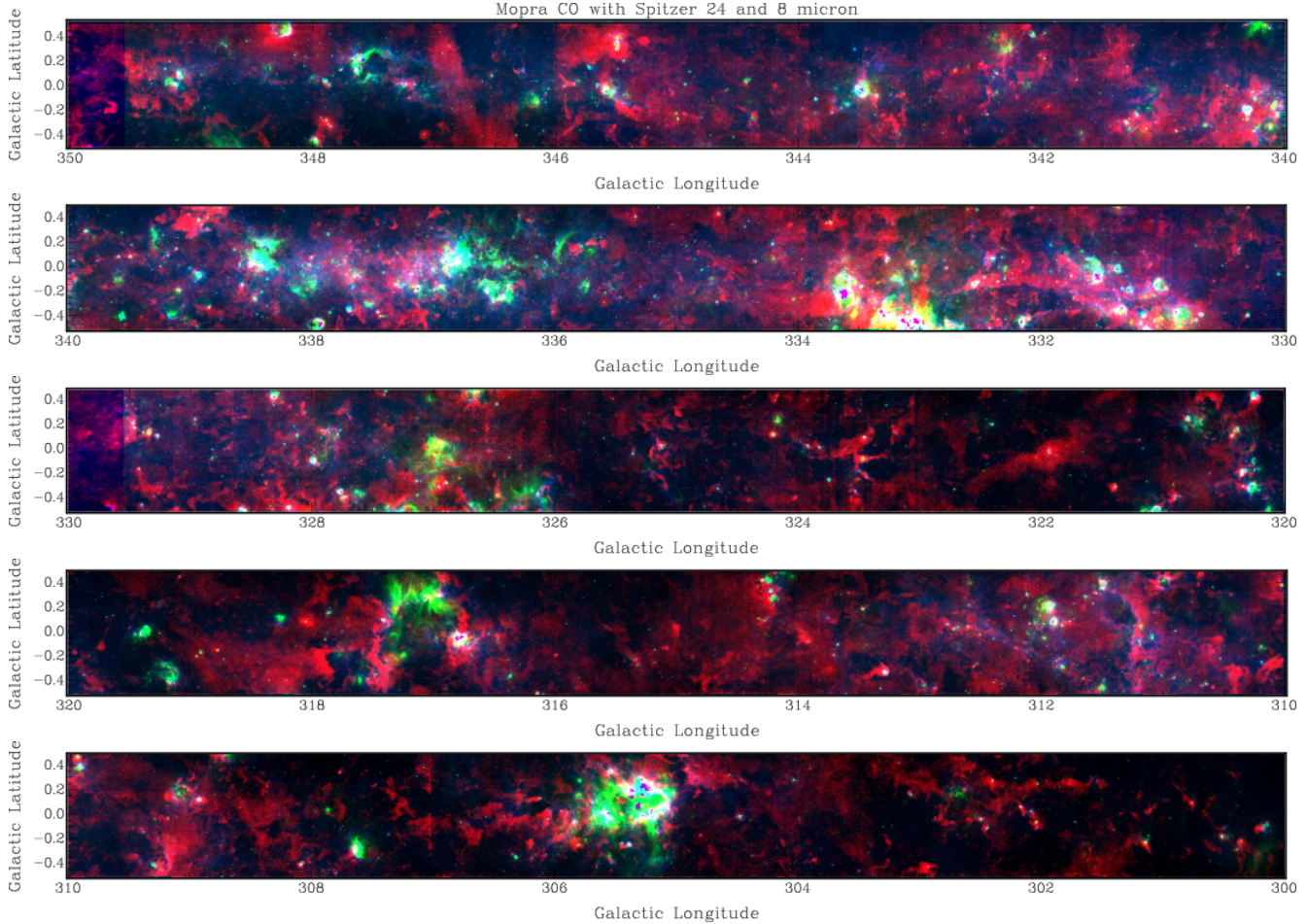


Figure 1. Three-colour image of the Galactic Plane from the Mopra CO survey (red; peak intensity image from $v = -150$ to $+50 \text{ km s}^{-1}$) together with the Spitzer MIPSGL 24 μm (green; Carey et al., 2009) and GLIMPSE 8 μm (blue; Churchwell et al., 2009; Benjamin et al., 2003) surveys.

The Columbia CO(1–0) survey (Dame et al., 2001) has been a revolutionary tool for the study of the Milky Way; its 8'-resolution has helped enable a large number of important astronomical results. Some examples include the constraining of the CO X-factor and Galactic cloud masses, the identification of Galactic structures (e.g. Dame & Thaddeus, 2011; Vallée, 2014) and implications for dark matter research (e.g. Drlica-Wagner et al., 2014).

The Mopra Galactic Plane CO survey will enable new Galactic science. ALMA offers arcsecond-level spatial resolution in the CO(1–0) transition (e.g. Mathews et al., 2013), and the very fine field of view of ALMA is well-complemented by a large sub-arcminute-scale map which can allow the identification of molecular gas components for observations. Furthermore, comprehensive investigations of the ‘missing’ gas of the Galaxy (as inferred from dust and gamma-ray observations, e.g. Planck Collaboration et al., 2015) require molecular clouds to be imaged at a resolution able to separate these ‘dark’

components, complementing observatories such as the Cherenkov Telescope Array (CTA, Cherenkov Telescope Array Consortium et al., 2017) and the High Elevation Antarctic Telescope (HEAT, Walker et al., 2004). Our survey also goes one step further than historical ^{12}CO surveys of the Galactic Plane by mapping multiple CO isotopologues that probe the regions where CO(1–0) becomes optically thick, tracing additional mass components.

In this paper, we present 50 square degrees of Mopra ^{12}CO , ^{13}CO , C^{18}O and C^{17}O data⁴. Section 3 is an update on the data-processing techniques used by the survey, descriptions of the data quality, and a list of regions affected by contaminated reference positions. A series of images and characterisations of Mopra data are presented in Section 4 alongside a new catalogue of C^{18}O clumps located within the region $l = 330\text{--}340^\circ$. Finally, we outline recent region and source-specific investigations that utilise Mopra CO isotopologue data

⁴available at doi:10.7910/DVN/LH3BDN

and propose additional work to be performed, in conjunction with other surveys, to determine the evolution of molecular clouds, and the origins of cosmic rays (Section 5 & 6).

2 PREVIOUS DATA RELEASES

The Mopra CO Galactic Plane survey was first described in Burton et al. (2013), which presented the results of the pilot observations undertaken in March 2011 of the single square degree, $l = 323\text{--}324^\circ$, $b = \pm 0.5^\circ$. The aims and the approach of the Mopra CO survey were also discussed in detail, with science goals of comparing the emission of Gamma and Cosmic rays to emission from nearby molecular clouds, and characterising the formation of molecular clouds. The initial observations were used to describe a number of giant molecular clouds along the G323 line of sight, demonstrating how the multiple isotopologue CO survey data could be used in conjunction with HI data from the Southern Galactic Plane Survey (SGPS; McClure-Griffiths et al., 2005) to determine the mass and column densities within these clouds. This data remains some of the noisiest in the Mopra CO survey (see Figures 2–4), as the initial observations were conducted during summer months.

The first data release by Braiding et al. (2015, hereafter DR1), presented the first ten degrees of the Mopra CO Survey, covering Galactic longitudes $l = 320\text{--}330^\circ$ and latitude $b = \pm 0.5^\circ$, and $l = 327\text{--}330^\circ$, $b = -0.5\text{--}+1.0^\circ$. The maps possessed a typical rms noise of ~ 1.2 K in the ^{12}CO data and ~ 0.5 K in the other isotopologue frequency bands. It was noted that the line intensities from the Mopra CO survey are ~ 1.3 times higher than those of Dame et al. (2001, see also §4.1), although the average line profiles for each square degree show similar qualitative features. The calculated mass of the molecular clouds in the ten square degrees of DR1 was found to be $\sim 4 \times 10^7 M_\odot$, and included many complex filamentary structures from the tangent point to the Norma spiral arm of the Galaxy. Data release 3 contains an improved reduction of these ten square degrees, and although the changes are very minor ($\sim 1\%$ of voxels differ from their previous values, most by $\ll 0.1$ K), it is recommended that current Mopra CO users download the newer files for future work.

Data release 2 (DR2; Rebollo et al., 2016) comprised 8 square degrees of observations covering the Carina Nebula and Gum 31 molecular complex. In addition to the molecular gas distribution derived from ^{12}CO and ^{13}CO line emission maps, this paper presented total gas column density and dust temperature maps. The Mopra CO data were complemented by dust maps from Herschel (Molinari et al., 2010), allowing the calculation of dust column densities within the nebula of between 6.3×10^{20} and $1.4 \times 10^{23} \text{ cm}^{-2}$, and dust temperatures within a range of 17 to 43 K. The distribution of the

total gas is well represented by a lognormal function, but a tail at high densities is clearly observed, which is a common feature of nebulae with active star formation (Pineda et al., 2010; Rebollo et al., 2016). Regional variations in the masses recovered from the Mopra CO emission and Herschel dust maps revealed the different evolutionary stages of the molecular clouds that comprise the Carina Nebula–Gum 31 complex.

The Central Molecular Zone (CMZ) of the Galaxy contains dense (e.g. Jones et al., 2012, 2013), high-temperature (e.g. Ao et al., 2013) molecular clouds with a total cumulative mass of $\sim 5 \times 10^7 M_\odot$ (e.g. Pierce-Price et al., 2000). The fourth data release of the Mopra CO Survey will cover the Galactic Centre region ($358.5 \leq l \leq 3.5^\circ$, $-0.5 \leq b \leq +1.0^\circ$; Blackwell et al., 2018), which has required the development of new observing and data processing techniques to produce high quality spectral maps. As the star formation behaviour of molecular clouds in the CMZ is linked to their orbital dynamics (e.g. Kruijssen et al., 2015), the high resolution Mopra CO maps will enable new studies of the inner Galaxy gas dynamics and triggered star formation.

3 DATA RELEASE 3

Observations for this data release were carried out over the Southern Hemisphere winters of 2011–2016 using Mopra, a 22 m single-dish radio telescope located ~ 450 km north-west of Sydney, Australia (at $31^\circ 16' 04''$ S, $149^\circ 05' 59''$ E, 866 m a.s.l.). Observations utilised the UNSW Digital Filter Bank (the UNSW-MOPS) in its ‘zoom’ mode, with 8×137.5 MHz dual-polarization bands. These bands were tuned to target the $J=1-0$ transition of ^{12}CO , ^{13}CO , C^{18}O and C^{17}O (with central frequencies of 115271.202, 110201.354, 109782.176 and 112358.988 MHz, respectively). Three bands were tuned to sample a $\text{CO}(1-0)$ velocity coverage of $\sim 1,100 \text{ km s}^{-1}$, while the $^{13}\text{CO}(1-0)$ and $\text{C}^{18}\text{O}(1-0)$ transitions each had two dedicated bands to sample a velocity-coverage of $\sim 770 \text{ km s}^{-1}$. One band was allocated to the least-abundant molecular transition, $\text{C}^{17}\text{O}(1-0)$, resulting in $\sim 380 \text{ km s}^{-1}$ of velocity coverage. The targeted central frequencies were offset according to Galactic Longitude to maximise overlap with expected Galactic rotation velocities. As in DR1, the observations from $l = 323\text{--}331^\circ$, $b = \pm 0.5^\circ$ cover a smaller velocity range, as only 4 ‘zoom’ bands were utilized during the 2011 observing period, one for each isotopologue. Our observations across the full 50 square degrees of DR3 suggest that it is unlikely that there are any high-velocity clouds in this region, as all of the ^{12}CO clouds detected to date have been within the velocity range of the primary zoom band.

As described in Burton et al. (2013), Fast-On-The-Fly (FOTF) mapping has been carried out in 1 square degree segments, with each segment being comprised of orthogonal scans (in longitudinal and latitudinal directions) to

reduce scanning artefacts. The exposure of each square degree is at least ~ 20 hrs, more in places where poor weather or technical issues interrupt observations and triggered a repeat of the affected scans.

The angular resolution of the Mopra beam at 115 GHz is 33-arcsec FWHM (Ladd et al., 2005); after a median filter convolution is applied during the data reduction process, the dataset possesses a beam size of around 0.6 arcmin. Since the survey region is spatially fully-sampled, the extended beam efficiency, $\eta_{XB} = 0.55$ at 115 GHz, should be used to convert brightness temperatures into line fluxes (rather than the main beam efficiency $\eta_{MB} = 0.42$; Ladd et al., 2005).

DR3 has been made available at the survey website and in the PASA data archive as a series of fits files covering a square degree for each isotopologue, separated by half a degree along the Galactic Plane. Although the full range of velocity space available for ^{12}CO is $[-1000, +1000] \text{ km s}^{-1}$ (with file sizes of ~ 800 MB per square degree), it is expected that most users would prefer to download the smaller (~ 300 MB per square degree) files covering the velocity range $[-150, +50] \text{ km s}^{-1}$ illustrated in this paper. No emission has as yet been detected outside this range, although closer to the Galactic centre this range will be extended. Also available are the T_{sys} , beam coverage and RMS noise images for each line.

3.1 Data Processing

From September 2015 observations were affected by a recurring synchronisation loss between the telescope and spectrometer, creating a spike in the central channel of $\sim 0.03\%$ of spectra. This was not automatically flagged by software during observations or using the data reduction processes from DR1 and DR2, and if left unchecked these artefacts would propagate throughout the reduction, particularly when spikes appeared in the sky reference spectra. A new IDL routine was created to mask the affected channels in the raw data from the telescope; by coincidence this also flags other poor spectra caused by clouds or system fluctuations.

The rest of the data reduction remains unchanged from DR1 and DR2, involving six main stages of processing (Braiding et al., 2015; Rebolledo et al., 2016). Firstly, **LIVEDATA**⁵ (Gooch, 1996) was used to perform the band-pass correction and background subtraction using data from the nearest reference position to create the calibrated spectra. These are then analysed using an IDL routine that flags any spectra that are poorly-calibrated or particularly noisy (mostly in the ^{12}CO bands where the system temperature is higher). The data are then interpolated onto a uniform grid using

GRIDZILLA (Gooch, 1996), employing a median filter for the interpolation of the oversampled data onto each grid location. **GRIDZILLA** excludes from the grid those spectra for which the T_{sys} values are above 1000 K for the ^{12}CO cube, and 700 K for the other lines (see §3.2). The output of these processes is a **fits** data cube in (l, b, V_{LSR}) coordinates.

Noisy outlier pixels, rows and columns are then cleaned using an IDL routine that first detects voxels that differ from their neighbours by more than 5 standard deviations, then rows and columns where the mean spectra differs by more than 3 standard deviations from the median of the entire data set (typically caused by the passage of clouds during the sky reference measurement). These ‘bad’ data are replaced by interpolating the values of their neighbouring pixels, as described in Burton et al. (2013), and the process is repeated until no further ‘bad’ data are detected.

The data are then continuum-subtracted using first a fourth-order and then a seventh-order polynomical fit, to yield data cubes of the brightness temperature for each spectral line as a function of Galactic coordinate and V_{LSR} velocity. Finally, data cubes that have been affected by contamination from faint molecular clouds present within the reference position (see §3.3), are corrected by modelling the contaminant component and adding that back into the final clean spectrum (Braiding et al., 2015).

3.2 Data Quality

The observations for DR3 were carried out over a wide variety of weather conditions, ranging from those of late Southern Hemisphere summer (March, 2011, 2014, and 2015) when the system temperature was high (~ 900 K for ^{12}CO) to deep winter (2011–2016) where the conditions are quite stable and T_{sys} in the ^{12}CO band is quite stable at around 400 K. This is reflected in the noise maps of the ^{12}CO , ^{13}CO , and C^{18}O data, which are presented in Figures 2, 3, and 4 respectively. The noise value for each pixel was determined from the standard deviation of the continuum channels for line-of-sight velocities containing no apparent signal. The thick striping seen within these maps is an effect of scanning in l and b directions under different system temperatures and observing conditions. Thinner stripes and spots of low noise indicate the positions of ‘bad’ pixels, rows, or columns that were identified and interpolated over (see §3.1; Burton et al., 2013).

The system temperature of Mopra (T_{sys} , discussed further in Appendix A.2) reflects the total level of signal received from the instrument, telescope, and sky, in addition to that from the source (which contributes a near-insignificant portion to T_{sys}). It is calibrated with reference to an ambient temperature paddle every 30 minutes, allowing us to control for variations in the

⁵Both **LIVEDATA** and **GRIDZILLA** can be downloaded from: www.atnf.csiro.au/computing/software/livedata/index.html

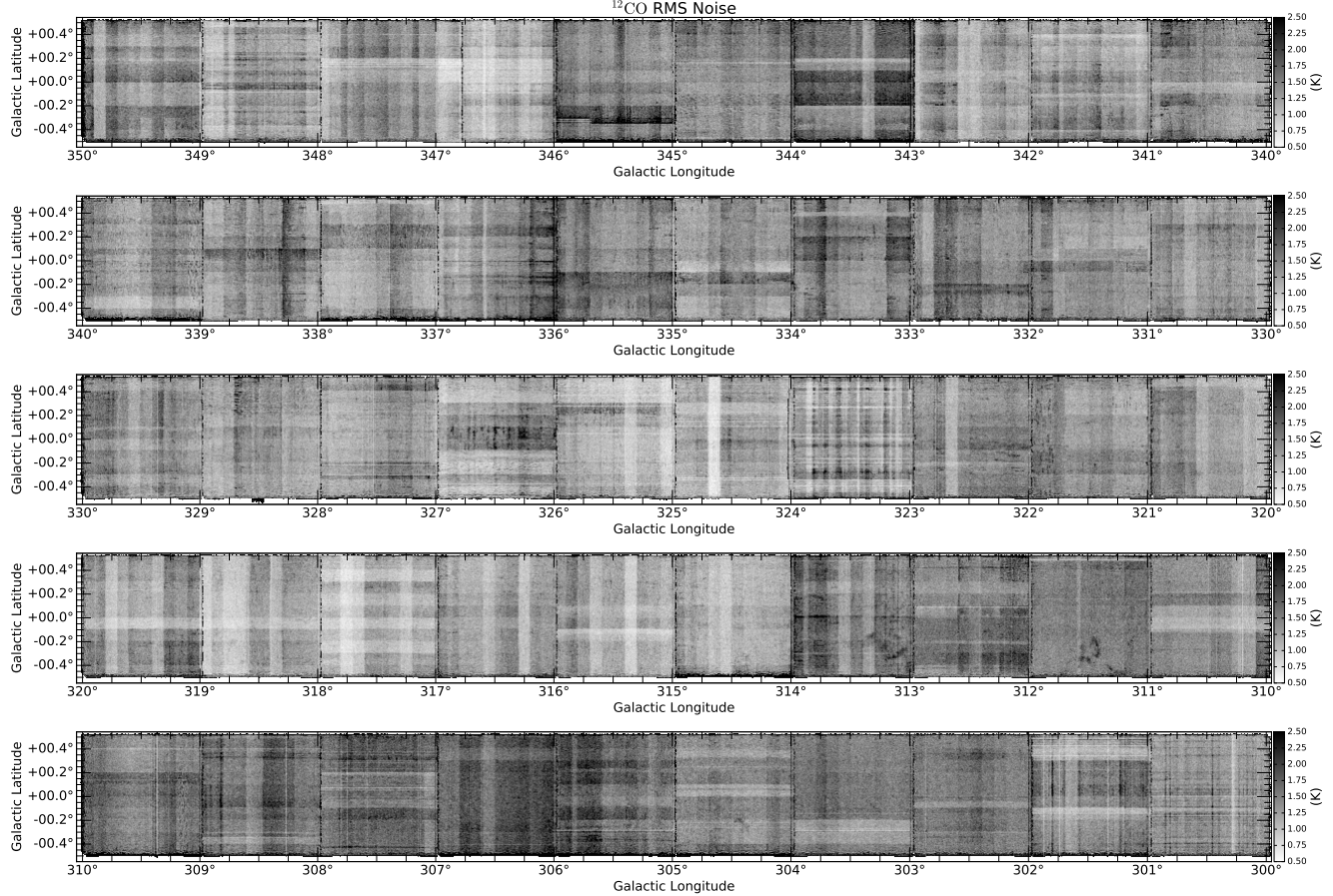


Figure 2. 1σ noise images for the ^{12}CO data covering the full 50 square degrees from $l = 300\text{--}350^\circ$ in units of T_A^* (K) (as indicated by the scale bars). The striping pattern is inherent to the data set, resulting from scanning in the l and b directions in variable observing conditions.

weather. Observations with an average T_{sys} greater than 1000 K were repeated under better weather conditions, while any individual measurement which possessed a T_{sys} greater than 1000 K was filtered out during the imaging stage of the data reduction (see §3.1).

To examine the Mopra beam resolution, observations of SiO(2-1, $v=1$) maser emission from the red supergiant variable star, AH Scorpii, were taken in November 2017 (Figure 9 in §A.1). The data were integrated over all masers in velocity-space, and gaussian line profiles were fitted to the diametral distribution in both right-ascension and declination. The measured FWHM was then deconvolved with the map smoothing by subtracting the smoothing kernel FWHM in quadrature. The resultant Mopra beam FWHM was calculated to be $35'' \pm 1''$ and $34'' \pm 1''$ for the Mopra beam axis at 86 GHz. This is consistent with previous calibration measurements that characterised the Mopra beam FWHM as $36'' \pm 3''$ (Ladd et al., 2005).

3.3 Sky Reference Positions

Table 1 lists coordinates of the sky reference positions used for each square degree of observations. Several of these reference positions contained ^{12}CO , ^{13}CO and in at least one instance C^{18}O line emission, which propagate into the data cubes as negative ‘‘emission’’. The line of sight velocity and peak intensity of the reference position ^{12}CO line emission are included in Table 1; the ^{13}CO line emission is typically fainter than the ^{12}CO line by a factor of 5, and similarly C^{18}O emission is only detected when the ^{12}CO contamination is exceptionally bright.

As mentioned in §3.1, data affected by contaminated reference positions are corrected in the last stage of data processing. An area of the cube which does not contain emission within $\pm 2 \text{ km s}^{-1}$ of the contamination is averaged and a gaussian profile is fitted to the spectrum, creating a clean model of the line emission at the reference position. The gaussian profile is then subtracted from each pixel, taking into account frequency shifts relating to Doppler tracking corrections across the cube. In some instances when the observations have been

Table 1 Sky reference beam positions for each square degree of DR3. Several cubes were contaminated by negative ^{12}CO , ^{13}CO and C^{18}O line emission from the sky reference position; the central velocity and intensity (in T_A^* [K] units) of the ^{12}CO contamination are noted here.

Cube	Reference Longitude	Reference Latitude	Contamination Velocity (km s^{-1})	Contamination Peak Intensity (T_A^* [K])
G300	300.500	+2.000		
G301	301.375	+2.375		
G302	302.875	-1.875	-6.2	-0.7
G303	303.000	-2.000	-5.4	-0.5
G304	304.000	-2.000		
G305	305.000	-2.000		
G306	306.000	-2.000	+38.3	-0.3
G307	307.500	-2.500	-46.2	-0.6
G308	309.000	-2.120		
G309	309.375	-2.500		
G310	310.500	-2.500		
G311	311.000	-2.500		
G312	312.500	-2.500		
G313	313.500	-2.500		
G314	314.875	-2.000	-4.9	-0.4
G315	315.500	-2.000		
G316	316.500	+2.000		
G317	318.000	+2.000		
G318	318.750	-2.000		
G319	319.000	-2.125	-22.9	-0.3
G320	320.375	-3.000		
G321	321.500	-2.500	-1.7	-3.2
G322	322.500	-2.000	-56.1, -13.0	-1.3, -0.4
G323	323.500	-2.000		
G324	324.500	-2.000	+0.9	-0.8
G325	325.500	-2.200	-46.6	-0.5
G326	326.500	-2.000	-19.5	-0.3
G327	327.500	-2.200		
G328	328.500	-2.200	+2.7	-0.4
G329	329.500	-2.200		
G330	329.500	-2.200		
G331	331.500	-2.000		
G332	332.500	-2.000		
G333	333.500	-2.000		
G334	333.500	-2.000		
G335	333.500	-2.000		
G336	336.500	-4.500	-61.8	-0.46
G337	337.500	-2.600		
G338	337.500	-2.600		
G339	339.500	+2.000		
G340	339.500	+2.000		
G341	342.500	-3.000	-0.89	-0.26
G342	342.500	-3.000	-10.1	-0.22
G343	343.500	+2.500		
G344	344.500	+3.000		
G345	345.635	-3.125	-18.7, -28.4	-0.81, -0.63
G346	346.250	-3.000		
G347	347.500	+2.625		
G348	349.250	-2.000		
G349	349.250	-2.000		

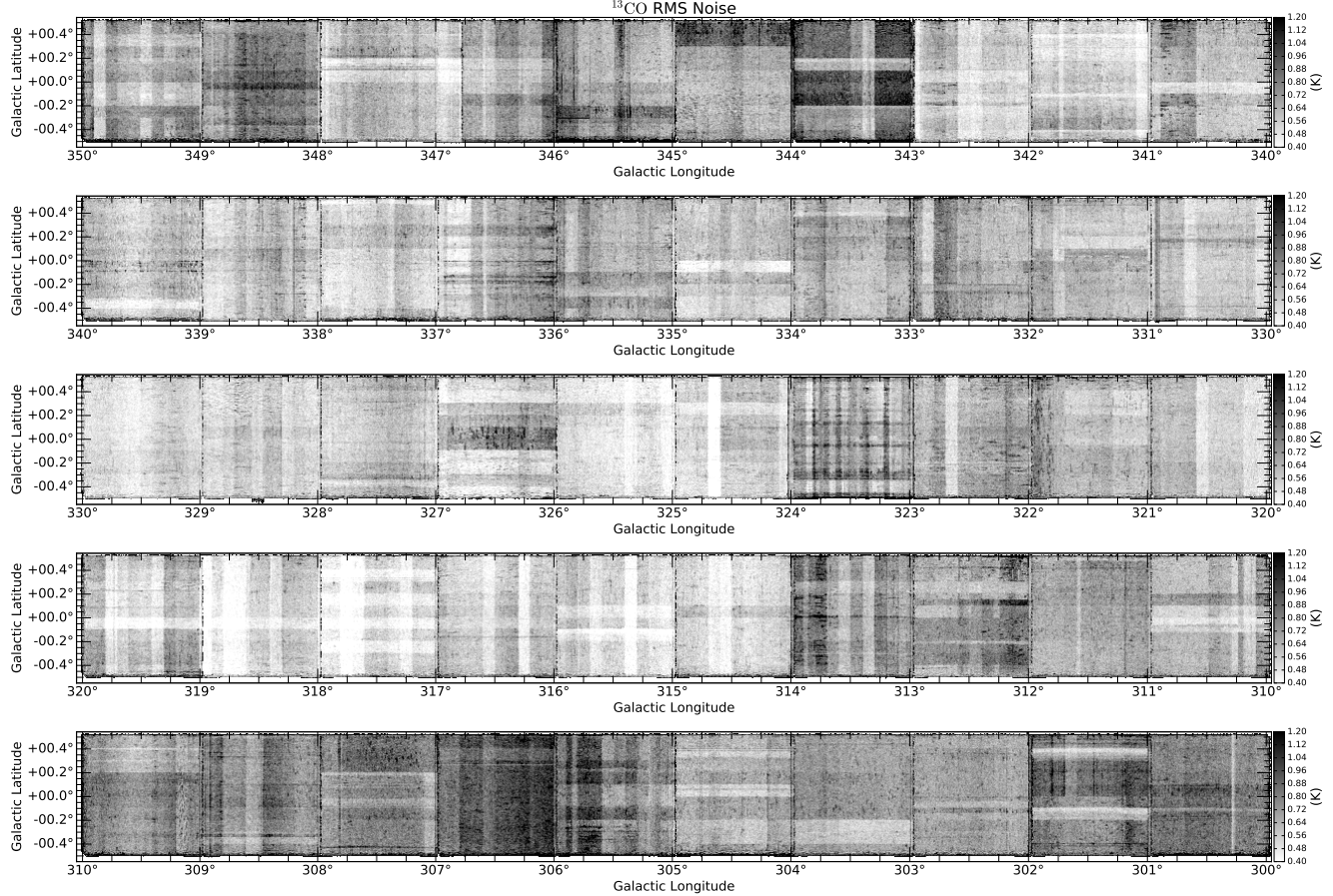


Figure 3. As in Figure 2, these are the 1σ noise images for the ^{13}CO data covering the full 50 square degrees from $l = 300\text{--}350^\circ$ in units of T_A^* (K) (as indicated by the scale bars).

taken many months apart and the Doppler corrections are large, the data are processed into separate cubes for each time period, and these are combined into a single cube after the reference contamination has been corrected. This technique was developed in response to reference-contaminated Mopra CO spectra from the Central Molecular Zone (CMZ, Blackwell et al., 2018).

4 RESULTS

We present here images from DR3, comparing the increased resolution of Mopra CO data to the lower spatial (8 arcmin) and spectral (1.3 km s^{-1}) resolution Columbia survey (Dame et al., 2001). We note consistent features between the two CO datasets, and illustrate the structure of the Milky Way through a series of position-velocity and mass-distribution plots.

4.1 Spectra & Moment Maps

The average line profiles of ^{12}CO and ^{13}CO for each central square degree of the Mopra Southern Galactic

Plane CO survey between longitudes 300° and 350° are presented in Appendix A.3. The ^{12}CO average spectra from the Dame et al. (2001) CO survey are included for comparison and are consistent with the features of Mopra CO survey data. We note a systematic shift in the brightnesses between the Mopra and Columbia surveys of a factor of ~ 1.35 as discussed in Braiding et al. (2015), which is calculated per square degree in Table 2 of Appendix A.3. The same shift is also apparent in the Nanten2 CO Survey data, which has very similar fluxes to the Mopra CO Survey (H. Sano, March 2017, private communication).

Integrated intensity maps from DR3 are presented in Appendix A.4, calculated over an interval of 10 km s^{-1} in the velocity range of -150 to $+50 \text{ km s}^{-1}$. We note similar features to those present in the Columbia CO survey (Dame et al., 2001), but also scanning artefacts of 1° -long line features in longitude or latitude near the edges of individual square degrees.

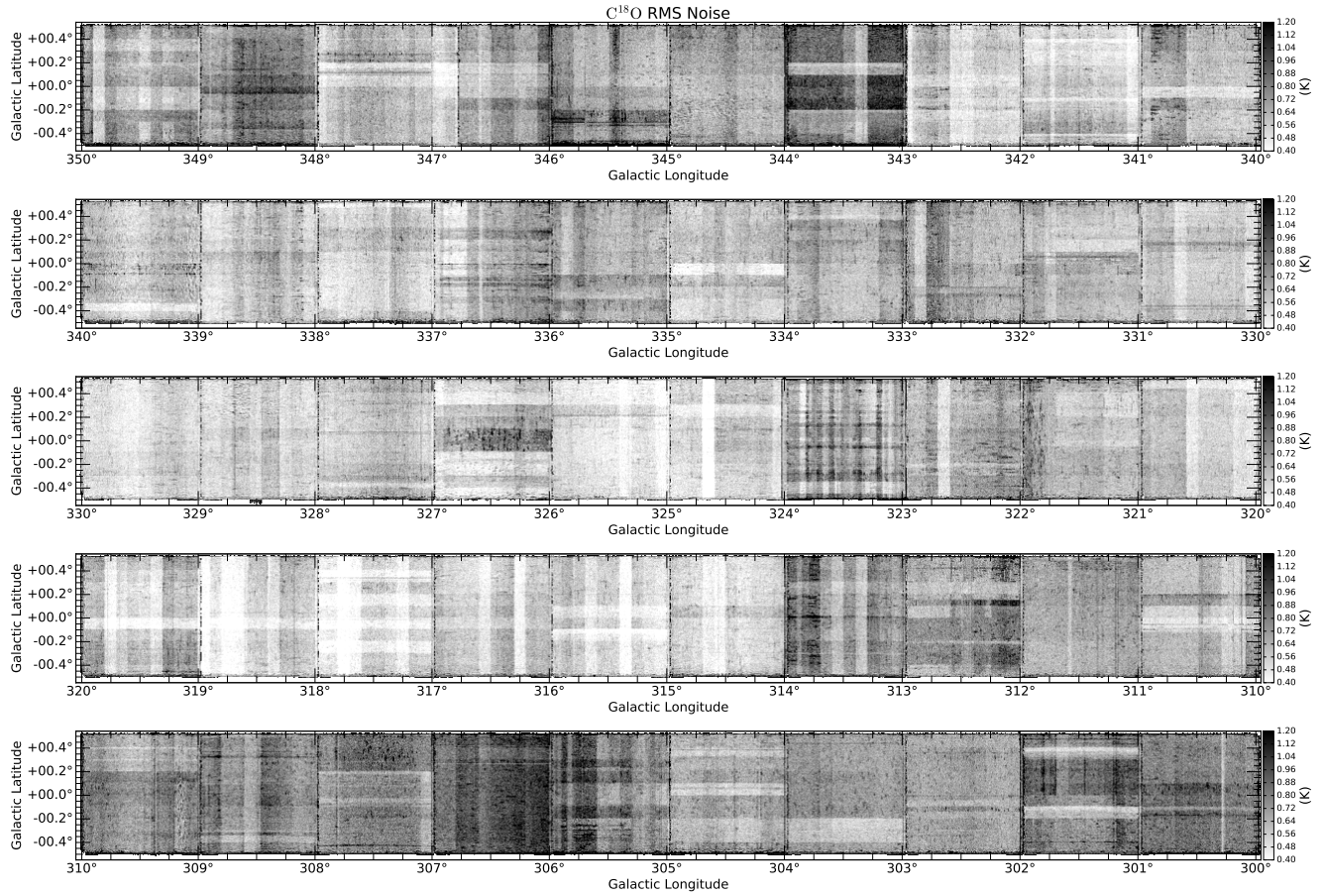


Figure 4. As in Figure 2, these are the 1σ noise images for the C^{18}O data covering the full 50 square degrees from $l = 300\text{--}350^\circ$ in units of T_A^* (K) (as indicated by the scale bars).

4.2 Velocity & Mass Distribution

Figures 5 and 6 show position-velocity (PV) slices of the CO emission averaged over 4 different ranges in latitude overlaid with the positions of four spiral arms from the Galaxy model of (Vallée, 2016, i.e. a pitch angle of 13.1° , central bar length of 2.2 kpc inclined at -30° to our sightline, Galactic Centre distance of 8.0 kpc and a flat rotation curve with velocity 220 km s^{-1}). Figure 5 shows the central plane $|b| < \pm 0.05^\circ$ and the entire data range of $|b| < \pm 0.5^\circ$, while Figure 6 shows the very top ($b = +0.4$ to $+0.5^\circ$) and bottom ($b = -0.5$ to -0.4°) of the surveyed field. The spiral arm model and its associated distance-velocity relationship are shown in Figure 7.

The observed features generally correspond to giant molecular cloud complexes within the spiral arms, with their velocity widths corresponding to internal motions within the complexes rather than the differential distances that could be inferred by applying a Galactic rotation model. In a few instances prominent outflows are evident as molecular emission that is quite extended in velocity but narrow in the longitudinal direction; these

could also be giant molecular clouds at far Galactic distances, but such clouds are generally expected to be somewhat extended in longitude.

However, while the molecular gas does tend to follow the trajectory of the spiral arm model in Figure 7, the detailed agreement is only modest. The differences between the PV-plots for the different latitude ranges are also striking, showing how discrete molecular gas is even within the Galactic Plane. Little $^{12}\text{CO}(1\text{--}0)$ emission is evident at ‘forbidden’ velocities, i.e. those that are more negative than the tangent point velocity at each latitude, and in particular the most negative velocities for each of the 4 model spiral arm positions.

Figure 8 shows the distribution of molecular mass with Galactic longitude, averaged for each square degree of the survey range. This calculation is as in Braiding et al. (2015) for $l = 320\text{--}330^\circ$, now extended to $l = 300\text{--}350^\circ$ and covering the entirety of DR3: applying the CO X-factor to convert ^{12}CO flux to column density using a conversion factor of $2.7 \times 10^{20} \text{ cm}^{-2} (\text{K km s}^{-1})^{-1}$, the value derived for $|b| < 1^\circ$ in Dame et al. (2001). Though larger than the $1.8 \times 10^{20} \text{ cm}^{-2}$ commonly used

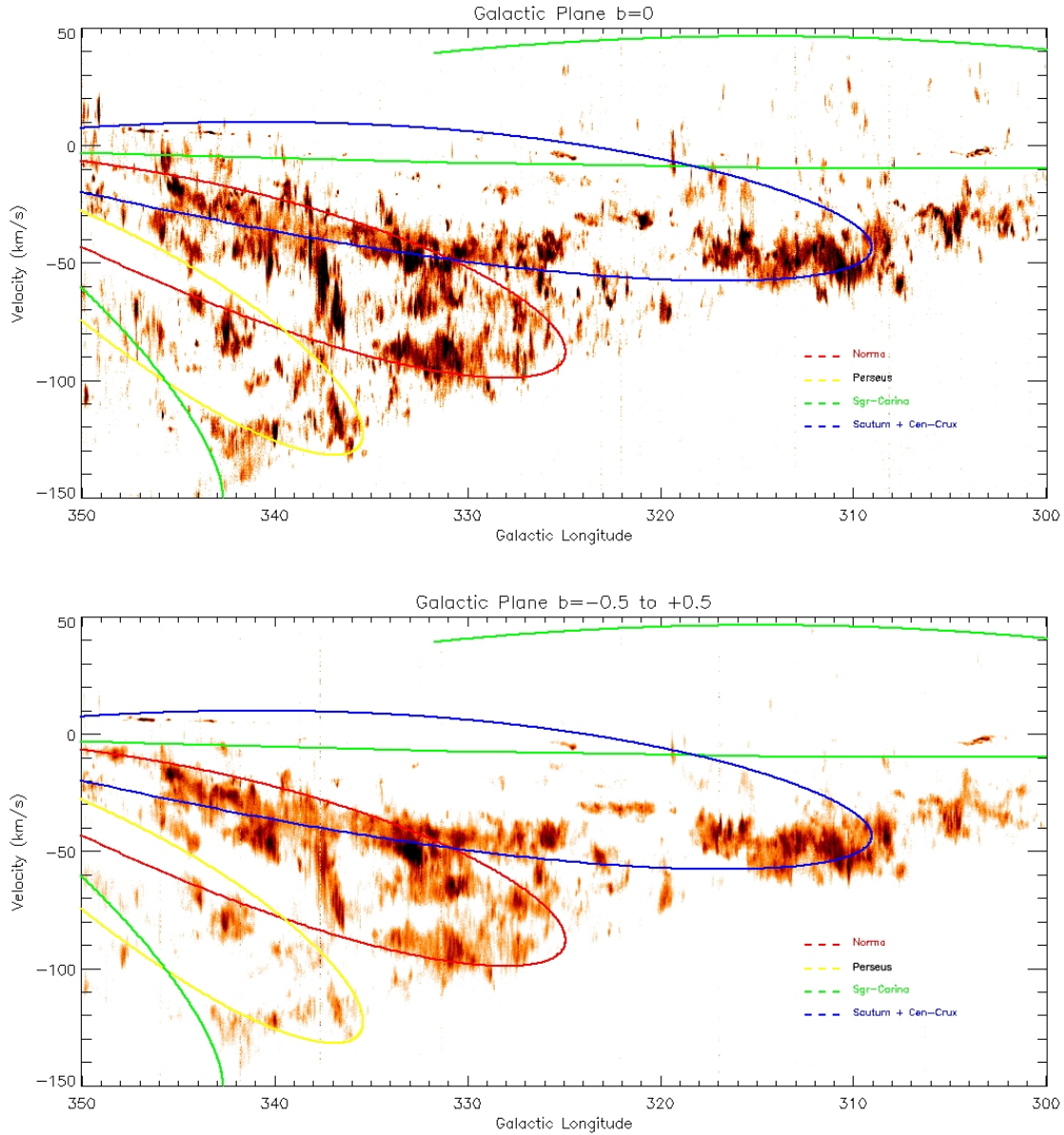


Figure 5. ^{12}CO position-velocity plots as a function of Galactic longitude. l is on the x -axis, V_{LSR} (the radial velocity) in km s^{-1} is on the y -axis. The data has been averaged between latitudes $b = -0.05^\circ$ and $+0.05^\circ$ (top) and $b = -0.5^\circ$ to $+0.5^\circ$ (bottom), respectively representing the midpoint of the plane and the entire surveyed plane. The solid lines are the model positions for the centres of the four spiral arms in the model of Vallée (2016). Note also that some artefacts are visible as features extending across the entire velocity direction, resulting from residual systematic effects.

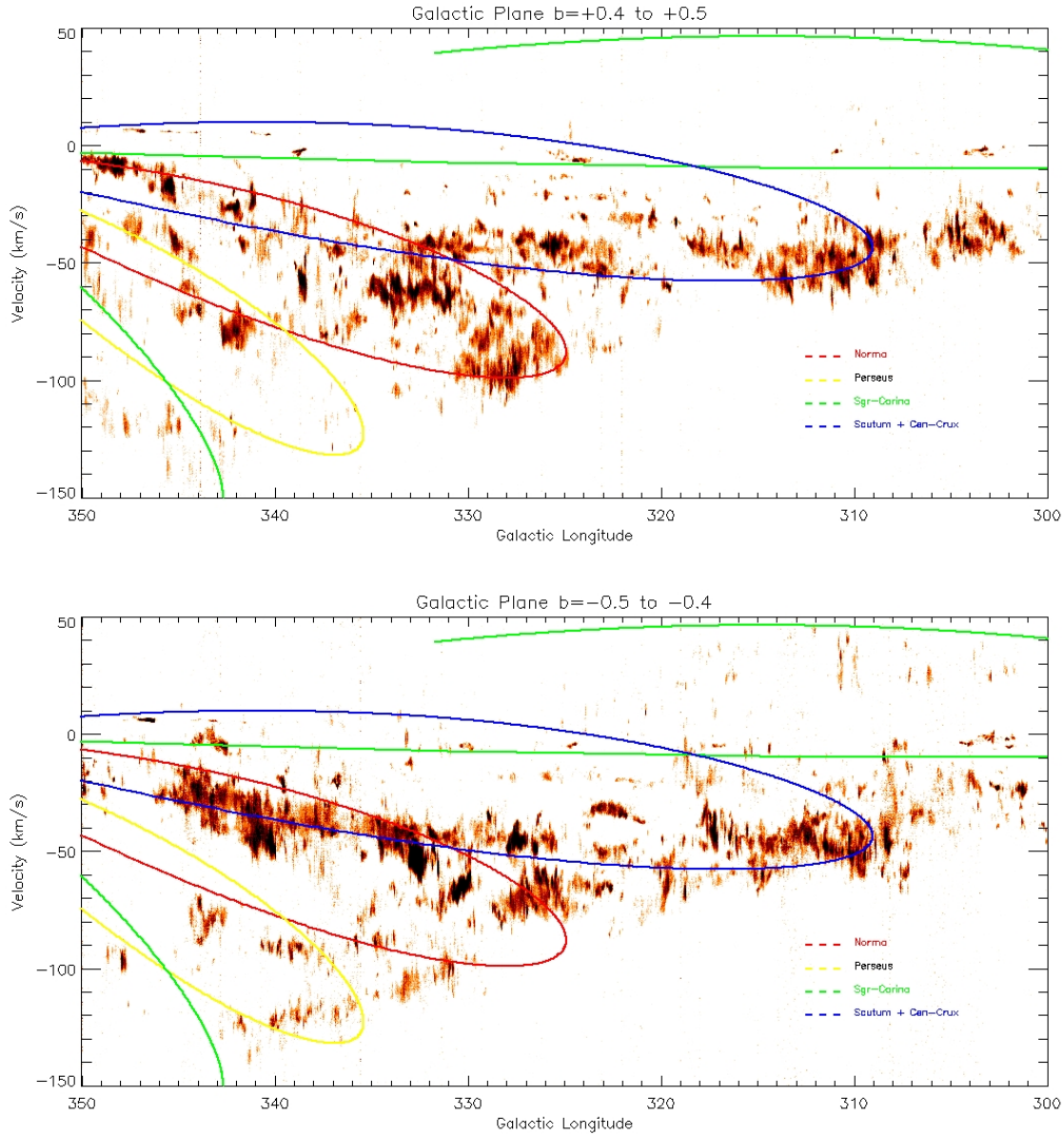


Figure 6. ^{12}CO position-velocity plots as a function of Galactic longitude, l , on the x -axis and the radial velocity, V_{LSR} , in km s^{-1} on the y -axis. The data has been averaged between latitudes $b = +0.5^\circ$ and $+0.4^\circ$ (top) and $b = -0.5^\circ$ to -0.4° (bottom), respectively representing the top and the bottom of the surveyed plane. The solid lines are the model positions for the centres of the four spiral arms in the model of Vallée (2016). Note also that some artefacts of residual systematic effects are visible as features extending across the entire velocity direction.

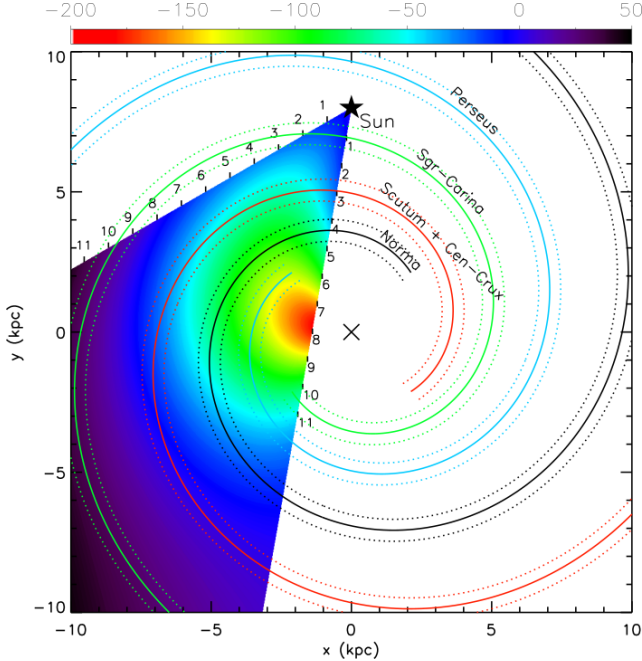


Figure 7. A schematic of the 4 spiral arms of the Milky Way Galaxy. Arm names, the Galactic Centre, and the location of the Sun are indicated. A colour-scale displays the expected kinematic line-of-sight velocity from the reference point of the Sun. The Galaxy is modelled as having a pitch angle of 13.1° , a central bar length of 2.2 kpc inclined at -30° to our sightline, a Galactic Centre distance of 8.0 kpc and a flat rotation curve with velocity 220 km s^{-1} (Vallée, 2016).

for $|b| < 5^\circ$, it is within the uncertainties discussed by Bolatto et al. (2013) from their meta-analysis of X-factor values derived from a variety of observational and theoretical studies. The mass is calculated from the column density by applying a Galactic rotation curve to convert velocity to distance. This included making assumptions regarding whether gas velocities relate to near- or far-side distances. Comparison with the spiral arm positions suggest that the bulk of the gas observed does arise at near distances, similar to the assumption in Braiding et al. (2015). However, we now present mass estimates based on the two extremes, of all the gas being at the near-distance and all at the far-distance. We have not included, however, molecular gas at positive velocities, which lie beyond the Solar Circle in this calculation. While such gas is clearly present at some PV-plot positions, the low fluxes when averaged over an entire degree, combined with their large distances, result in large absolute errors in the mass determination. Hence, we have not included them in Figure 8 (but see also the note at the end of the next paragraph). We find that typically there are a few $\times 10^6 M_\odot$ of molecular gas per square degree from $l = 300^\circ$ to $l = 330^\circ$. The mass then rises to a peak of around $10^7 M_\odot$ per square degree between $l = 330^\circ$ and 340° , before falling by a factor of 2 at $l = 350^\circ$. The total molecular gas within $\pm 0.5^\circ$ of

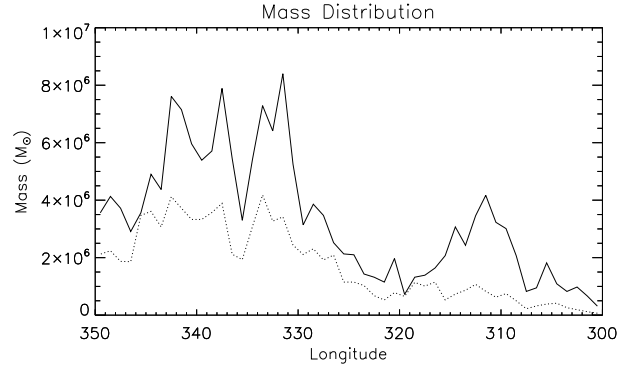


Figure 8. Molecular mass distribution for the inner degree of latitude across the Galaxy, extending from $l = 300\text{--}350^\circ$. Masses are calculated using a ^{12}CO X-factor of $2.7 \times 10^{20} \text{ cm}^{-2} (\text{K km s}^{-1})^{-1}$ to convert line fluxes to column densities for all gas detected within the solar circle (i.e. that with negative velocities). The solid line illustrates the mass calculated using the assumption of near-side distances; the dotted line assumes far-side distances (and is divided by a factor of 10 for presentation).

the Galactic Plane, in the 50 degrees from $l = 300\text{--}350^\circ$, is found to be $\sim 2 \times 10^8 M_\odot$ (if all were at the near distance) and $\sim 9 \times 10^8 M_\odot$ (all at the far distance). While not included in the plot, the total amount of gas lying beyond the solar circle is estimated to be around $4 \times 10^7 M_\odot$. This would contribute an additional 5 to 20% to the total molecular gas content calculated here. From the moment maps in Appendix A.4, it is clear that we have observed not only ^{12}CO , but also ^{13}CO at far distances with velocities $> +30 \text{ km s}^{-1}$.

4.3 C¹⁸O clump catalogue

When the faint C¹⁸O line is detected it is almost certainly optically thin due to the low abundance of the molecule with respect to ^{12}CO , and so provides a sightline that penetrates entirely through clouds. Thus the highest column density molecular clumps are detected in C¹⁸O. In order to investigate the distribution of C¹⁸O clumps across the Milky Way, we isolate individual clumps by applying the Clumpfind⁶ algorithm (Williams et al., 1994) to the region between $330 < l < 340^\circ$ where $-0.5 < b < +0.5$, and $-140 < V_{\text{LSR}} < +50 \text{ km s}^{-1}$. In order to efficiently run this calculation on the Mopra CO data cubes, a number of simplifications needed to be performed: firstly the data was binned by 10 spectral channels (reducing the velocity resolution to $\sim 0.92 \text{ km s}^{-1}$) and secondly it was box smoothed using the IDL routine `smooth`⁷. The relative 1σ emission level of the C¹⁸O data cube is then $\sim 0.10 \text{ K}$ (derived by computing the standard deviation of the spectra in an emission-free

⁶<http://www.ifa.hawaii.edu/users/jpw/clumpfind.shtml>

⁷We employed a box smoothing kernel of dimensions [2,2,1]; utilising 2 voxels in the angular directions and 1 along the velocity axis.

region).

`Clumpfind` operates by finding local peaks of emission and then contouring around them to decompose the data cube into a set of clumps of C¹⁸O emission. It requires two input parameters to work: the increment between contour levels, `inc`, and the desired lower limit of clump emission, `low`; after a series of tests both of these were assigned the value of 0.45 K, equivalent to the 4.5 σ emission level.

The resulting bright C¹⁸O clumps are presented in Table 3 of Appendix A.5; for each of these we report the coordinates of the clump centroid, the average and peak main beam brightness temperature, the relative FWHM extensions in arcsec and km s⁻¹, and its radius in arcseconds. Prior to computing the physical properties of each clump, we compare the C¹⁸O and ¹³CO spectral profiles for each line of sight, rejecting those false detections that are noisy spikes in the C¹⁸O band without a clear peak in both CO isotopologues. We also check the `clumpfind` ID assignation to ensure each clump is physically distinct (as it lists nearby local maxima within the same physical structure as independent clumps); within the catalogue the minimum separation between two centroids is 9 voxels.

Using the model described above in §4.2 we calculate near and far distances to each clump, which are also listed in Table 3. Following Wilson et al. (2009) we derive the C¹⁸O column density for each clump, assuming that the gas is in local thermodynamic equilibrium (LTE) at a fixed T_{ex} = 10 K, to be:

$$N(\text{C}^{18}\text{O}) = 3.0 \times 10^{14} \frac{T_{\text{ex}}}{1 - e^{-(T_0^{18}/T_{\text{ex}})}} \int \tau_{18} dv, \quad (1)$$

where T₀¹⁸ = 5.27 K is the energy level of the J = 1–0 C¹⁸O transition, and dv is the velocity interval in km s⁻¹. The optical depth, τ_{18} , is:

$$\tau_{18} = -\ln \left(1 - \frac{T_{\text{MB}}^{18}}{5.27} \left[[e^{5.27/T_{\text{ex}}} - 1]^{-1} - 0.16 \right]^{-1} \right). \quad (2)$$

The column density of H₂, N(H₂) is then calculated for each clump using the abundance ratio of [H₂/C¹⁸O] = 5.88 × 10⁶ from Frerking et al. (1982). Finally, we are able to derive near and far masses for each clump. Assuming that the clumps are all located at the near distance, the total mass traced by C¹⁸O in this region is ∼2.5 × 10⁶ M_⊙, equivalent to 10% of the total molecular gas mass traced by ¹²CO in the same portion of Galactic Plane, as only the highest density regions are traced by C¹⁸O. Nevertheless, the C¹⁸O molecule provides an important optically thin tracer of the molecular gas.

5 ISM SURVEY SYNERGIES

The Mopra CO survey is a timely addition to several Galactic Plane surveys currently under way. In particular, we have observed to a Galactic longitude of $l = 11^\circ$,

giving 2 square degrees of overlap with the Northern Hemisphere FOREST Unbiased Galactic plane Imaging survey with the Nobeyama 45-m telescope (FUGIN; Minamidani et al., 2015; Umemoto et al., 2017), a similarly high resolution ¹²CO(1–0) survey covering from $l = 10^\circ$ – 50° and $l = 198^\circ$ – 236° where $|b| < 1^\circ$. Preliminary work comparing these surveys is now underway, but as mentioned in §4, similar comparisons with the Nanten2 CO survey suggest that the observed fluxes and structures in the overlapping region will be equivalent (H. Sano, March 2017, pers.comm.).

Combining Mopra CO with data from other surveys presents the opportunity to fully characterise regions of interest in order to probe the origins and history of molecular clouds (Burton et al., 2013). Recently, Sano et al. (2017a) presented work using data from this survey, ASTE and Nanten2 to investigate high-mass star cluster formation triggered by cloud-cloud collisions, in particular focusing on the H II region RCW 36, located in the Vela Molecular Ridge. They suggested that a cloud-cloud collision formed RCW 36 and its stellar cluster, with a relative velocity separation of ∼5 km s⁻¹. The estimated cloud separation of ∼0.85 pc was estimated to occur over a time-scale of ∼0.2 Myr, assuming a distance of 1.9 kpc, consistent with the age of the cluster. The resulting O-type star formation lead to a high measured CO rotational temperature.

CO isotopologue data from DR1 of the Mopra Galactic Plane Survey was exploited in an investigation of the so-called ‘dark’ component of molecular gas towards a cold, filamentary molecular cloud in the G328 sight-line (Burton et al., 2014, 2015). The authors compared the distribution of atomic H I-traced gas to atomic C emission (which traces some CO-dark molecular gas) and the CO-traced molecules observed in DR1. They found that ¹³CO and [C i] show similar distributions and velocity profiles, the abundance of atomic C increases towards the molecular cloud edges, consistent with CO photodissociation by an average interstellar radiation field and cosmic-ray ionisation at low optical depths. Further comparison to dust images from Herschel showed that the cloud was IR-dark and that no star formation is yet occurring within the young filament. Extended studies using C⁺ observations from the Stratospheric Observatory for Infrared Astronomy (SOFIA) will target gas that may be in the transition phase between atomic and molecular forms of Carbon (Risacher et al., 2016), allowing a better tracing of the dark molecular gas that has been inferred from gamma-ray observations (see §6) and to study molecular cloud formation in detail.

The APEX Telescope Large Area Survey of the Galaxy (ATLASGAL) has been used to perform an unbiased census of massive dense clumps in the Galactic Plane at 870 μm , using Mopra CO data to provide radial velocities to ∼500 of the clumps (Urquhart et al., 2018). The properties of these clumps were exploited to develop

an evolutionary classification scheme showing trends for increasing dust temperatures and luminosities as a function of evolution, showing that most of the clumps are already associated with star formation. We expect to determine a similar evolutionary scheme for molecular cloud cores (including the C¹⁸O cores presented in §4.3), using the Mopra CO and other survey data in future.

The OH $\lambda = 18$ cm lines are complementary to CO and H I when estimating the mass of H₂ in molecular clouds, as at densities well below 10³ cm⁻³ CO is affected by ultraviolet shielding, interstellar chemistry, and sub-thermal processes (Dickey et al., 2013). The GASKAP (The Galactic Australian Square Kilometre Array Pathfinder) Survey will trace atomic hydrogen directly through the H I transition and OH (Dickey et al., 2013). The GASKAP survey will achieve spatial resolutions of 20–60 arcsec for H I and 90–180 arcsec for OH, the former comparable with the Mopra CO survey, allowing astronomers to carry out pixel to pixel comparisons between the different tracers. Also using ASKAP, the EMU (Evolutionary Map of the Universe) Survey will provide a similar-resolution high sensitivity map of radio continuum emission in the Galactic Plane, allowing the detection of H II regions, supernova remnants and planetary nebulae at similar resolutions to Mopra CO and GASKAP (Norris et al., 2011). Future improvements to the velocity resolution of ASKAP may bring it closer to that of Mopra.

Towards a better understanding of the motions of the Galactic Centre, Yan et al. (2017) employed Mopra ¹²CO and ¹³CO data in conjunction with OH absorption data from the Southern Parkes Large-Area Survey in Hydroxyl (SPLASH; Dawson et al., 2014) to create a 3-dimensional image of the Galactic Centre region at a spatial resolution of 38 pc. The Galactic Centre was well-described with a bar-like structure at an angle of $67 \pm 2^\circ$ to the line-of-sight. More generally the Mopra CO data from the Central Molecular Zone (Blackwell et al., 2018) will be key to studies of star formation and its effect on the evolution of the CMZ (e.g. Kruijssen et al., 2015).

Interstellar medium surveys are critical to X-ray and other high-energy studies, where they are used to determine distances to supernova remnants, particularly using morphology anti-correlations and photoelectric absorption studies (e.g. Maxted et al., 2018). Heinz et al. (2015) observed X-ray light echoes from the X-ray binary Circinus X-1, which demonstrated four well-defined rings with radii from 5 to 13 arcmin. By modelling the dust distribution towards Circinus X-1 and comparing that to ¹²CO emission from Data Release 3 they were able to identify the source clouds for the innermost rings and determine the distance to Circinus X-1 to be ~ 9.4 kpc for the binary system, ruling out previous near distance estimates of ~ 4 kpc.

The Mopra CO survey will also be well-complemented

by ¹³CO(2-1) data from SEDIGISM (Structure, Excitation, and Dynamics of the Inner Galactic Interstellar Medium; Schuller et al., 2017), allowing the calculation of rotational temperature estimates for regions that are optically-thick in ¹²CO and ¹³CO(1-0). Similarly, James Clerk Maxwell Telescope (JCMT) ¹²CO(3-2) observations (Dempsey et al., 2013) will be used to refine temperature and column density estimations for molecular clouds of interest.

Perhaps most importantly the Mopra CO survey data will be used as a finder chart for objects of interest to be observed with ALMA, which offers arcsecond-level spatial resolution in the CO(1-0) transition (Mathews et al., 2013). We note that Mopra CO data has guided successful ALMA and SOFIA applications for observations towards molecular cores interacting with the young supernova remnant, RX J1713.7–3946 (Rowell, 2017; Sano, 2017). The resultant data will reveal the extremely fine details of these structures and provide an important step towards understanding cosmic ray origins.

Future ISM catalogues of sources of interest traced by the Mopra CO survey will be essential for determining the best objects to follow-up with ALMA. A sample catalogue of bright C¹⁸O clumps is in Appendix A.5, along with characterisations of the location, size, temperature and mass. The complete catalogue will provide supplementary information useful for targeting dense clumps in star formation research.

6 GAMMA-RAY OBSERVATIONS

Gamma-ray maps provide an important window into the gas distribution of the Galaxy that rely on studies of CO, [C I], [C II] and H I. A large component of gamma-ray emission from the Milky Way comes from three distinct so-called ‘diffuse’ source types (see e.g. Acero et al., 2013, 2017; Dubus et al., 2013):

1. Truly diffuse gamma-rays from Cosmic Rays (CRs) circulating in the Galactic Plane for $\gtrsim 10^6$ years, i.e. the diffuse CR ‘sea’;
2. Local gamma-ray enhancements from CRs escaping local accelerators on time-frames $\lesssim 10^5$ years; and
3. Unresolved sources of gamma-ray emission across the Galaxy.

Diffuse sources of type (1) and (2) involve cosmic-ray protons interacting with gas in the Galactic Plane via proton-proton collisions that produce charged and neutral pions. The neutral pions quickly decay into gamma-ray photons. Diffuse sources of type (3) may also have a component of gamma-ray emission produced via this mechanism, depending on the source.

Unlike spectral line emission, gamma-rays from pion-decay can be considered a general tracer of gas density

independent of temperature or chemistry. As the gamma-ray flux generated by proton-proton interactions is a product of cosmic ray density and gas density, gamma-ray maps can be used to highlight excesses of both gas and CRs. It follows that gas studies and gamma-ray astronomy are intimately tied together.

In order to identify gamma-ray sources in the Galactic Plane maps from Fermi-LAT, which operates in the 0.02–300 GeV gamma-ray regime (Atwood et al., 2009), a model of the gamma-ray emission from diffuse source (1) was required. This model was constructed from H I and CO gas maps of similar resolution (e.g. McClure-Griffiths et al., 2005; Dame et al., 2001) and revealed that previous work underestimated the gamma-ray Galactic contribution at high latitudes and hence overestimated the background CR ‘sea’ (e.g. Strong et al., 2004).

Galactic molecular cores resolved at sub-arcminute scales in both gamma-rays and CO(1–0) emission will enable the identification of pion-decay signatures near cosmic-ray sources (Cameron, 2012; Acharya et al., 2013), and may deliver kinematic distance solutions for cosmic-ray sources (Cherenkov Telescope Array Consortium et al., 2017). The signature of this decay will be particularly strong if the gamma-ray spectral index is altered by CR diffusion into molecular cores due to energy-dependent propagation (e.g. Gabici et al., 2007; Maxted et al., 2012). Indeed, a common theme developing for young gamma-ray shell-type supernova remnants (which are regarded as key PeV CR acceleration candidates) is the existence of sub-arcminute-scale molecular cores embedded in the perimeter of regions blown out by the progenitor star (Fukui, 2008; Moriguchi et al., 2005; Sano et al., 2013; Maxted et al., 2013; Fukuda et al., 2014; Kavanagh et al., 2015; Fukui et al., 2017; Sano et al., 2017b). The next-generation Cherenkov Telescope Array (CTA Cherenkov Telescope Array Consortium et al., 2017) is expected to provide gamma-ray maps at a resolution sufficient to identify local peaks due to cloud clumps and filaments. Furthermore, the Mopra CO survey will probe interstellar medium dynamics by revealing broad-line or asymmetric emission indicative of the shock-gas interactions, as is expected of some gamma-ray sources like older supernova shocks and pulsar wind nebulae (e.g. Arikawa et al., 1999).

Data from the Mopra Galactic Plane CO Survey have already been used to examine the nature of gamma-ray sources observed with the highest resolution gamma-ray telescope, H.E.S.S. (High Energy Stereoscopic System, Aharonian et al., 2006). Understanding the links between TeV gamma-ray emission and the parent high energy particle populations local to extreme Galactic objects is a step forward in the search for elusive CR hadron acceleration sites; pulsar wind nebulae and SNRs with associated gamma-ray detections are the primary candidates in the pursuit for Galactic CR sources.

Lau et al. (2017b) exploited Mopra CO and CS iso-

topologue data to investigate the gamma-ray sources HESS J1640–465 and HESS J1641–463, which are positionally coincident with the SNRs G338.3–0.0 and G338.5+0.1. The authors found coincident diffuse molecular gas, with a bright complex of dense gas and H II regions connecting the SNRs. CO-derived masses were then utilised to estimate the density of >1 TeV CRs assuming that the gamma-ray emission was caused by pion-decay following proton-proton interactions. The values inferred were in the range of 100–1000 times the Solar value (Lau et al., 2017b). Similarly, CO and CS observations that identify filamentary molecular features towards the unidentified objects HESS J1614–518 and HESS J1616–508 (Lau et al., 2017a) represent the first steps in forming an understanding of the nature gamma-ray emitters.

Maxted et al. (2018) compared line-of-sight column densities from Mopra CO and the SGPS H I emission to X-ray absorption column densities for the bright shell-type gamma-ray SNR, HESS J1731–347. This enabled the calculation of a kinematic distance to the source, and revealed a large associated molecular gas cloud that bridged the region between HESS J1731–347 and a nearby unidentified gamma-ray source, HESS J1729–345. Such a discovery adds weight to the suggestion that some unidentified gamma-ray sources are the product of so-called ‘runaway cosmic rays’ that escape a CR acceleration site and diffuse into nearby molecular gas clouds (i.e. diffuse sources of type 2). Similar CR scenarios have also been investigated for pulsar wind nebulae and their progenitor supernova remnants (e.g. HESS J1826–130, Voisin et al., 2016).

With the CTA now under construction (Cherenkov Telescope Array Consortium et al., 2017), subarcminute resolution gamma-ray maps will soon become available. As with Fermi-LAT, CTA will require similar-resolution gas maps to characterise the diffuse gamma-ray emission components (1 and 2) and enable studies of gamma-ray sources and dark gas. Furthermore, CTA’s improved sensitivity will enable it to detect sources across the Galactic disk, expanding on the rather limited (few kpc for sources of <10% Crab flux) horizon achieved by current telescopes like H.E.S.S. Towards this future, we are preparing molecular gas maps that will fully parametrise Mopra CO, FUGIN and GASKAP data for use in gamma-ray modelling of the Galactic Plane (e.g. using GALPROP, PICARD and DRAGON; Strong & Moskalenko, 1998; Kissmann, 2014; Evoli et al., 2017, respectively).

7 SUMMARY

We present the third data release of the Mopra Southern Galactic Plane CO Survey, covering 50 square degrees between Galactic longitude $l = 300\text{--}350^\circ$ and latitude $b = \pm 0.5^\circ$. These data are part of a larger campaign to

map the molecular gas of the inner Galactic Plane in ^{12}CO , ^{13}CO , C^{18}O and C^{17}O (1–0) emission.

We find general agreement between the CO spectral line profiles of the Mopra survey and those of the Columbia survey for each square degree of coverage. Furthermore, we find a modest agreement between the Mopra survey position-velocity structure and a recent Galactic Plane model (Vallée, 2016). A preliminary catalogue of C^{18}O clumps presented traces $\sim 10\%$ of the observed ^{12}CO molecular gas, illustrating the importance of this optically thin tracer of molecular gas.

The Mopra CO survey, which is estimated to trace a $\sim\text{few}\times 10^6 \text{ M}_\odot$ of molecular gas per square degree, is already making an impact on the search for Galactic cosmic-ray sources and star formation research. We discuss past and future multi-wavelength investigations towards a number of Galactic Plane sources and synergies with other surveys.

The Mopra CO survey is still ongoing, with the intention of covering the entire fourth quadrant and expanding to Galactic latitudes beyond $b = \pm 1.0^\circ$ by the end of 2018. As the data are published, they are being made available at the survey website, and the PASA data archive.

8 ACKNOWLEDGEMENTS

The Mopra radio telescope is part of the Australia Telescope National Facility. Operations support was provided by the University of New South Wales, the University of Adelaide and Western Sydney University. Many staff of the ATNF have contributed to the success of the remote operations at Mopra. We particularly wish to acknowledge the contributions of David Brodrick, Philip Edwards, Brett Hiscock, and Peter Mirtschin.

This research made use of Astropy, a community-developed core Python package for Astronomy (Astropy Collaboration et al., 2013) and the IDL Astronomy Library (Landsman, 1993).

We are indebted also to the financial support of the #TeamMopra kickstarter contributors, listed at www.mopra.org. The University of New South Wales Digital Filter Bank used for the observations with the Mopra Telescope (the UNSW-MOPS) was provided with support from the Australian Research Council (ARC). We also acknowledge ARC support through Discovery Project DP120101585 and Linkage, Infrastructure, Equipment and Facilities project LE160100094.

REFERENCES

- Acero F., et al., 2013, *Astroparticle Physics*, 43, 276
 Acero F., et al., 2017, *ApJ*, 840, 74
 Acharya B. S., et al., 2013, *Astroparticle Physics*, 43, 3
 Aharonian F., et al., 2006, *A&A*, 457, 899
 Ao Y., et al., 2013, *A&A*, 550, A135
 Arikawa Y., Tatematsu K., Sekimoto Y., Takahashi T., 1999, *PASJ*, 51, L7
 Astropy Collaboration et al., 2013, *A&A*, 558, A33
 Atwood W. B., et al., 2009, *ApJ*, 697, 1071
 Benjamin R. A., et al., 2003, *PASP*, 115, 953
 Blackwell R., et al., 2018, in prep
 Bolatto A. D., Wolfire M., Leroy A. K., 2013, *ARA&A*, 51, 207
 Braiding C., et al., 2015, *PASA*, 32, e020
 Burton M. G., et al., 2013, *PASA*, 30, e044
 Burton M. G., et al., 2014, *ApJ*, 782, 72
 Burton M. G., et al., 2015, *ApJ*, 811, 13
 Cameron R. A., 2012, in Ground-based and Airborne Telescopes IV. p. 844418, doi:10.1117/12.926614
 Carey S. J., et al., 2009, *PASP*, 121, 76
 Cherenkov Telescope Array Consortium T., et al., 2017, preprint, (arXiv:1709.07997)
 Churchwell E., et al., 2009, *PASP*, 121, 213
 Dame T. M., Thaddeus P., 2011, *ApJ*, 734, L24
 Dame T. M., Hartmann D., Thaddeus P., 2001, *ApJ*, 547, 792
 Dawson J. R., et al., 2014, *MNRAS*, 439, 1596
 Dempsey J. T., Thomas H. S., Currie M. J., 2013, *ApJS*, 209, 8
 Dickey J. M., et al., 2013, *PASA*, 30, e003
 Drlica-Wagner A., Gómez-Vargas G. A., Hewitt J. W., Linden T., Tibaldo L., 2014, *ApJ*, 790, 24
 Dubus G., et al., 2013, *Astroparticle Physics*, 43, 317
 Evoli C., Gaggero D., Vittino A., Di Bernardo G., Di Mauro M., Ligorini A., Ullio P., Grasso D., 2017, *JCAP*, 2, 015
 Frerking M. A., Langer W. D., Wilson R. W., 1982, *ApJ*, 262, 590
 Fukuda T., Yoshiike S., Sano H., Torii K., Yamamoto H., Acero F., Fukui Y., 2014, *ApJ*, 788, 94
 Fukui Y., 2008, in Aharonian F. A., Hofmann W., Rieger F., eds, American Institute of Physics Conference Series Vol. 1085, American Institute of Physics Conference Series. pp 104–111 (arXiv:0810.5416), doi:10.1063/1.3076625
 Fukui Y., et al., 2017, preprint, (arXiv:1708.07911)
 Gabici S., Aharonian F. A., Blasi P., 2007, *Ap&SS*, 309, 365
 Gooch R., 1996, in Jacoby G. H., Barnes J., eds, Astronomical Society of the Pacific Conference Series Vol. 101, Astronomical Data Analysis Software and Systems V. p. 80
 Heinz S., et al., 2015, *ApJ*, 806, 265
 Jones P. A., et al., 2012, *MNRAS*, 419, 2961
 Jones P. A., Burton M. G., Cunningham M. R., Tothill N. F. H., Walsh A. J., 2013, *MNRAS*, 433, 221
 Kavanagh P. J., Sasaki M., Bozzetto L. M., Filipović M. D., Points S. D., Maggi P., Haberl F., 2015, *A&A*,

- 573, A73
- Kissmann R., 2014, *Astroparticle Physics*, 55, 37
- Kruijssen J. M. D., Dale J. E., Longmore S. N., 2015, *MNRAS*, 447, 1059
- Ladd N., Purcell C., Wong T., Robertson S., 2005, *PASA*, 22, 62
- Landsman W. B., 1993, in Hanisch R. J., Brissenden R. J. V., Barnes J., eds, Astronomical Society of the Pacific Conference Series Vol. 52, Astronomical Data Analysis Software and Systems II. p. 246
- Lau J. C., et al., 2017a, *PASA*, 34, e064
- Lau J. C., et al., 2017b, *MNRAS*, 464, 3757
- Mathews G. S., et al., 2013, *A&A*, 557, A132
- Maxted N., et al., 2012, *MNRAS*, 422, 2230
- Maxted N., et al., 2013, *PASA*, 30, e055
- Maxted N., et al., 2018, *MNRAS*, 474, 662
- McClure-Griffiths N. M., Dickey J. M., Gaensler B. M., Green A. J., Havercorn M., Strasser S., 2005, *ApJS*, 158, 178
- Minamidani T., et al., 2015, in EAS Publications Series. pp 193–194, doi:10.1051/eas/1575036
- Molinari S., et al., 2010, *PASP*, 122, 314
- Moriguchi Y., Tamura K., Tawara Y., Sasago H., Yamada K., Onishi T., Fukui Y., 2005, *ApJ*, 631, 947
- Norris R. P., et al., 2011, *PASA*, 28, 215
- Pierce-Price D., et al., 2000, *ApJ*, 545, L121
- Pineda J. L., Goldsmith P. F., Chapman N., Snell R. L., Li D., Cambréy L., Brunt C., 2010, *ApJ*, 721, 686
- Planck Collaboration et al., 2015, *A&A*, 582, A31
- Rebolledo D., et al., 2016, *MNRAS*, 456, 2406
- Risacher C., et al., 2016, *A&A*, 595, A34
- Rowell G. e. a., 2017, SOFIA Proposal P06-0122
- Sano H. e. a., 2017, ALMA Proposal XXXXXX
- Sano H., et al., 2013, *ApJ*, 778, 59
- Sano H., et al., 2017a, preprint, (arXiv:1706.05763)
- Sano H., et al., 2017b, *ApJ*, 843, 61
- Schuller F., et al., 2017, *A&A*, 601, A124
- Strong A. W., Moskalenko I. V., 1998, *ApJ*, 509, 212
- Strong A. W., Moskalenko I. V., Reimer O., 2004, *ApJ*, 613, 962
- Umemoto T., et al., 2017, *PASJ*, 69, 78
- Urquhart J. S., et al., 2018, *MNRAS*, 473, 1059
- Vallée J. P., 2014, *AJ*, 148, 5
- Vallée J. P., 2016, *AJ*, 151, 55
- Voisin F., Rowell G., Burton M. G., Walsh A., Fukui Y., Aharonian F., 2016, *MNRAS*, 458, 2813
- Walker C. K., et al., 2004, in Oschmann Jr. J. M., ed., Proc. SPIE Vol. 5489, Ground-based Telescopes. pp 470–480, doi:10.1117/12.551424
- Williams J. P., de Geus E. J., Blitz L., 1994, *ApJ*, 428, 693
- Wilson R. W., Jefferts K. B., Penzias A. A., 1970, *ApJ*, 161, L43

- Wilson T. L., Rohlfs K., Hüttemeister S., 2009, Tools of Radio Astronomy. Springer-Verlag, doi:10.1007/978-3-540-85122-6
- Yan Q.-Z., et al., 2017, *MNRAS*, 471, 2523

A SUPPLEMENTARY MATERIALS

A.1 The Mopra Beam

To characterise the Mopra beam resolution, observations of the red supergiant variable star AH Scorpii were performed on the 14th of November, 2017. SiO(2–1, $v=1$) masers from AH Scorpii are point-like, allowing the Mopra beam size and shape to be characterised. The integrated data, described more fully in §3.2, are illustrated in Figure 9.

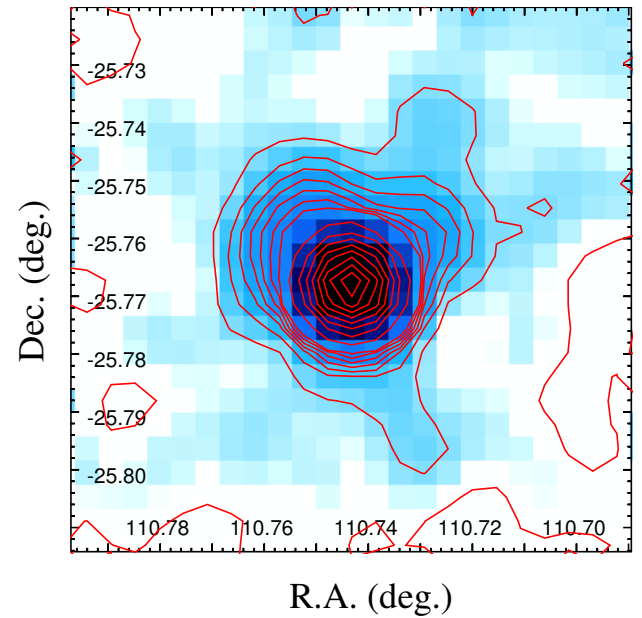


Figure 9. A Mopra SiO(2–1, $v=1$) image of the red supergiant variable star, AH Scorpii, integrated between 2 and 48 km s⁻¹. Red contours indicate 1% steps between 0 to 10% total intensity, and 10% steps between 10 and 100% the total intensity. Observations were carried out on the 14th of November, 2017.

A.2 System Temperature

Maps of the system temperature for the ¹²CO isotologue are shown in Figure 10, with values approximately twice those of the ¹³CO and C¹⁸O isotopologues shown in Figure 11 (which occur in the same 2 GHz band of the spectrometer). Striping in these images occurs because the data is scanned in the l and b directions to minimize artefacts from poor sky conditions, while spots indicate points where high T_{sys} values have been removed (see §3 and Braiding et al., 2015, for additional details).

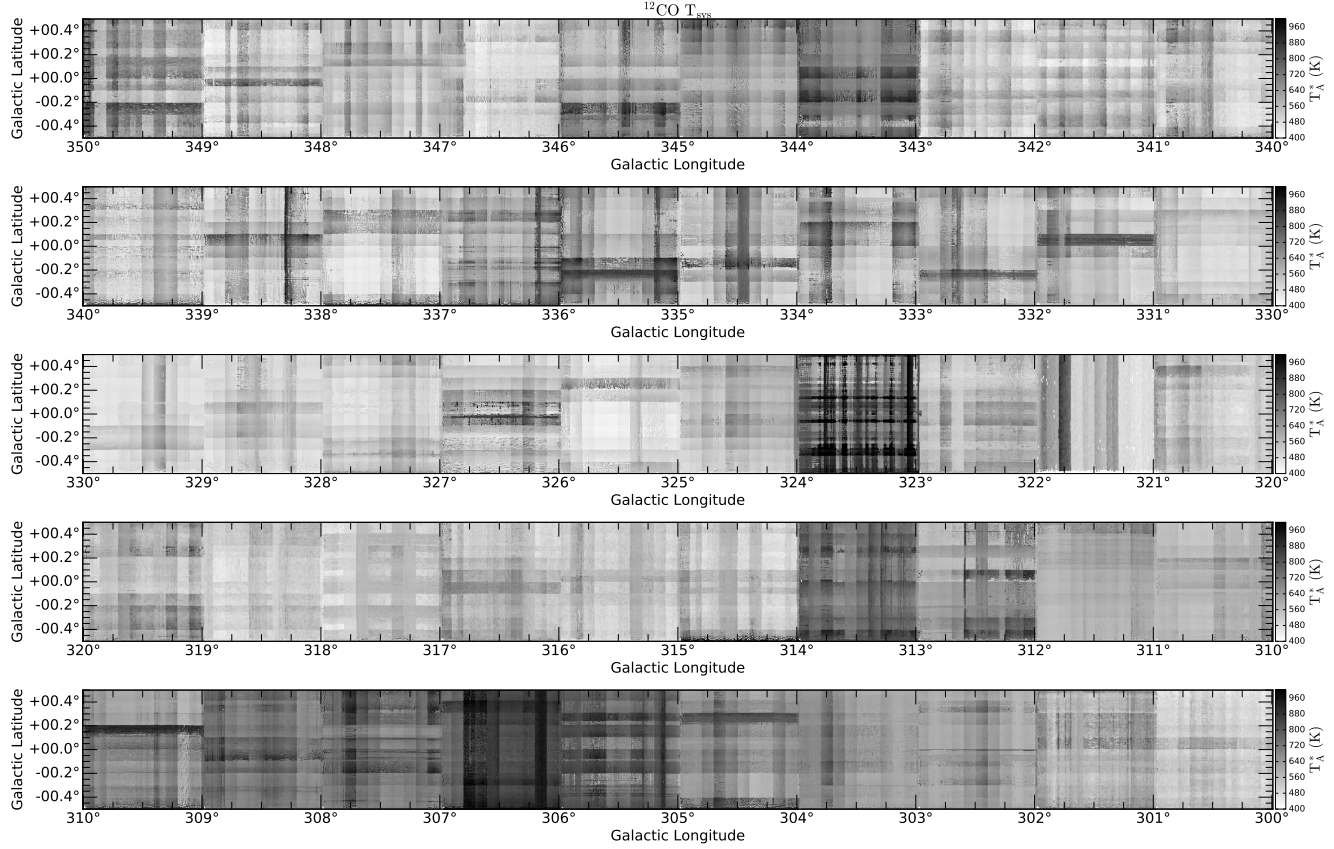


Figure 10. T_{sys} images for the ^{12}CO data covering the full 50 square degrees from $l = 300\text{--}350^\circ$ in units of T_A^* (K) (as indicated by the scale bars). The striping pattern is inherent to the data set, resulting from scanning in the l and b directions in variable observing conditions.

A.3 Averaged Spectra

The average line profiles for the ^{12}CO , ^{13}CO , and ^{12}CO from the Columbia survey (Dame et al., 2001), averaged over each square degree are displayed in Figures 12–21. A distinct progression towards increasingly negative velocities is seen from longitudes $l = 300\text{--}350^\circ$. At $l = 300^\circ$, the line of sight spectral line velocities are all higher than -50 km/s , consistent with the lower limit on velocity set by the Scutum-Crux arm tangent in the Galactic model adopted in this paper (see Figure 7). Positive-velocity spectral lines typically indicate emission seen from the far-side of the Galaxy (beyond the Solar Circle).

With increasing longitude, the range of spectral line velocities increases, and the negative extent of the range decreases beyond -100 km/s , consistent with expectations of the inner-Galaxy (see Figure 7). The mean intensity ratio between the average spectra illustrated in Figures 12–21 from the MopraCO and the Dame survey is 1.35 (with a median value of 1.36), with the individual values for each square degree listed in Table 2 below.

A.4 Integrated intensity maps

Figs. 22 to 41 are integrated intensity maps of $T_{MB}\Delta V$ from DR3. Grey scale images are taken from the ^{12}CO data and the contours are from the ^{13}CO data, between the velocity range of -150 and $+50 \text{ km s}^{-1}$ with an interval of 10 km s^{-1} . Note that some scanning artefacts are present in these images, evident as 1° -long line features in longitude or latitude, particularly near the edges of individual square degrees.

A.5 C¹⁸O clump catalogue

Table 3 presents a sample of C¹⁸O molecular clumps extracted from the Galactic longitude range $330 \leq l \leq 340^\circ$ data cubes as described in §4.3. These are the first items from a wider database that is in preparation and will describe all the C¹⁸O clumps comprised in the Mopra CO survey data ($300 \leq l \leq 350^\circ$ and beyond).

Two methods are used to compute the cloud areas: In the first (labelled A in Table 3), we define the clump area as the number of non-zero pixels in the integrated intensity map multiplied by the area of the single pixel in square arcseconds. The second (labelled A_{fwhm}) is the

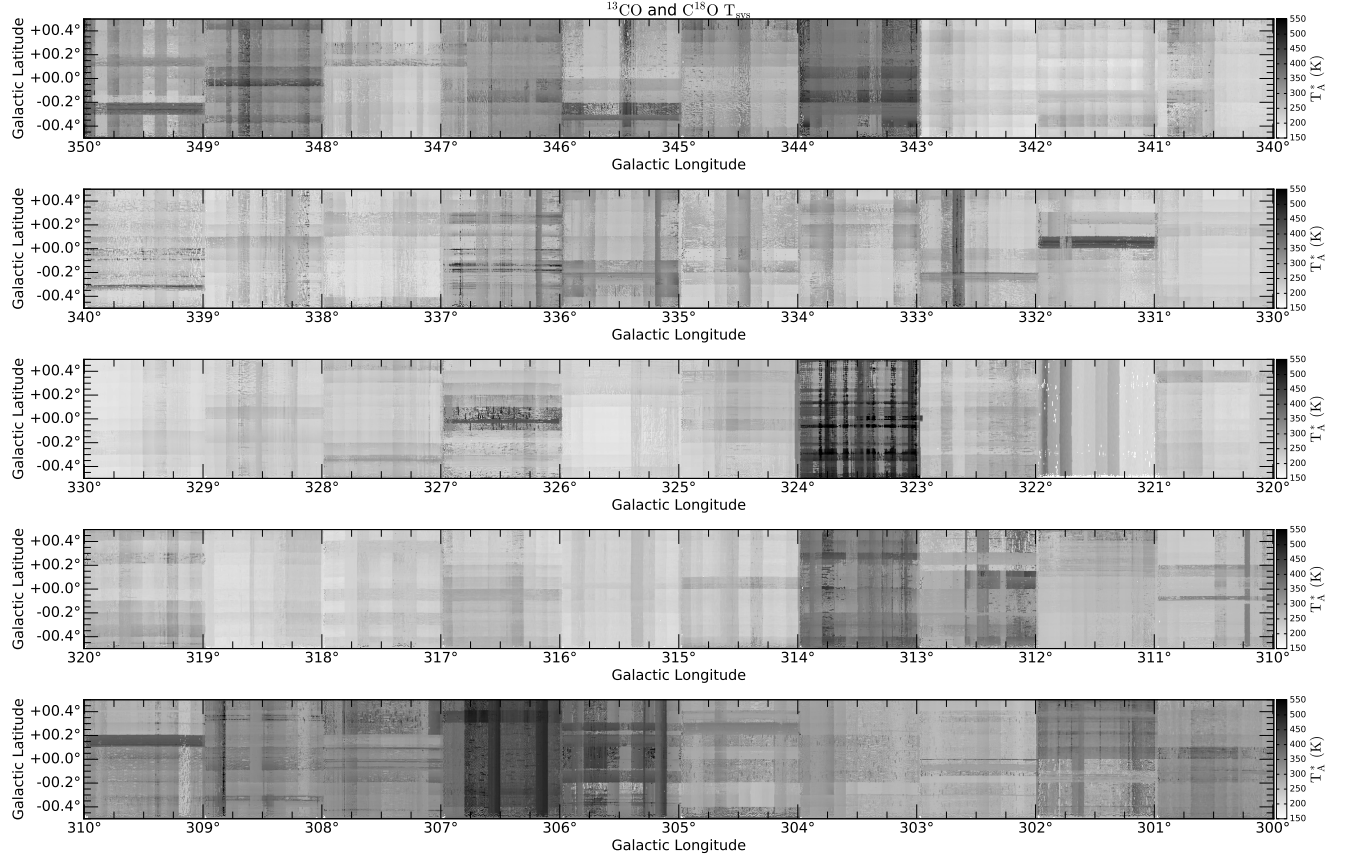


Figure 11. T_{sys} images for ^{13}CO and C^{18}O (which share the same 2 GHz band of the spectrometer) covering the full 50 square degrees from $l = 300\text{--}350^\circ$ in units of T_A^* (K) (as indicated by the scale bars). The striping pattern is inherent to the data set, resulting from scanning in the l and b directions in variable observing conditions.

area of an ellipse with semi-axes defined by the FWHM angular extensions Δl and Δb .

Note that for nine clumps we used the tangent point distance for both near and far distances, since their coordinates have no solution in the Galactic rotation curve; as a consequence their near and far masses are the same.

Table 2 Intensity ratios between the average spectra for each square degree of Mopra CO and the Columbia CO Survey (Dame et al., 2001), **calculated using the integrated intensities of each spectrum**. The mean over the 50 square degrees is 1.35, and the median 1.36.

Cube	Ratio								
G300	1.12	G310	1.44	G320	1.30	G330	1.39	G340	1.41
G301	1.25	G311	1.48	G321	1.20	G331	1.47	G341	1.38
G302	1.63	G312	1.45	G322	1.18	G332	1.43	G342	1.39
G303	1.42	G313	1.43	G323	1.23	G333	1.45	G343	1.13
G304	1.44	G314	1.35	G324	1.28	G334	1.45	G344	1.44
G305	1.59	G315	1.23	G325	1.28	G335	1.23	G345	1.49
G306	1.19	G316	1.27	G326	1.27	G336	1.32	G346	1.14
G307	1.67	G317	1.34	G327	1.27	G337	1.54	G347	1.40
G308	1.38	G318	1.26	G328	1.33	G338	1.47	G348	1.26
G309	1.40	G319	1.01	G329	1.33	G339	1.41	G349	1.30

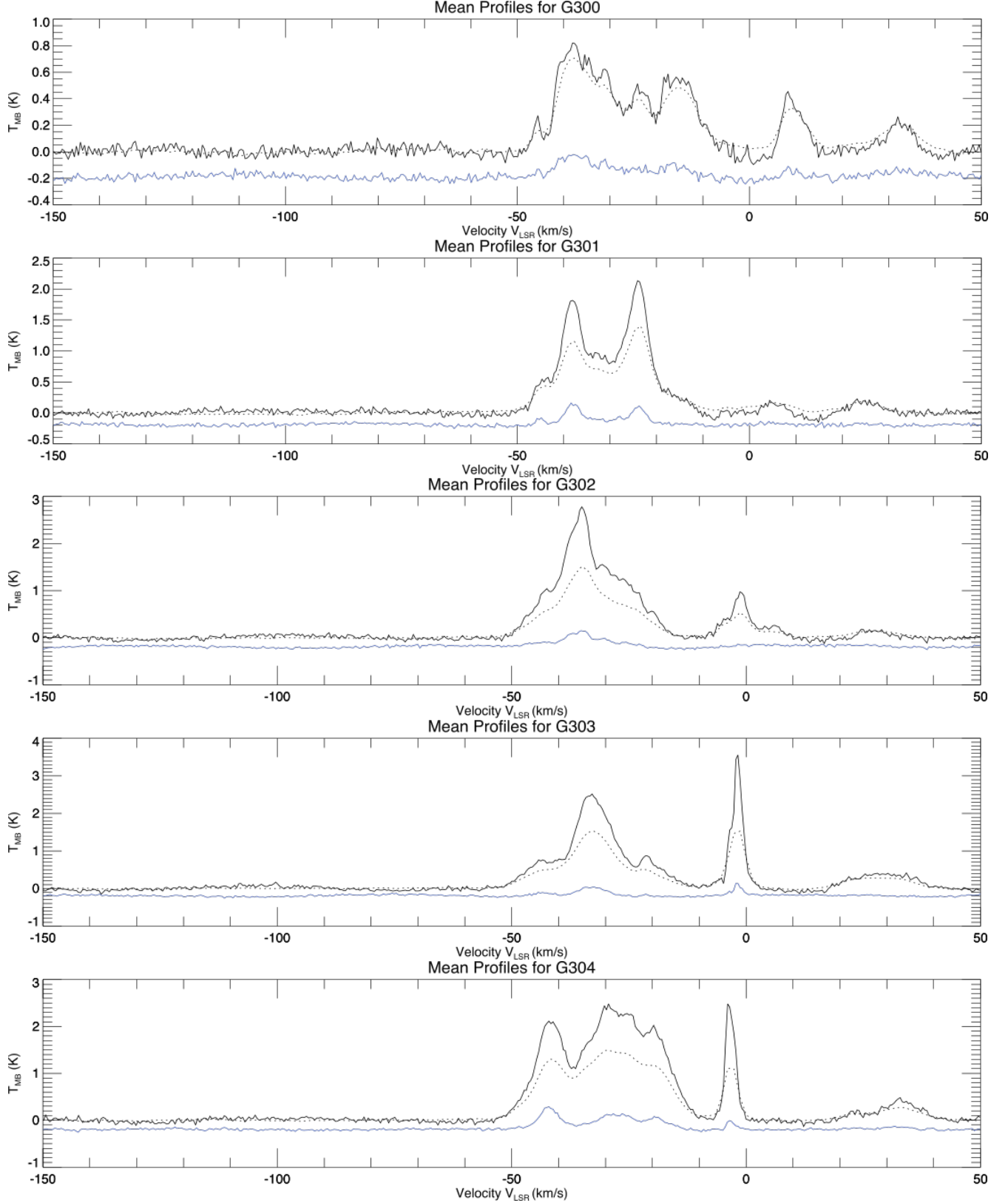


Figure 12. Average spectra for each square degree along the Galactic Plane between $l = 300\text{--}305^\circ$, labelled by their lower longitude limit, from $-150 < V_{\text{LSR}} < +50 \text{ km s}^{-1}$. The dark solid lines are the Mopra ^{12}CO data, while the blue is the ^{13}CO emission offset by -0.2 K . The dashed lines are the equivalent average ^{12}CO spectra from the Columbia CO Survey (Dame et al., 2001), which show systematic lower line intensities by a factor of ~ 1.35 (see Table 2 for degree-specific values).

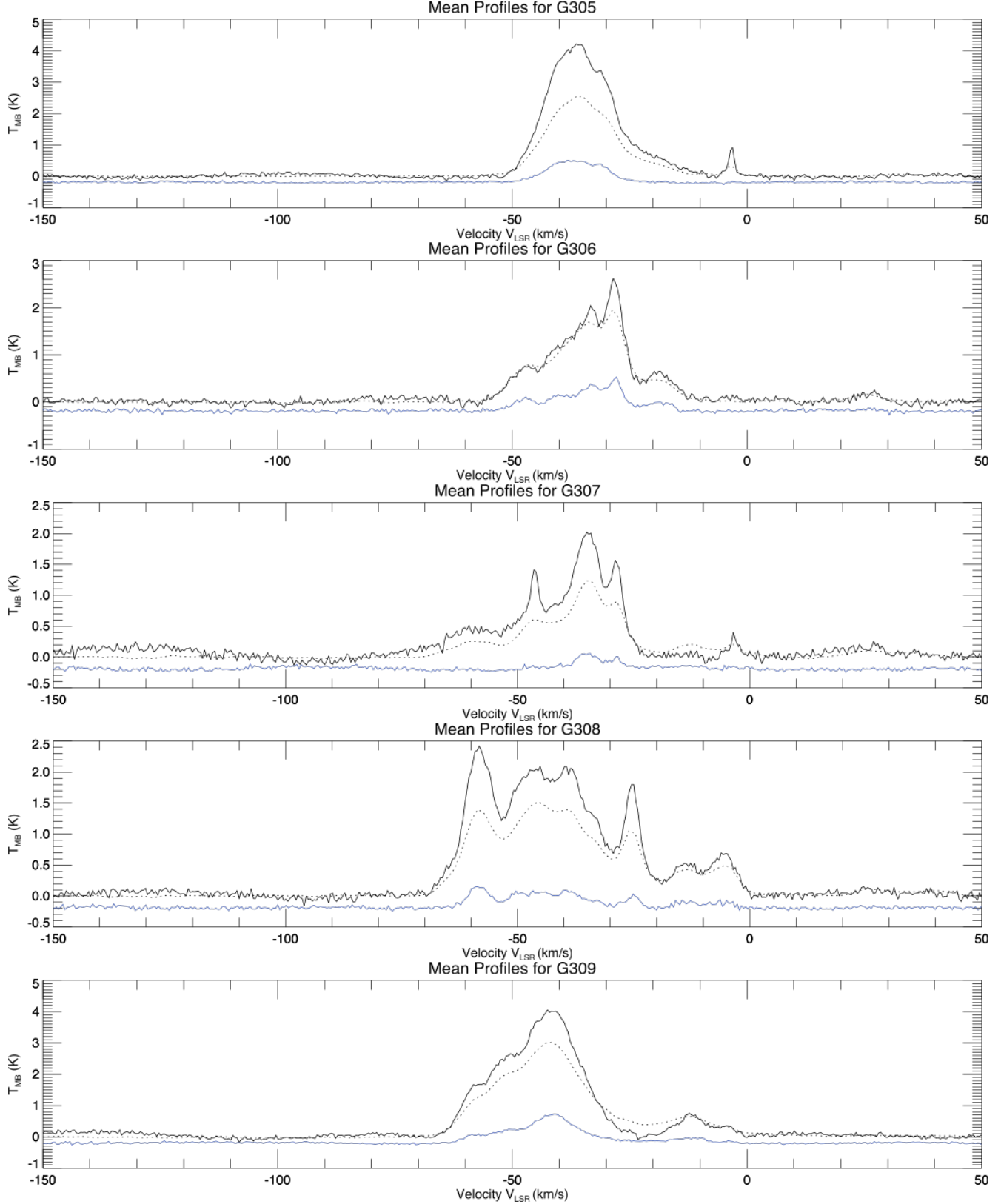


Figure 13. Average spectra for each square degree along the Galactic Plane between $l = 305\text{--}310^\circ$, labelled by their lower longitude limit, from $-150 < V_{\text{LSR}} < +50 \text{ km s}^{-1}$. The dark solid lines are the Mopra ^{12}CO data, while the blue is the ^{13}CO emission offset by -0.2 K . The dashed lines are the equivalent average ^{12}CO spectra from the Columbia CO Survey (Dame et al., 2001), which show systematic lower line intensities by a factor of ~ 1.35 (see Table 2 for degree-specific values).

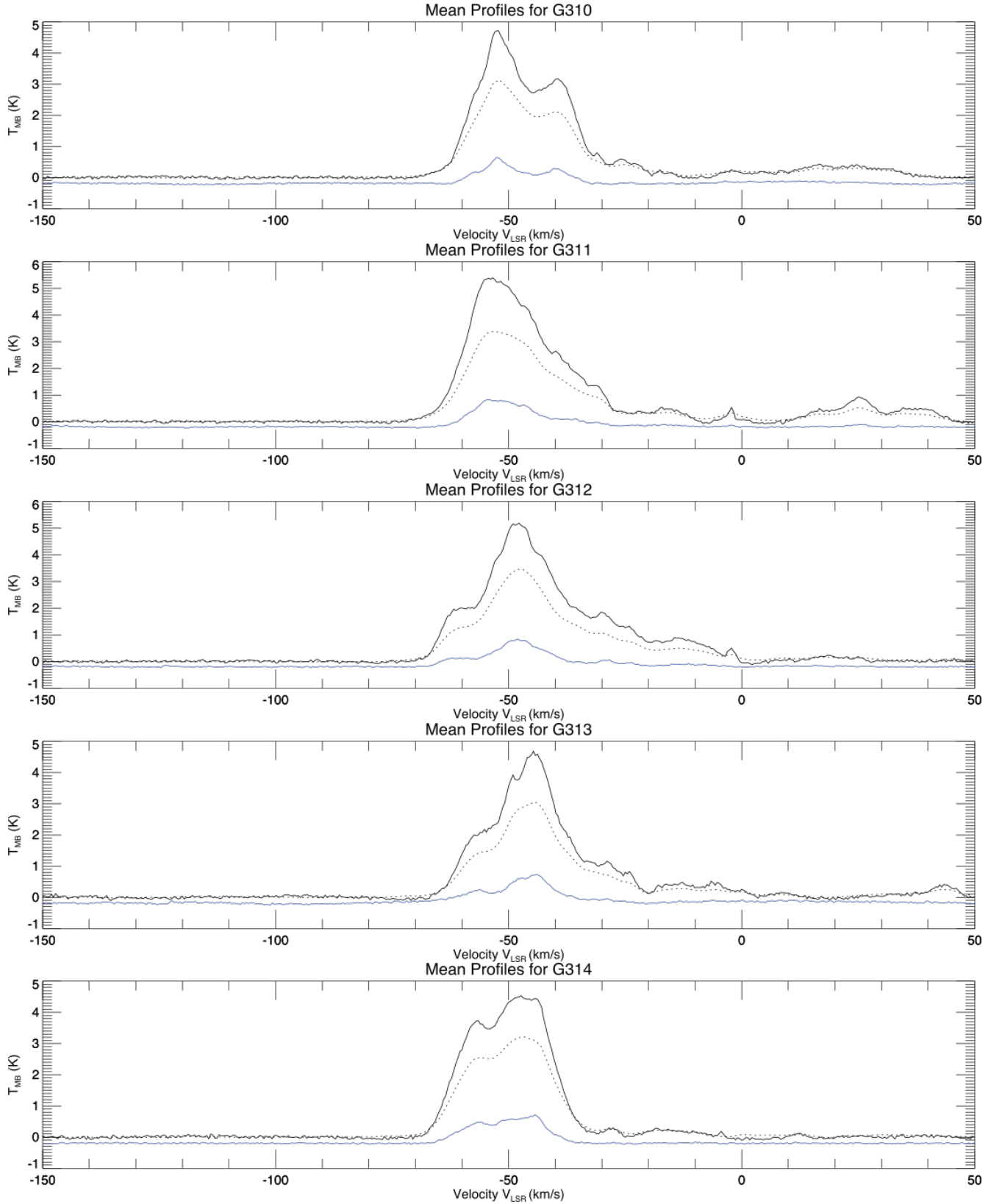


Figure 14. Average spectra for each square degree along the Galactic Plane between $l = 310\text{--}315^\circ$, labelled by their lower longitude limit, from $-150 < V_{\text{LSR}} < +50 \text{ km s}^{-1}$. The dark solid lines are the Mopra ^{12}CO data, while the blue is the ^{13}CO emission offset by -0.2 K . The dashed lines are the equivalent average ^{12}CO spectra from the Columbia CO Survey (Dame et al., 2001), which show systematic lower line intensities by a factor of ~ 1.35 (see Table 2 for degree-specific values).

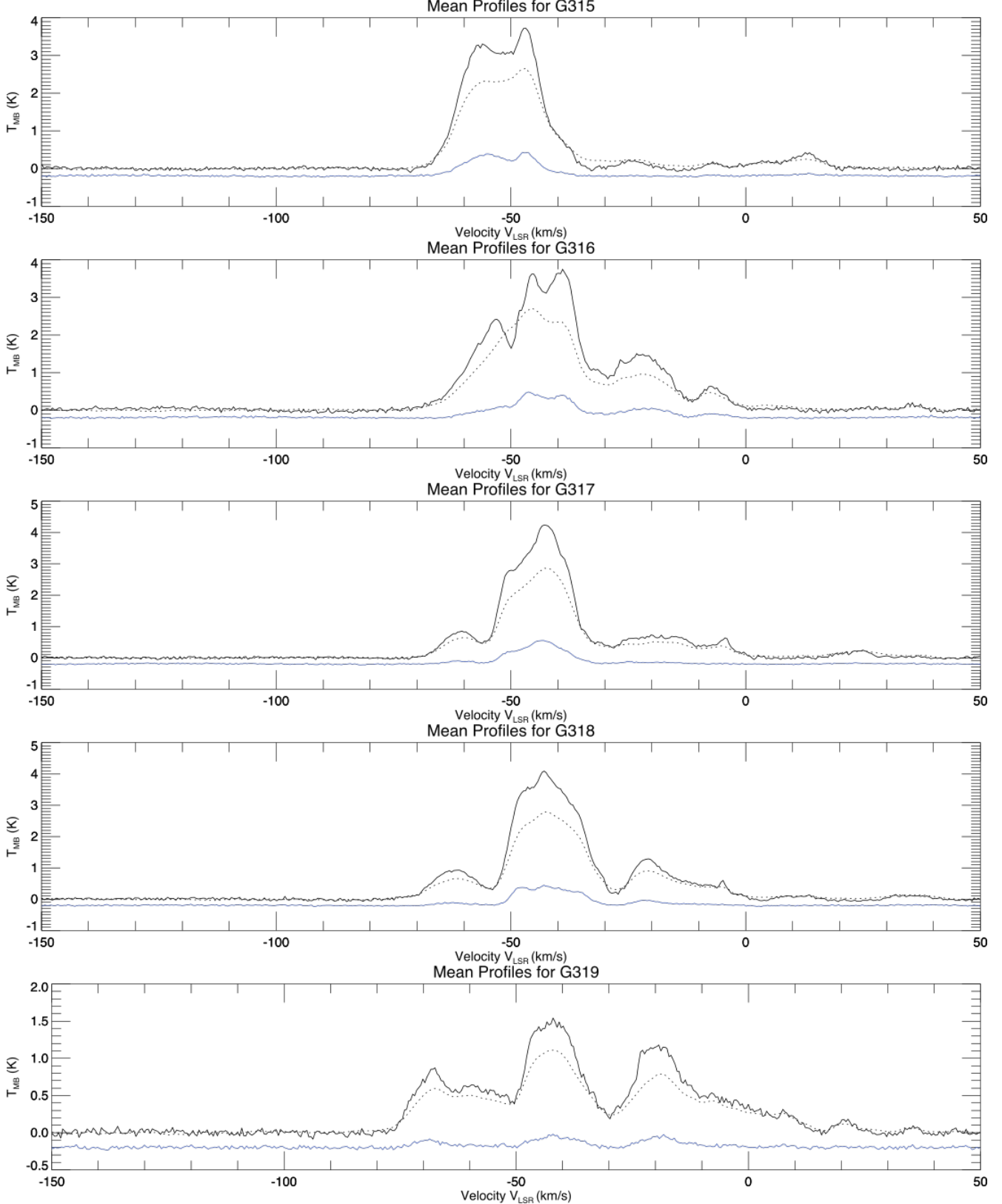


Figure 15. Average spectra for each square degree along the Galactic Plane between $l = 315\text{--}320^\circ$, labelled by their lower longitude limit, from $-150 < V_{LSR} < +50\text{ km s}^{-1}$. The dark solid lines are the Mopra ^{12}CO data, while the blue is the ^{13}CO emission offset by -0.2 K . The dashed lines are the equivalent average ^{12}CO spectra from the Columbia CO Survey (Dame et al., 2001), which show systematic lower line intensities by a factor of ~ 1.35 (see Table 2 for degree-specific values).

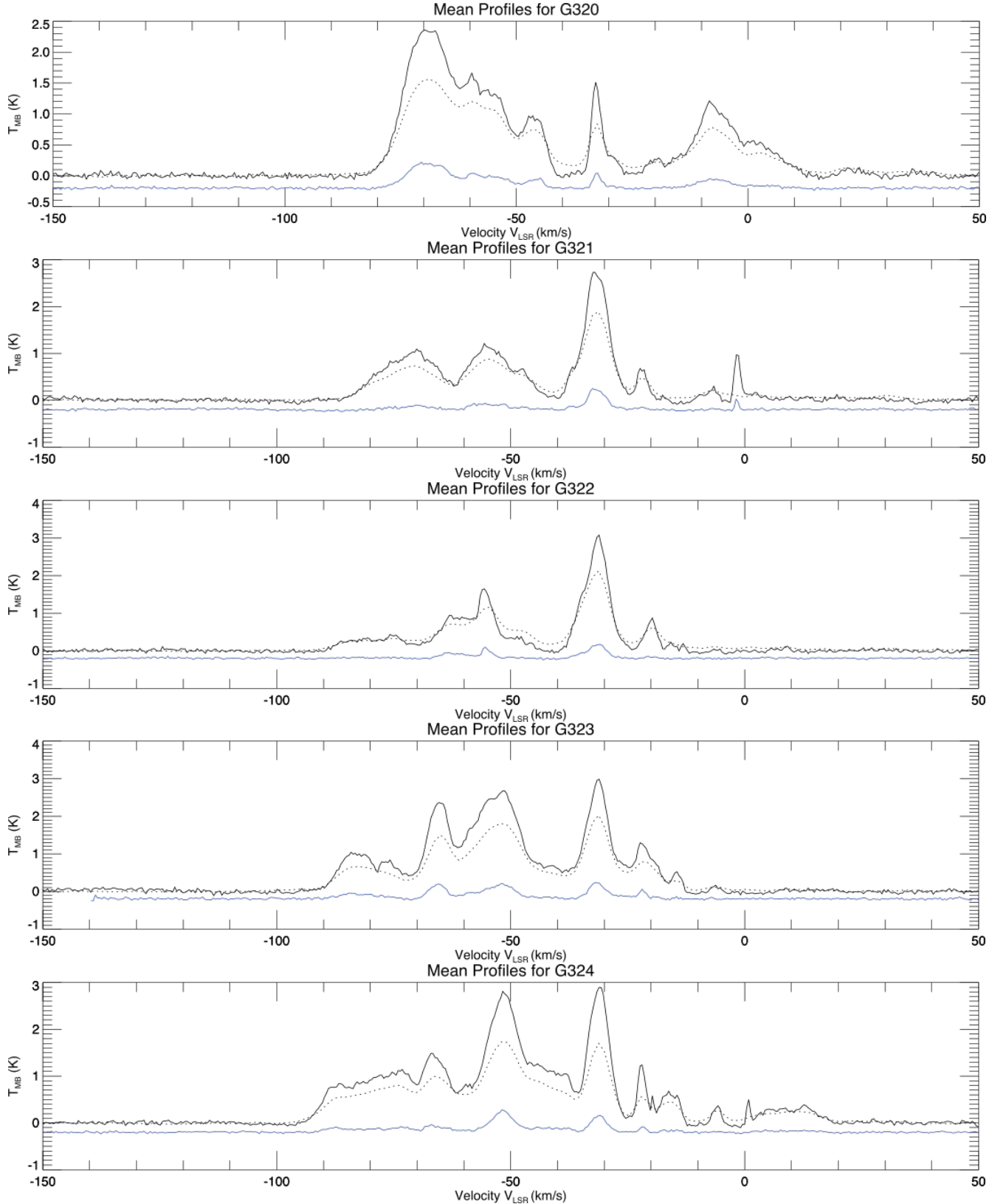


Figure 16. Average spectra for each square degree along the Galactic Plane between $l = 320\text{--}325^\circ$, labelled by their lower longitude limit, from $-150 < V_{\text{LSR}} < +50 \text{ km s}^{-1}$. The dark solid lines are the Mopra ^{12}CO data, while the blue is the ^{13}CO emission offset by -0.2 K . The dashed lines are the equivalent average ^{12}CO spectra from the Columbia CO Survey (Dame et al., 2001), which show systematic lower line intensities by a factor of ~ 1.35 (see Table 2 for degree-specific values).

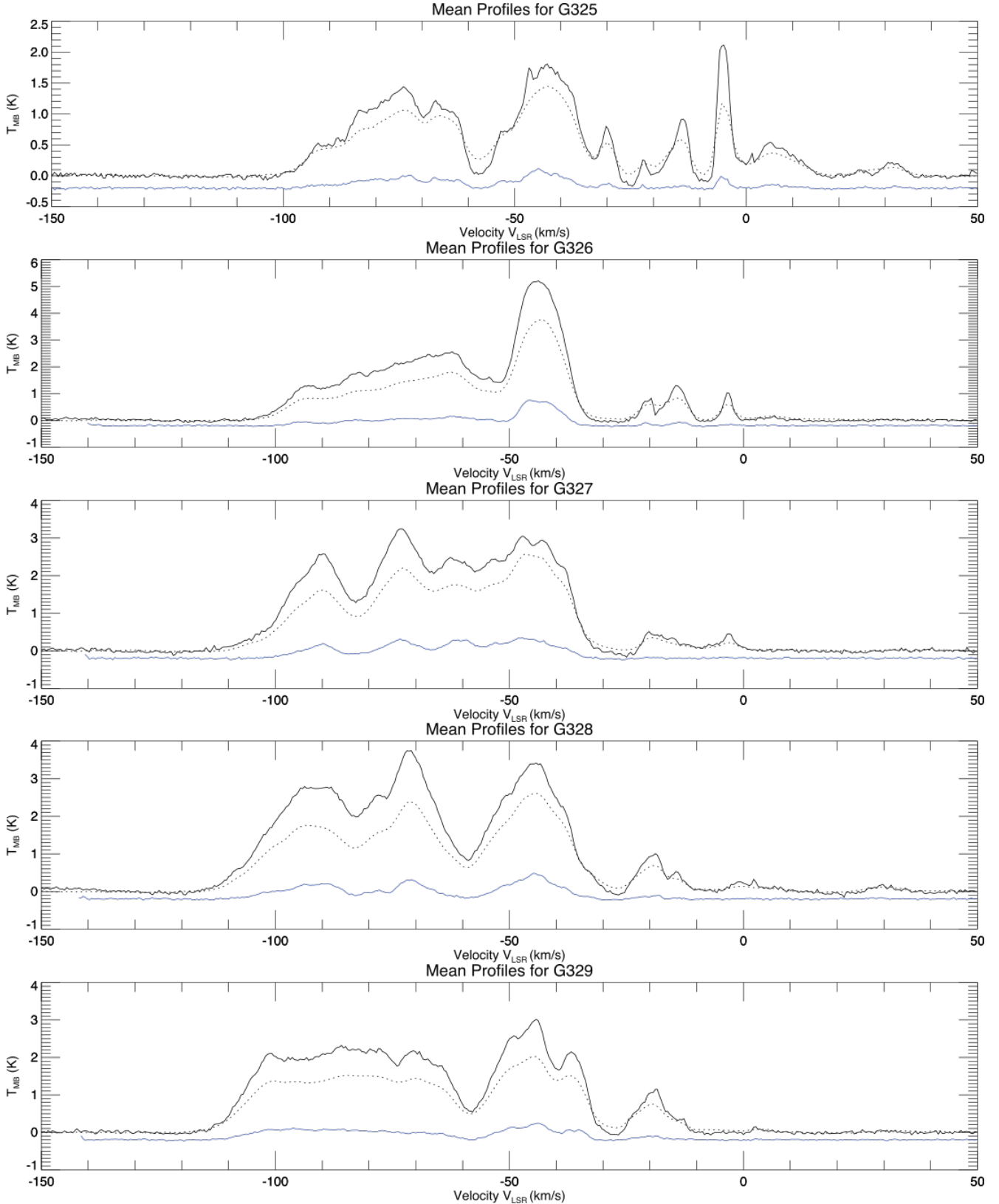


Figure 17. Average spectra for each square degree along the Galactic Plane between $l = 325\text{--}330^\circ$, labelled by their lower longitude limit, from $-150 < V_{LSR} < +50\text{ km s}^{-1}$. The dark solid lines are the Mopra ^{12}CO data, while the blue is the ^{13}CO emission offset by -0.2 K . The dashed lines are the equivalent average ^{12}CO spectra from the Columbia CO Survey (Dame et al., 2001), which show systematic lower line intensities by a factor of ~ 1.35 (see Table 2 for degree-specific values).

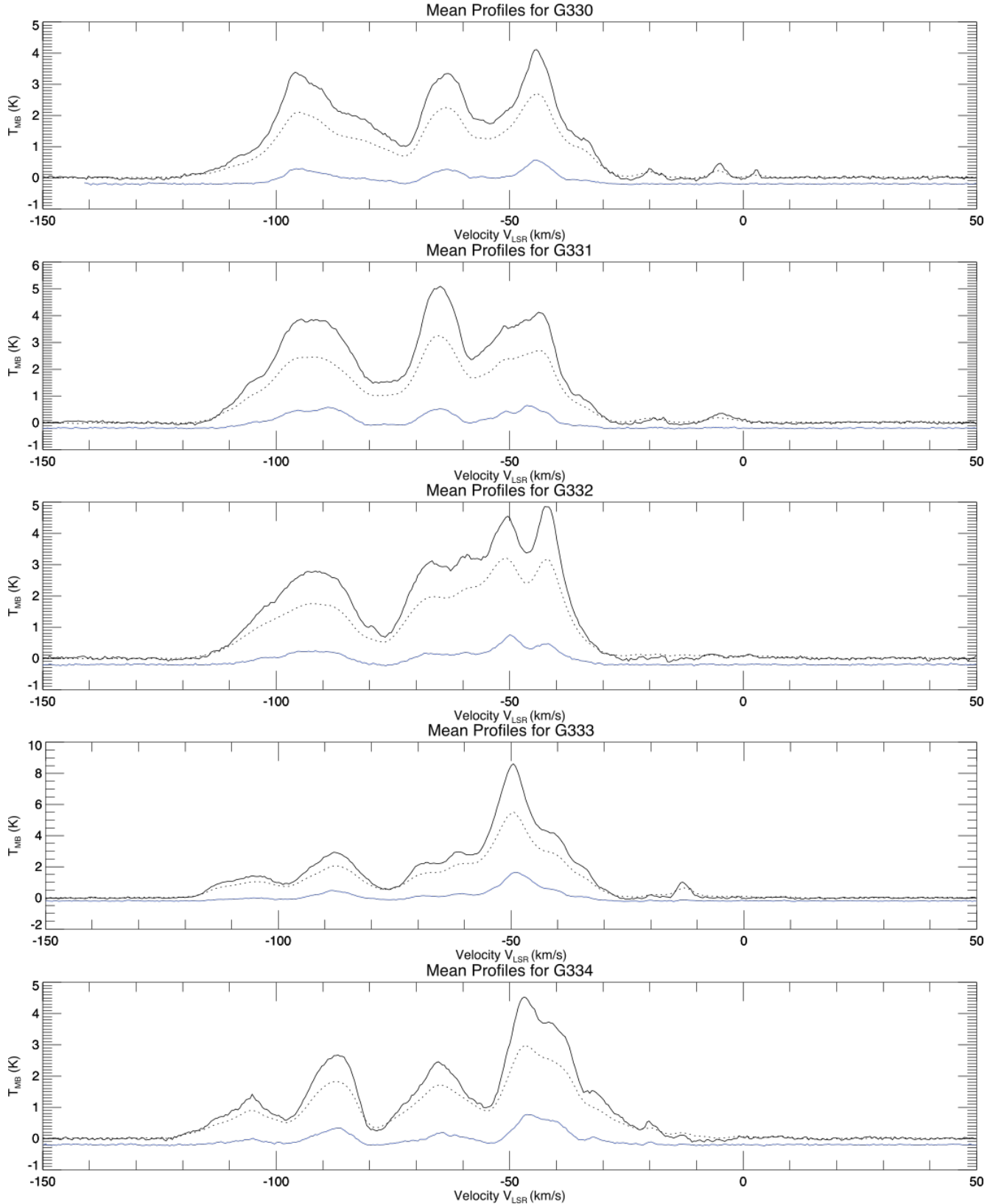


Figure 18. Average spectra for each square degree along the Galactic Plane between $l = 330\text{--}335^\circ$, labelled by their lower longitude limit, from $-150 < V_{LSR} < +50\text{ km s}^{-1}$. The dark solid lines are the Mopra ^{12}CO data, while the blue is the ^{13}CO emission offset by -0.2 K . The dashed lines are the equivalent average ^{12}CO spectra from the Columbia CO Survey (Dame et al., 2001), which show systematic lower line intensities by a factor of ~ 1.35 (see Table 2 for degree-specific values).

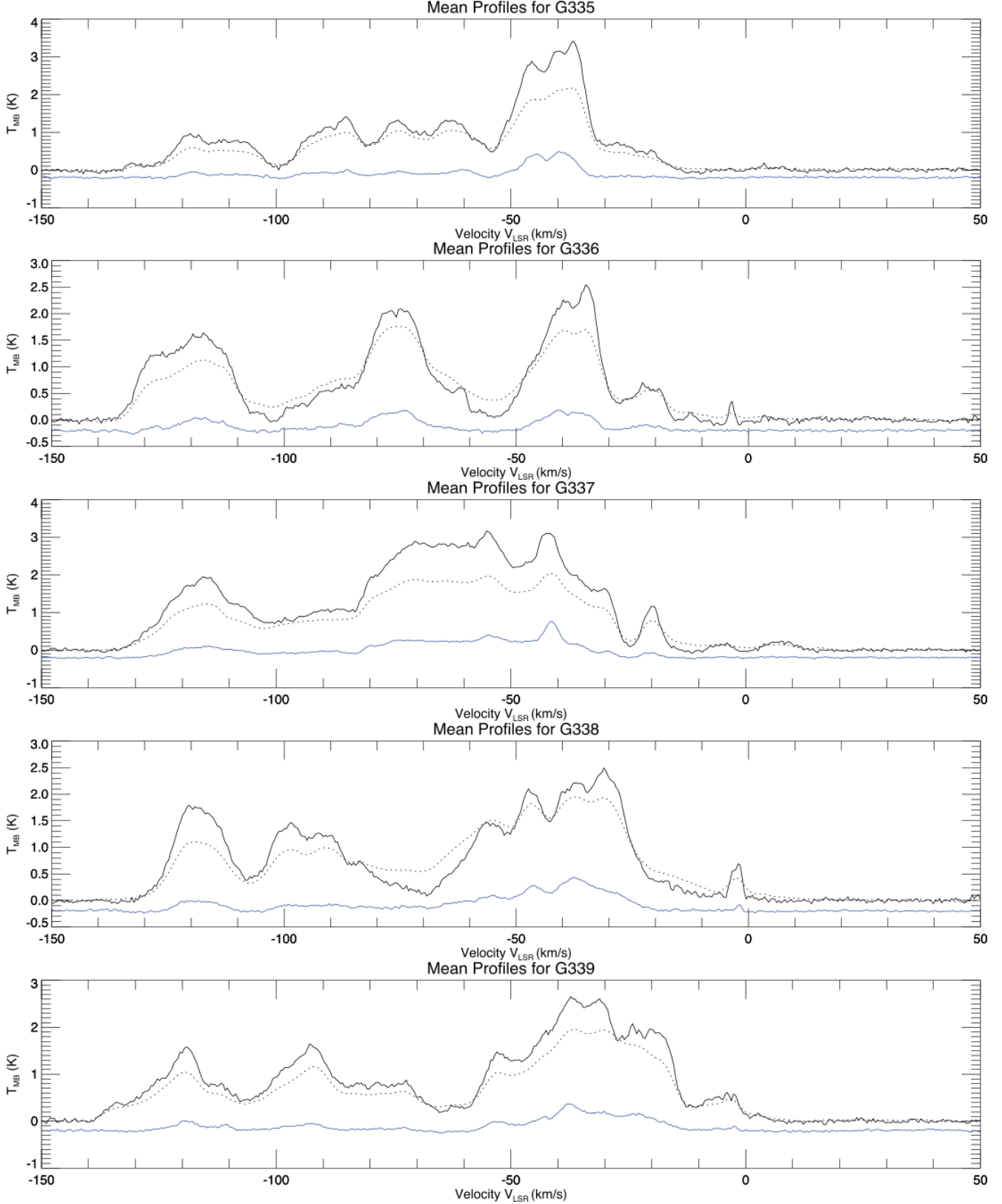


Figure 19. Average spectra for each square degree along the Galactic Plane between $l = 335\text{--}340^\circ$, labelled by their lower longitude limit, from $-150 < V_{LSR} < +50 \text{ km s}^{-1}$. The dark solid lines are the Mopra ^{12}CO data, while the blue is the ^{13}CO emission offset by -0.2 K . The dashed lines are the equivalent average ^{12}CO spectra from the Columbia CO Survey (Dame et al., 2001), which show systematic lower line intensities by a factor of ~ 1.35 (see Table 2 for degree-specific values).

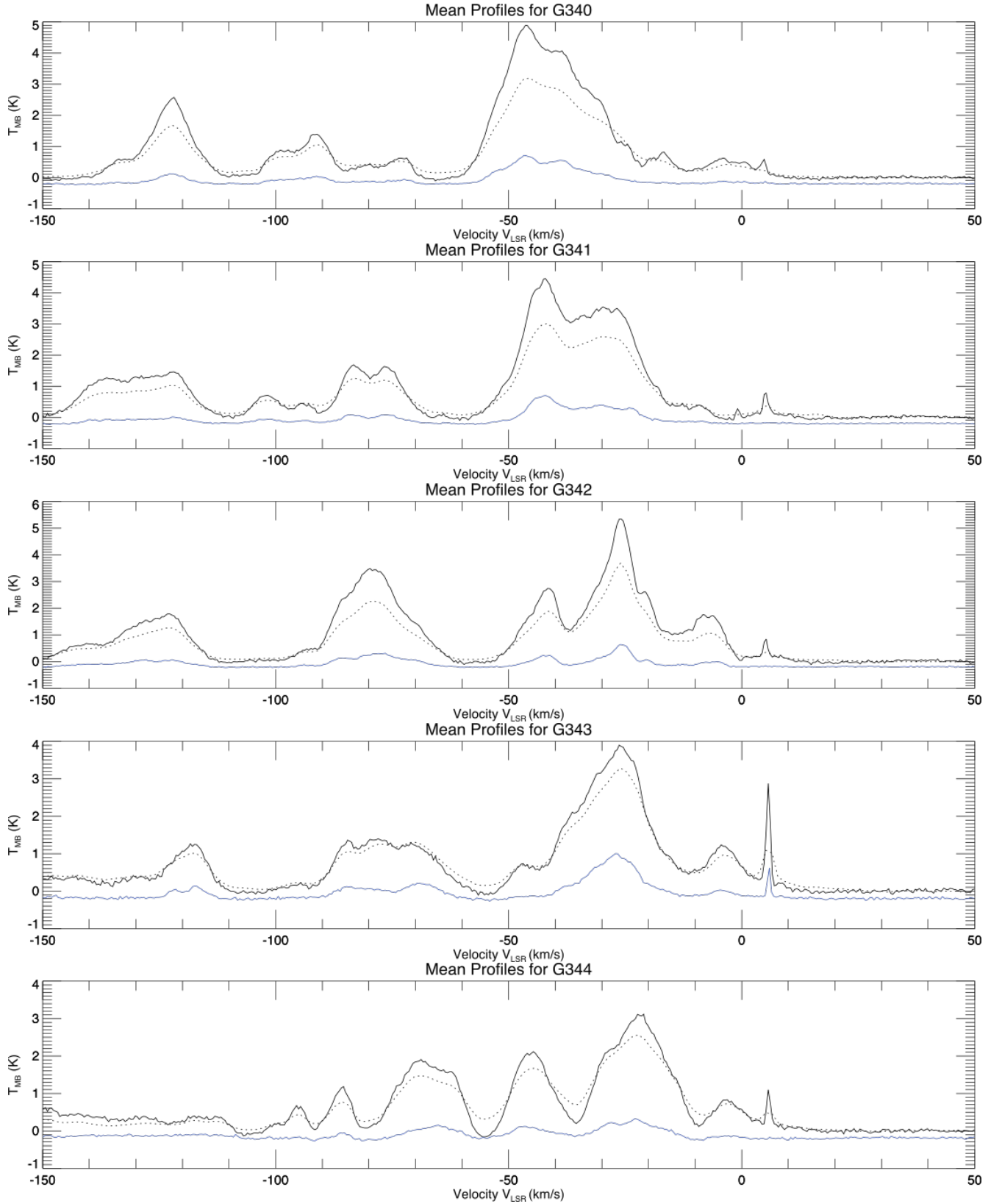


Figure 20. Average spectra for each square degree along the Galactic Plane between $l = 340\text{--}345^\circ$, labelled by their lower longitude limit, from $-150 < V_{\text{LSR}} < +50 \text{ km s}^{-1}$. The dark solid lines are the Mopra ^{12}CO data, while the blue is the ^{13}CO emission offset by -0.2 K . The dashed lines are the equivalent average ^{12}CO spectra from the Columbia CO Survey (Dame et al., 2001), which show systematic lower line intensities by a factor of ~ 1.35 (see Table 2 for degree-specific values).

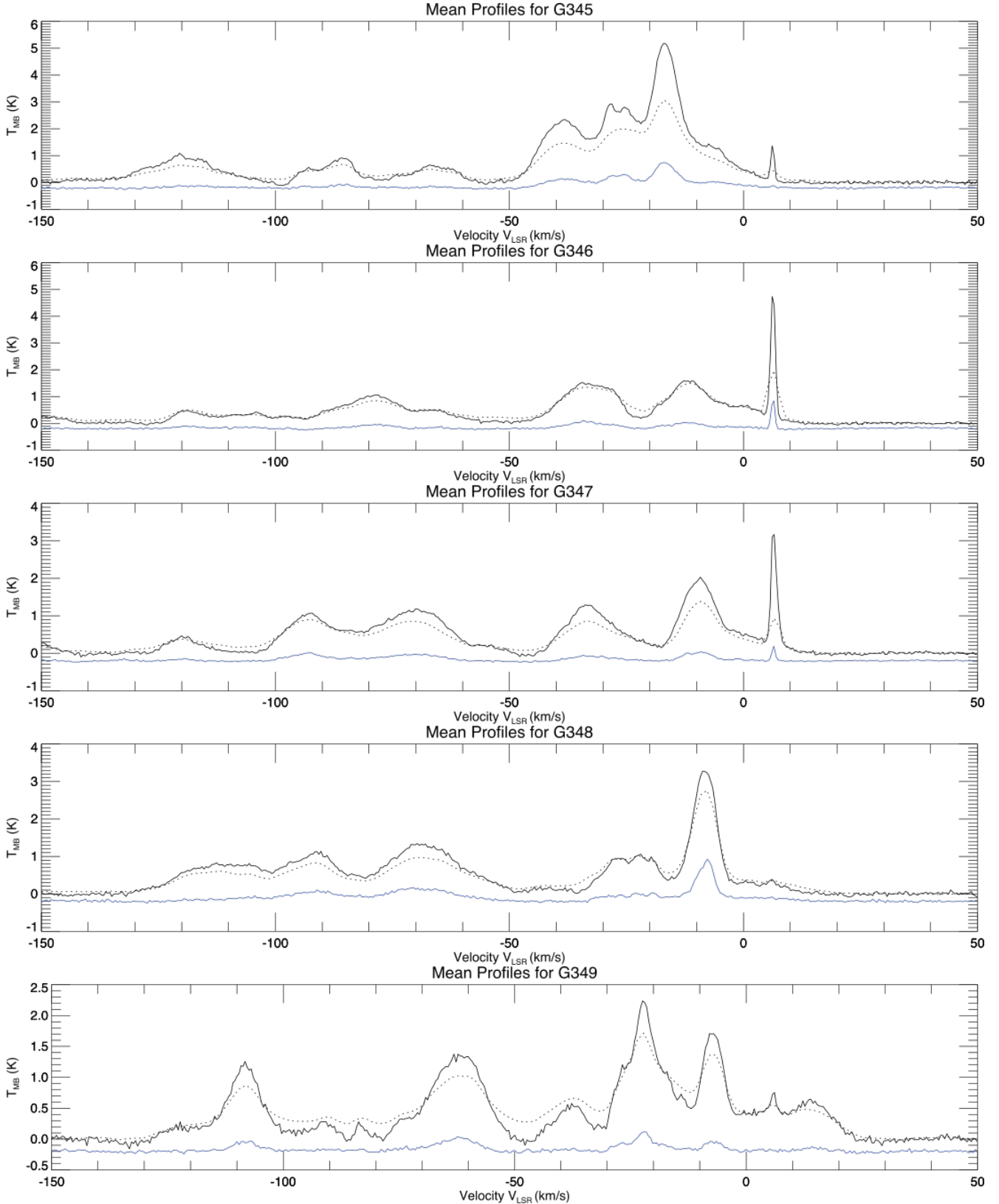


Figure 21. Average spectra for each square degree along the Galactic Plane between $l = 345\text{--}350^\circ$, labelled by their lower longitude limit, from $-150 < V_{LSR} < +50\text{ km s}^{-1}$. The dark solid lines are the Mopra ^{12}CO data, while the blue is the ^{13}CO emission offset by -0.2 K . The dashed lines are the equivalent average ^{12}CO spectra from the Columbia CO Survey (Dame et al., 2001), which show systematic lower line intensities by a factor of ~ 1.35 (see Table 2 for degree-specific values).

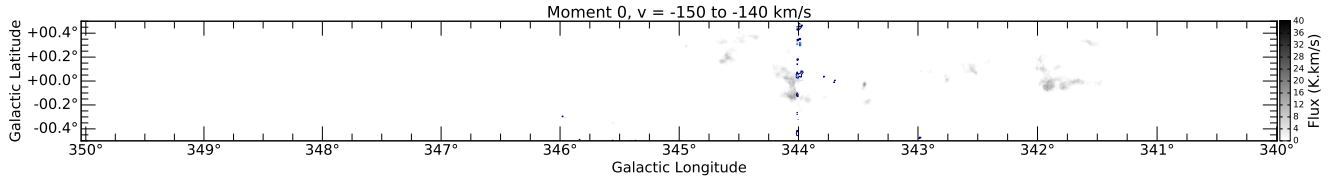


Figure 22. Moment 0 image for $l = 340\text{--}350^\circ$ calculated over the velocity interval $v = -150$ to -140 km s^{-1} using the main beam intensity, T_{MB} . The grayscale ^{12}CO image runs from 0 to 40 K.km/s, while the ^{13}CO contours are at 1, 6, 11, 16 K.km/s. None of the other data cubes demonstrate significant emission in this velocity range. Note that some scanning artefacts are present in this and following images, evident as 1° -long line features in longitude or latitude.

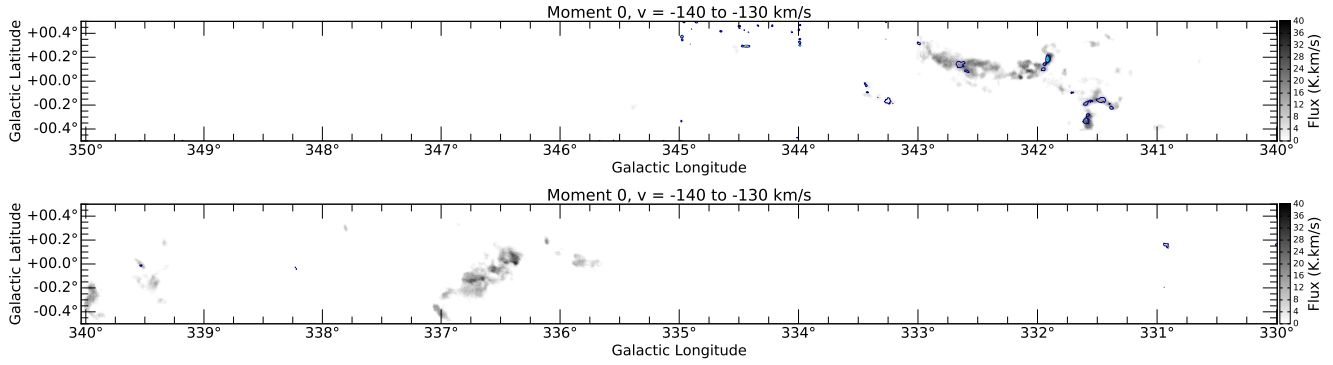


Figure 23. Moment 0 images for $l = 330\text{--}350^\circ$ calculated over the velocity interval $v = -140$ to -130 km s^{-1} . The grayscale ^{12}CO image runs from 0 to 40 K.km/s, while the ^{13}CO contours are at 1, 6, 11, 16 K.km/s. None of the other data cubes demonstrate significant emission in this velocity range.

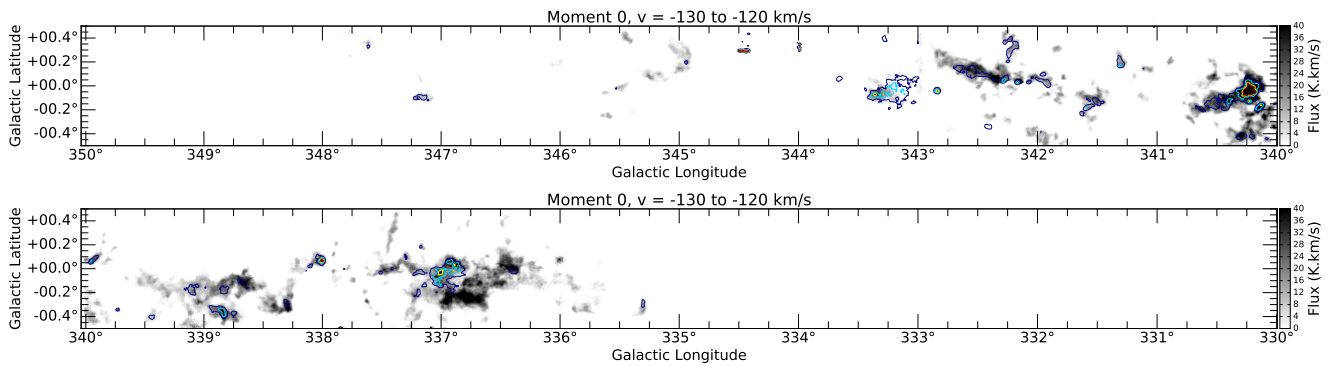


Figure 24. Moment 0 images for $l = 330\text{--}350^\circ$ calculated over the velocity interval $v = -130$ to -120 km s^{-1} . The grayscale ^{12}CO image runs from 0 to 40 K.km/s, while the ^{13}CO contours are at 1, 6, 11, 16 K.km/s. None of the other data cubes demonstrate significant emission in this velocity range.

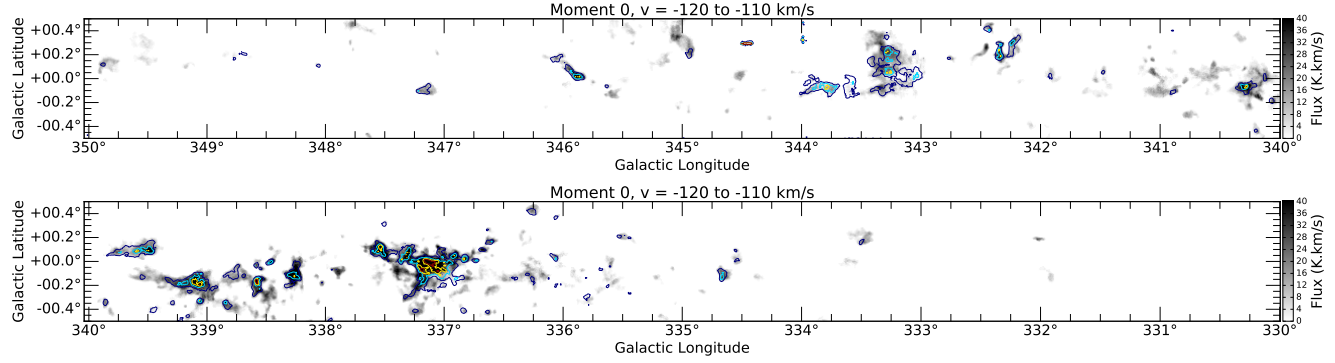


Figure 25. Moment 0 images for $l = 330\text{--}350^\circ$ calculated over the velocity interval $v = -120$ to -110 km s^{-1} . The grayscale ^{12}CO image runs from 0 to 40 K.km/s, while the ^{13}CO contours are at 1, 6, 11, 16 K.km/s. None of the other data cubes demonstrate significant emission in this velocity range.

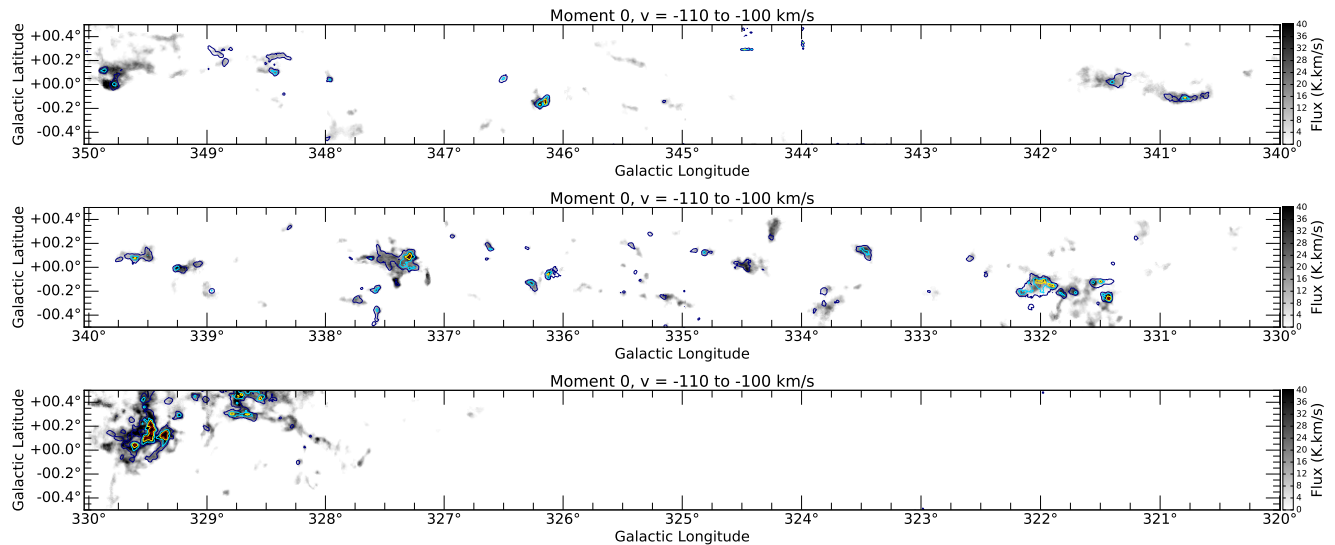


Figure 26. Moment 0 images for $l = 320\text{--}350^\circ$ calculated over the velocity interval $v = -110$ to -100 km s^{-1} . The grayscale ^{12}CO image runs from 0 to 40 K.km/s, while the ^{13}CO contours are at 1, 6, 11, 16 K.km/s. None of the other data cubes demonstrate significant emission in this velocity range.

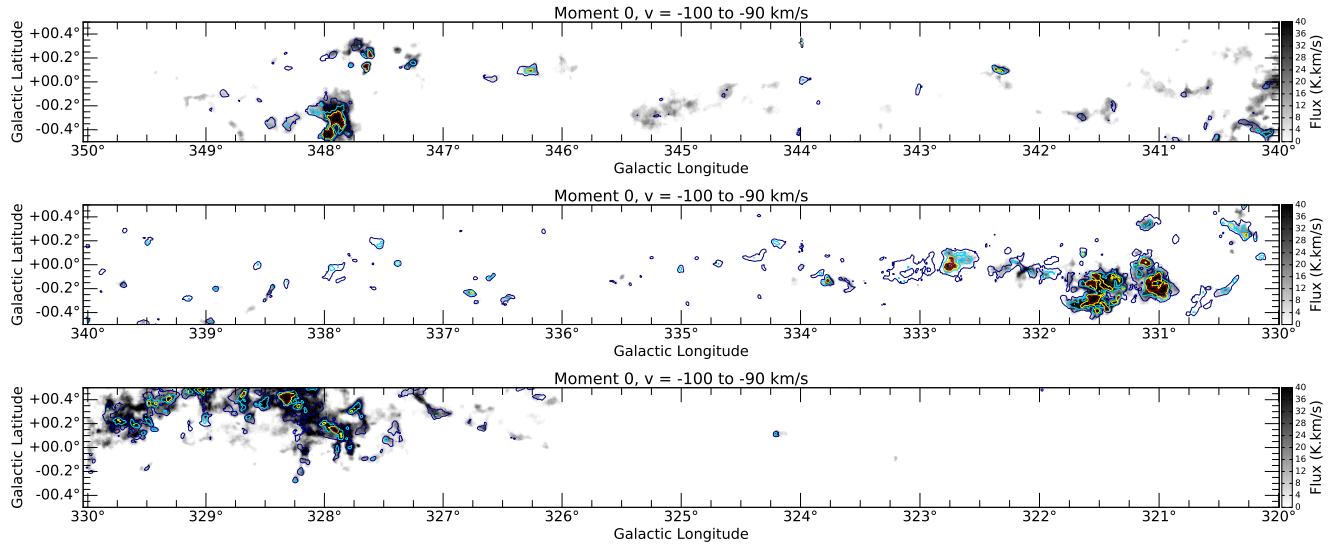


Figure 27. Moment 0 images for $l = 320\text{--}350^\circ$ calculated over the velocity interval $v = -100$ to -90 km s^{-1} . The grayscale ^{12}CO image runs from 0 to 40 K.km/s, while the ^{13}CO contours are at 1, 6, 11, 16 K.km/s. None of the other data cubes demonstrate significant emission in this velocity range.

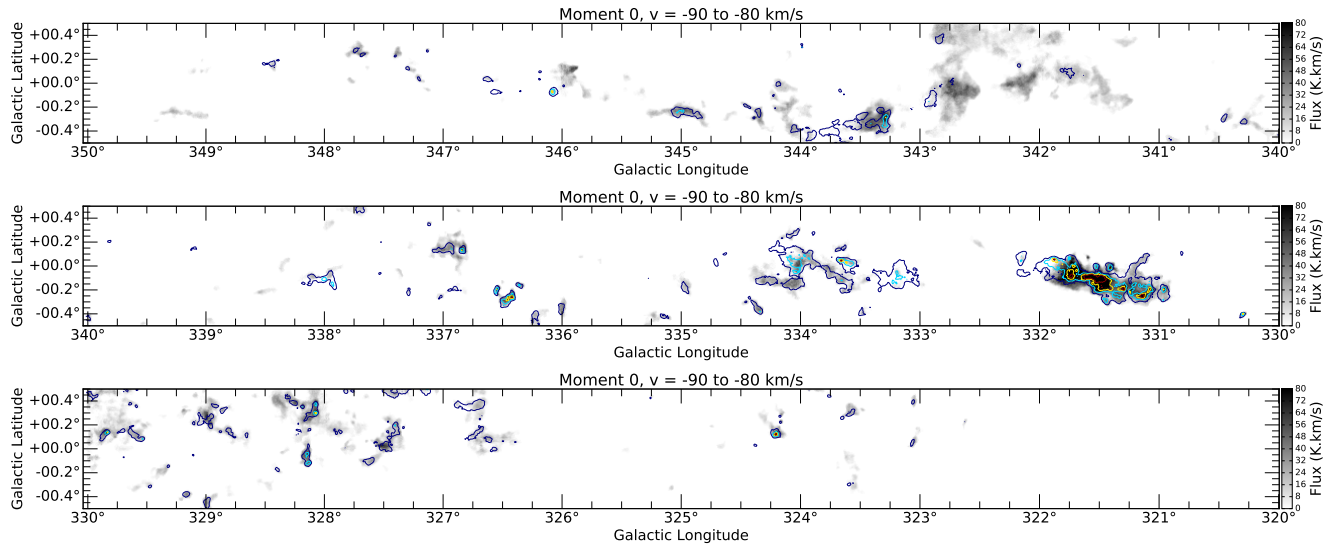


Figure 28. Moment 0 images for $l = 320\text{--}350^\circ$ calculated over the velocity interval $v = -90$ to -80 km s^{-1} . Note that the scales have changed here from previous images: the grayscale ^{12}CO image now runs from 0 to 80 K.km/s, while the ^{13}CO contours are at 4, 12, 20, 28 K.km/s. None of the other data cubes demonstrate significant emission in this velocity range.

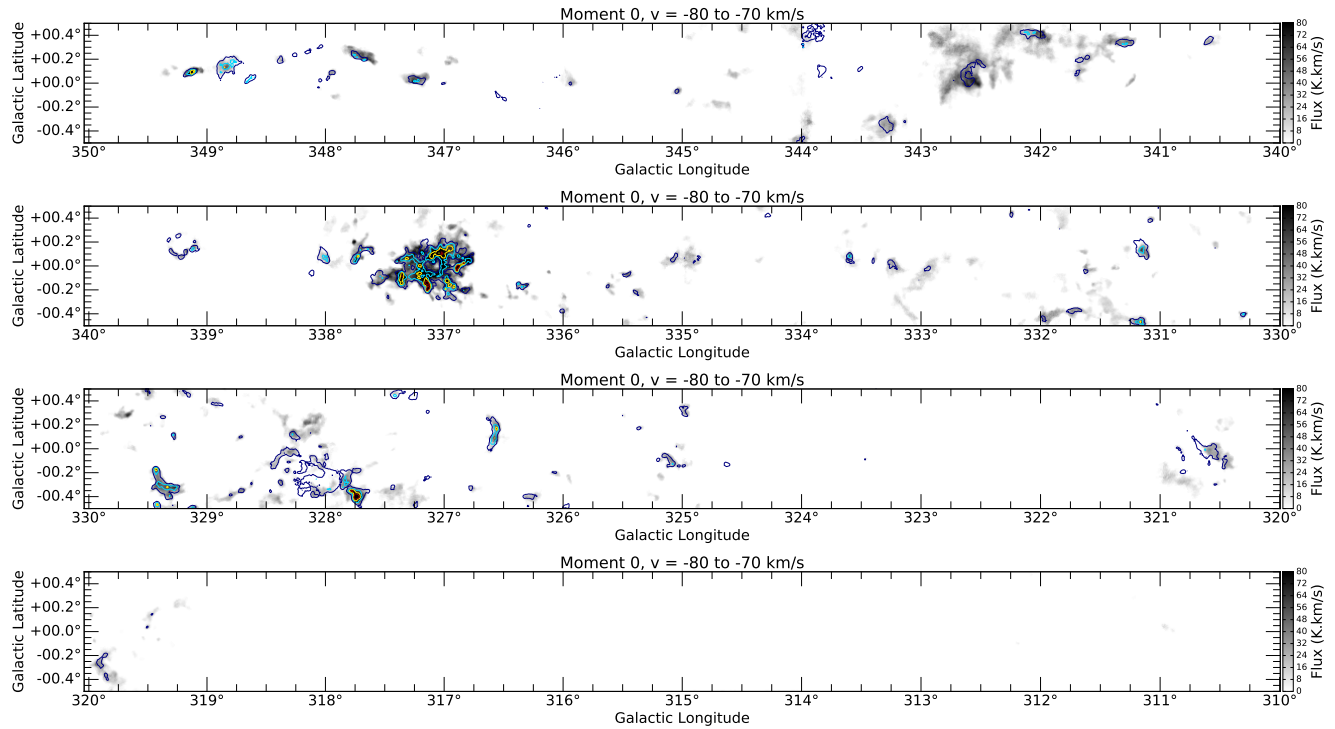


Figure 29. Moment 0 images for $l = 310\text{--}350^\circ$ calculated over the velocity interval $v = -80$ to -70 km s^{-1} . The grayscale ^{12}CO image runs from 0 to 80 K.km/s, while the ^{13}CO contours are at 4, 12, 20, 28 K.km/s. None of the other data cubes demonstrate significant emission in this velocity range.

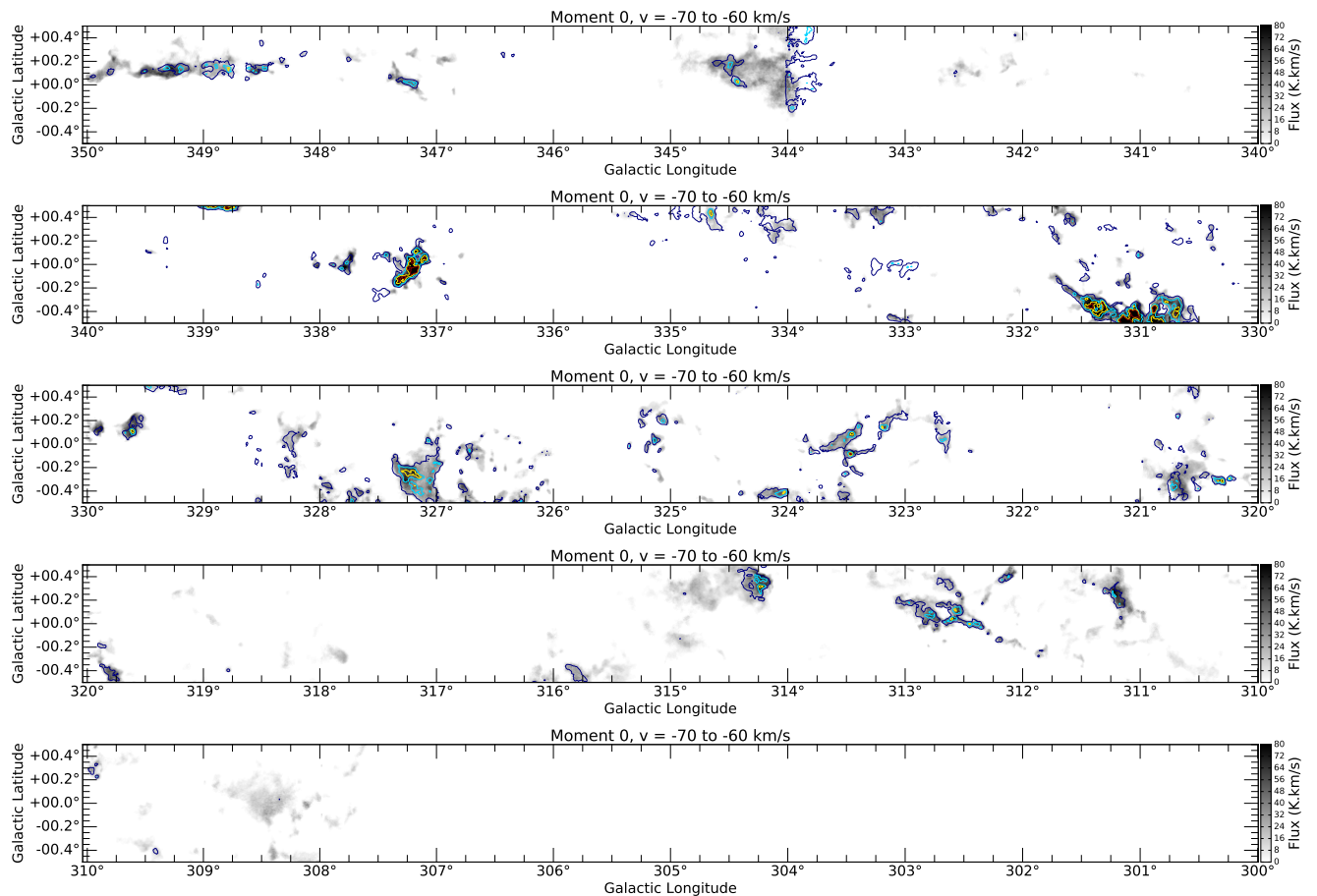


Figure 30. Moment 0 images for $l = 300\text{--}350^\circ$ calculated over the velocity interval $v = -70$ to -60 km s^{-1} . The grayscale ^{12}CO image runs from 0 to 80 K.km/s, while the ^{13}CO contours are at 4, 12, 20, 28 K.km/s.

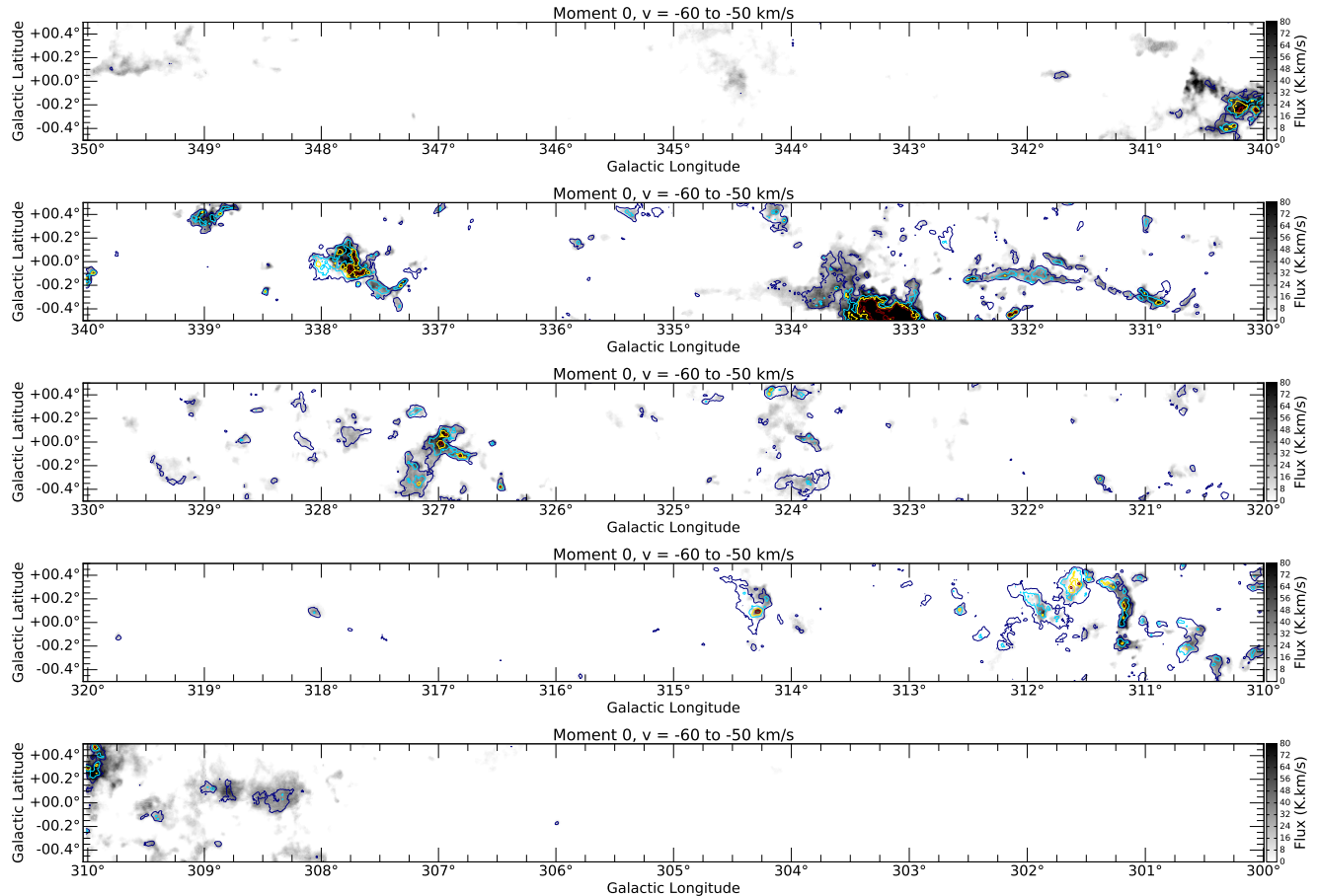


Figure 31. Moment 0 images for $l = 300\text{--}350^\circ$ calculated over the velocity interval $v = -60$ to -50 km s^{-1} . The grayscale ^{12}CO image runs from 0 to 80 K.km/s, while the ^{13}CO contours are at 4, 12, 20, 28 K.km/s.

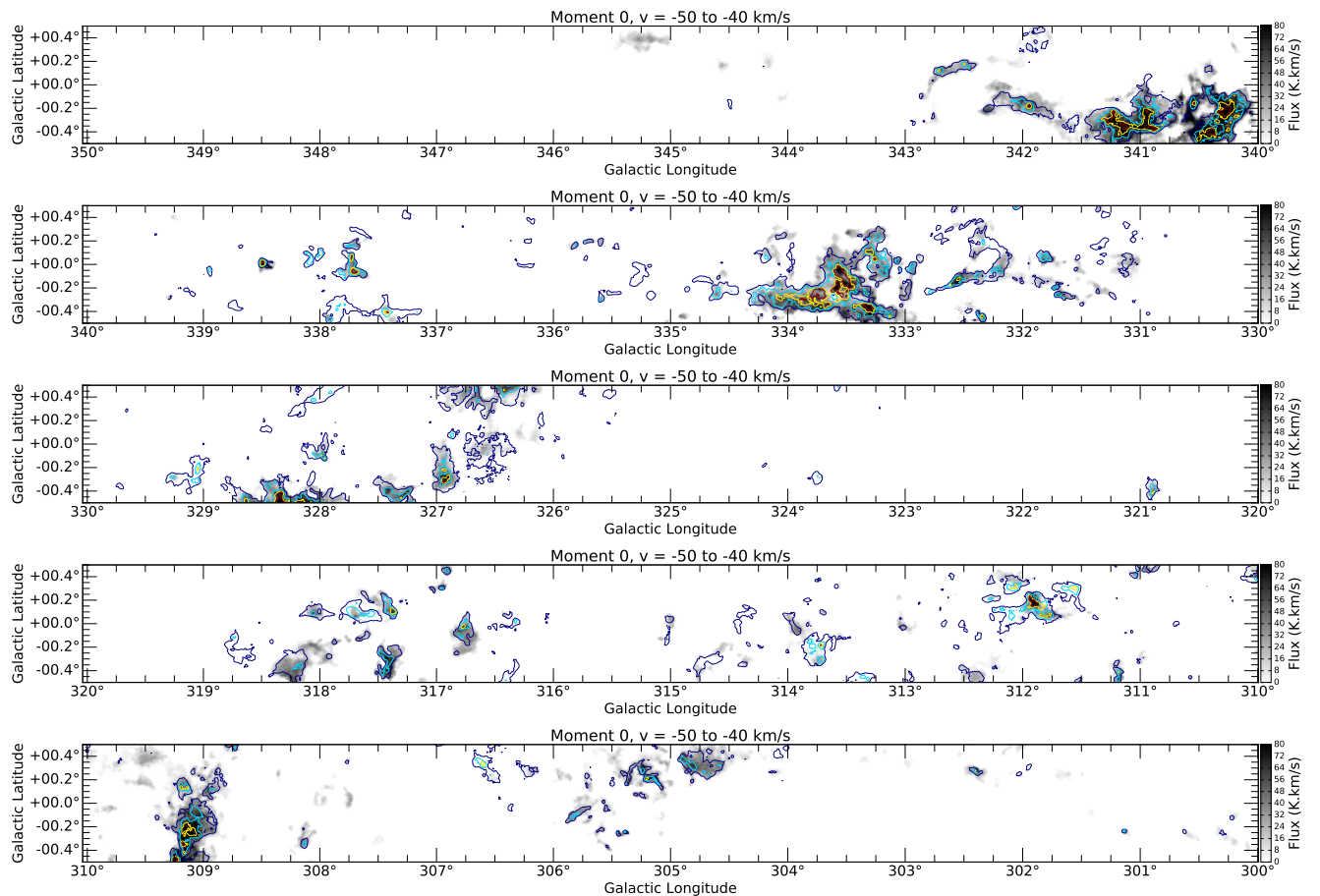


Figure 32. Moment 0 images for $l = 300\text{--}350^\circ$ calculated over the velocity interval $v = -50\text{ to }-40 \text{ km s}^{-1}$. The grayscale ^{12}CO image runs from 0 to 80 K.km/s, while the ^{13}CO contours are at 4, 12, 20, 28 K.km/s.

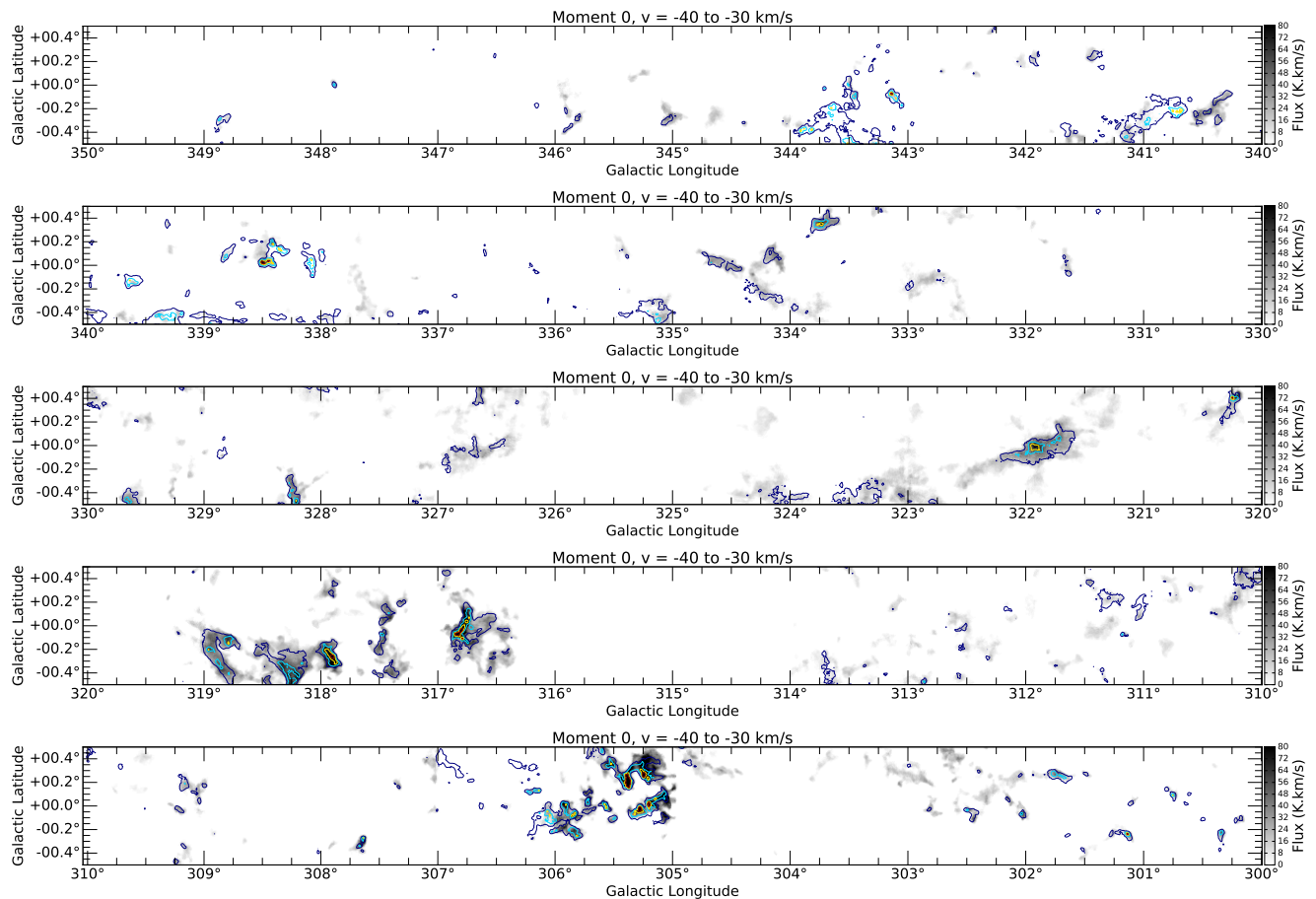


Figure 33. Moment 0 images for $l = 300\text{--}350^\circ$ calculated over the velocity interval $v = -40$ to -30 km s^{-1} . The grayscale ^{12}CO image runs from 0 to 80 K.km/s, while the ^{13}CO contours are at 4, 12, 20, 28 K.km/s.

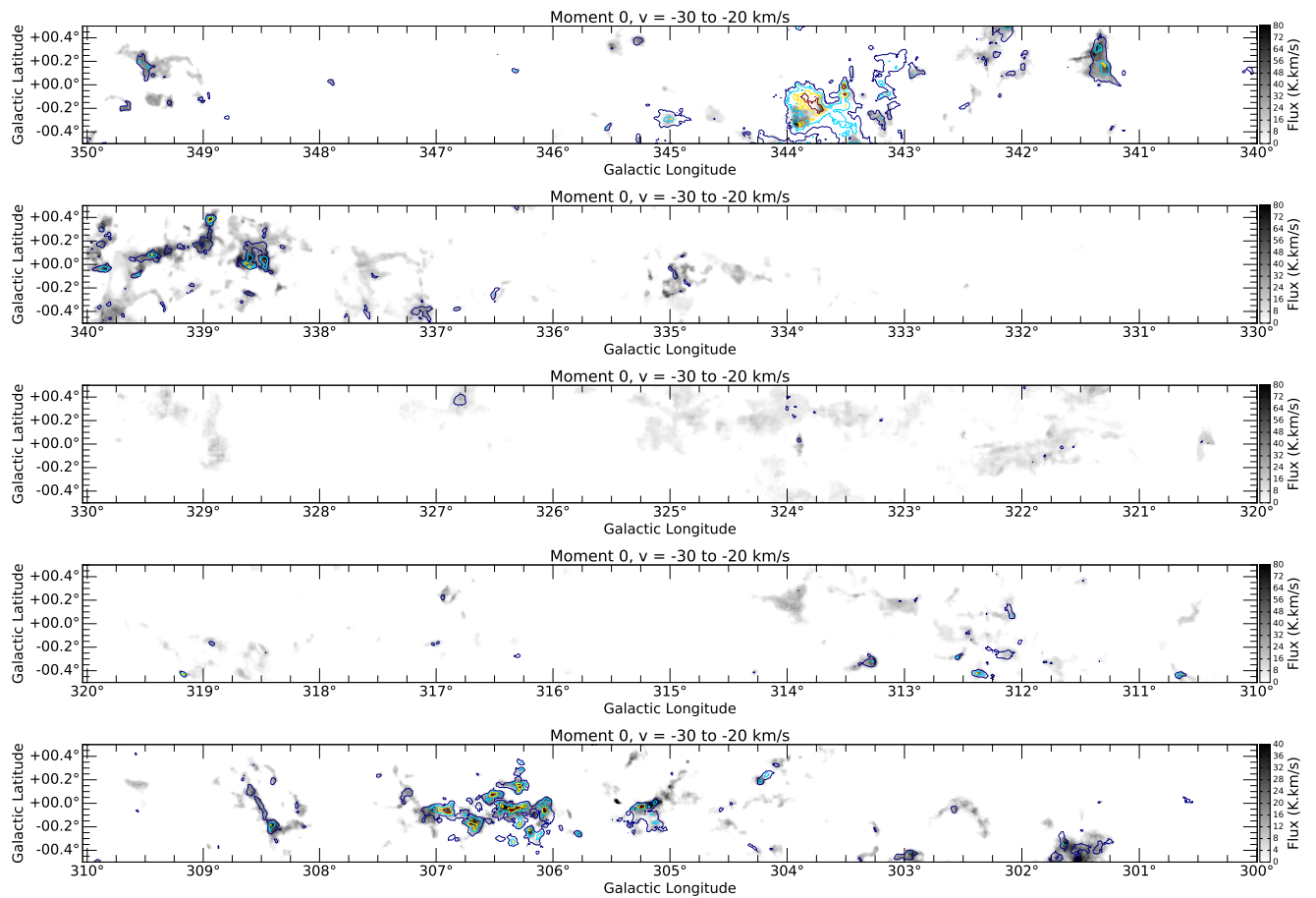


Figure 34. Moment 0 images for $l = 300\text{--}350^\circ$ calculated over the velocity interval $v = -30$ to -20 km s^{-1} . The grayscale ^{12}CO image runs from 0 to 80 K.km/s, while the ^{13}CO contours are at 4, 12, 20, 28 K.km/s.

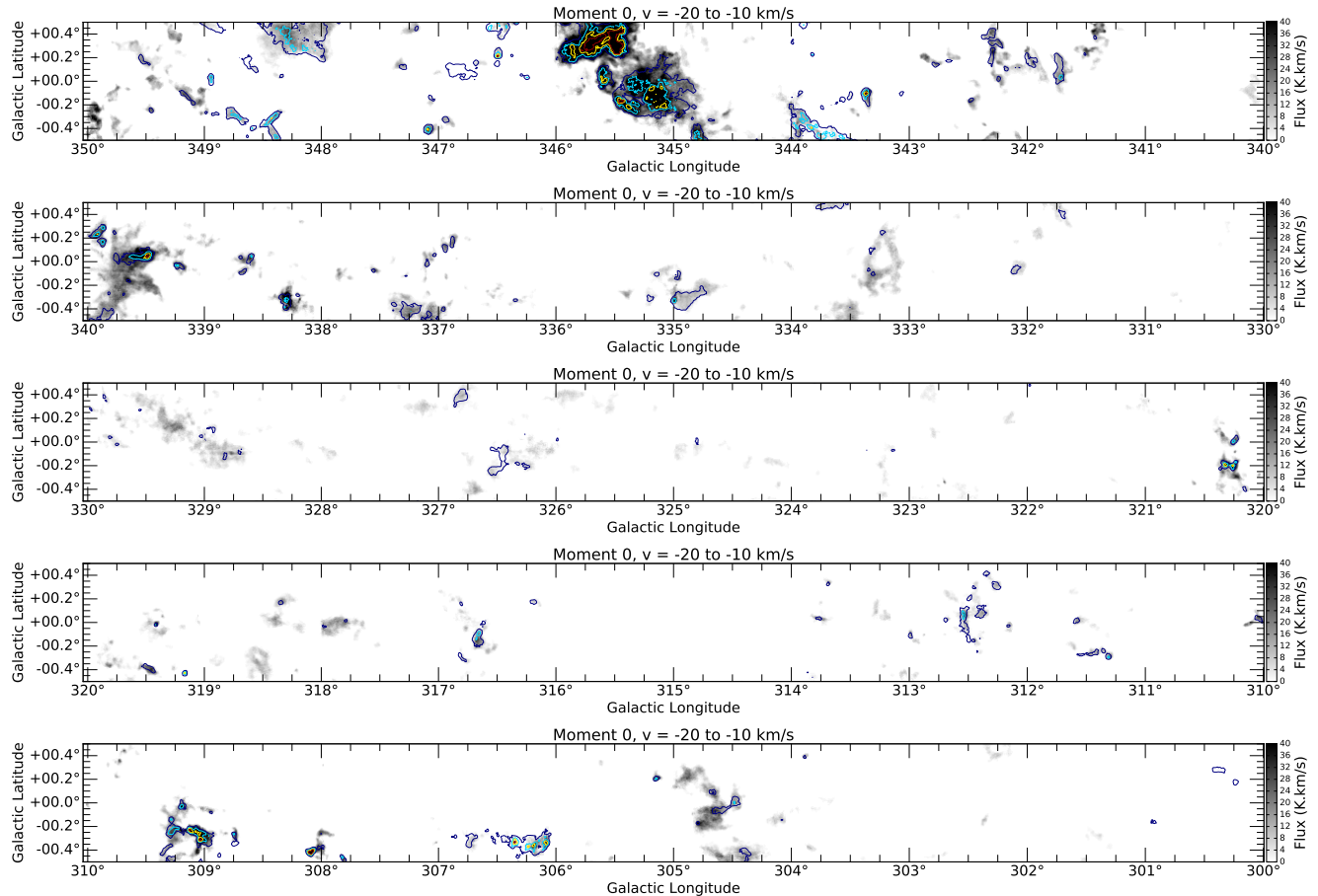


Figure 35. Moment 0 images for $l = 300\text{--}350^\circ$ calculated over the velocity interval $v = -20\text{ to }-10 \text{ km s}^{-1}$. The scales have changed again, the grayscale ^{12}CO image runs from 0 to 40 K.km/s, while the ^{13}CO contours are at 1, 6, 11, 16 K.km/s.

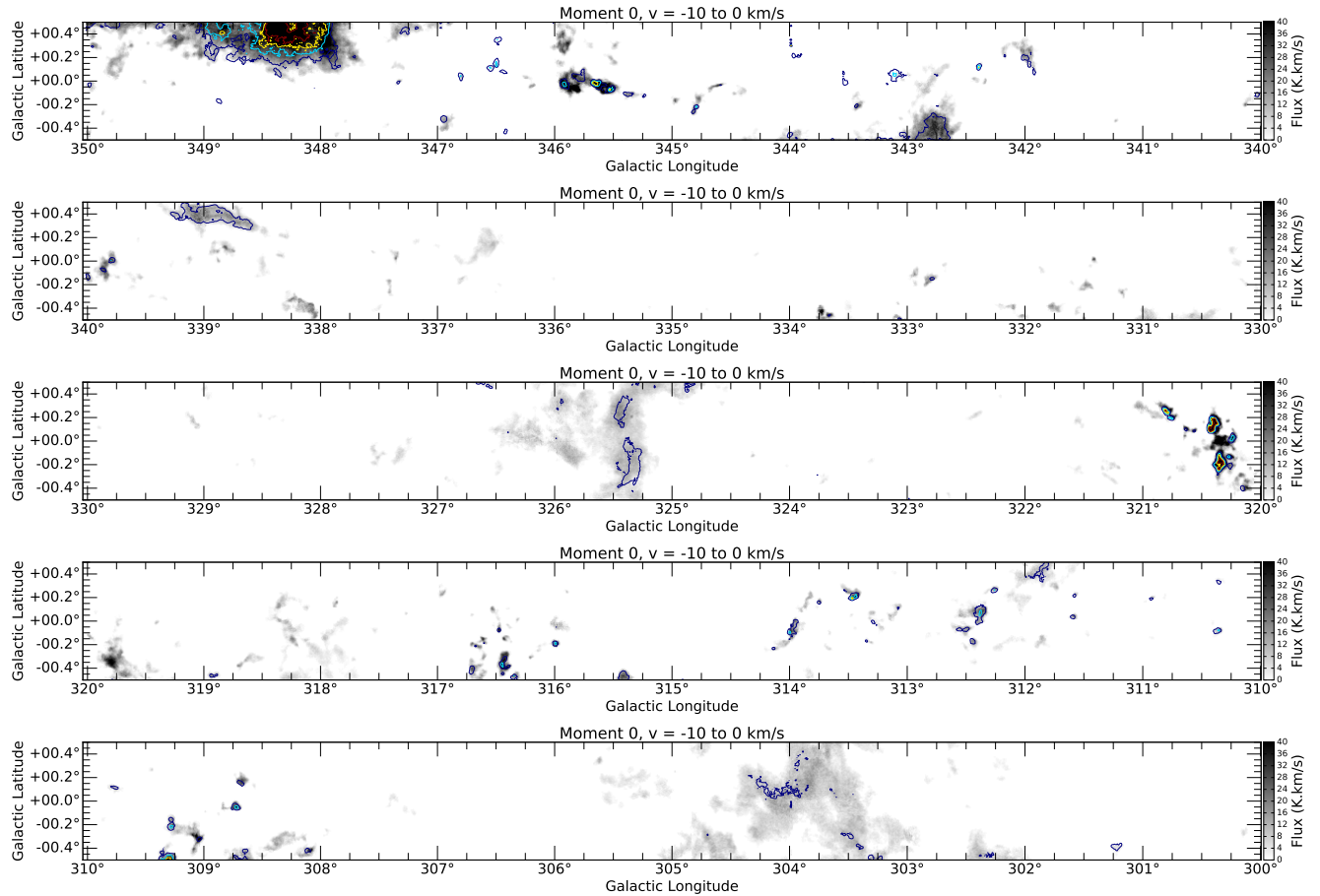


Figure 36. Moment 0 images for $l = 300\text{--}350^\circ$ calculated over the velocity interval $v = -10$ to 0 km s^{-1} . The grayscale ^{12}CO image runs from 0 to 40 K.km/s, while the ^{13}CO contours are at 1, 6, 11, 16 K.km/s.

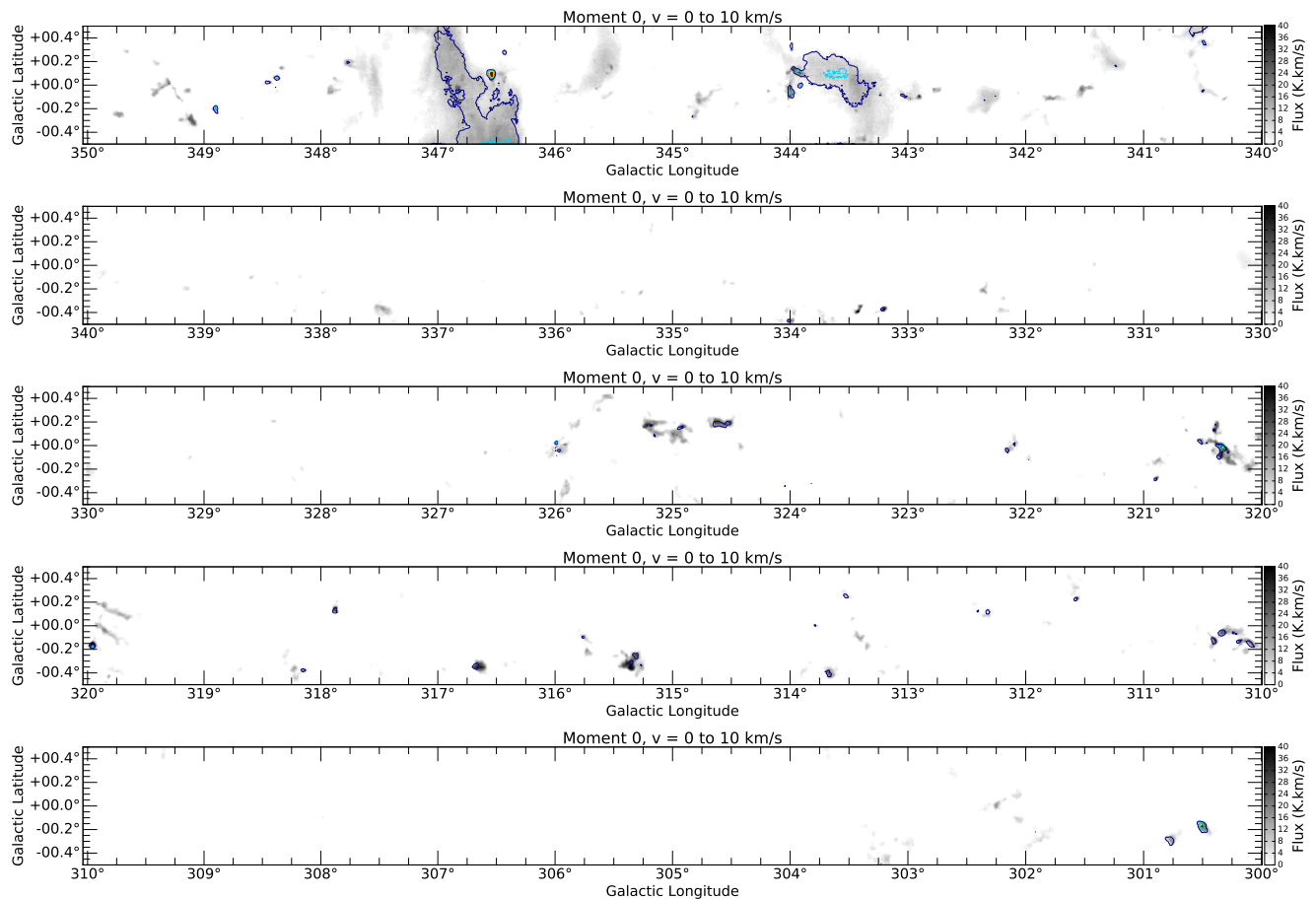


Figure 37. Moment 0 images for $l = 300\text{--}350^\circ$ calculated over the velocity interval $v = 0$ to $+10 \text{ km s}^{-1}$. The grayscale ^{12}CO image runs from 0 to 40 K.km/s, while the ^{13}CO contours are at 1, 6, 11, 16 K.km/s.

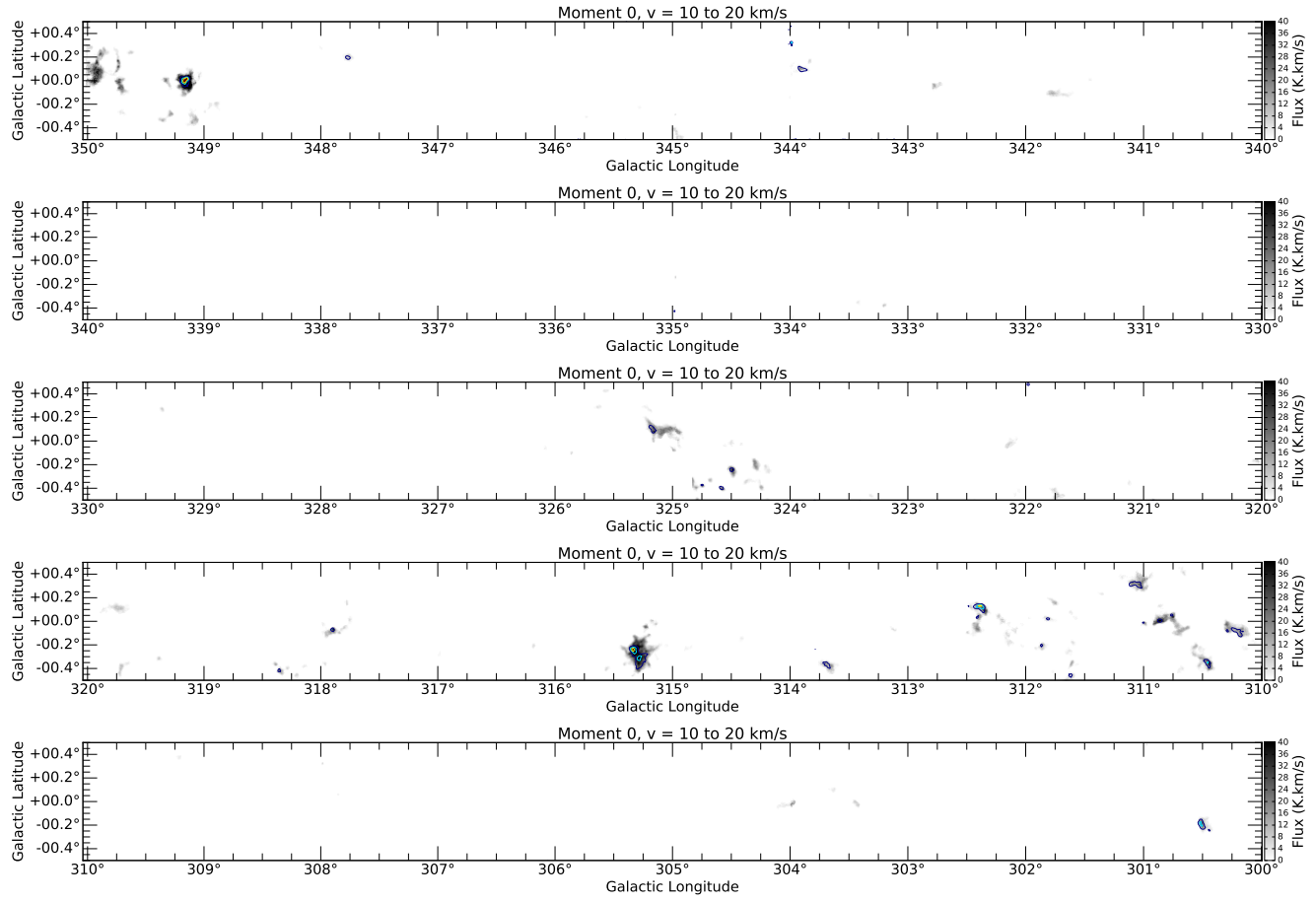


Figure 38. Moment 0 images for $l = 300\text{--}350^\circ$ calculated over the velocity interval $v = +10$ to $+20 \text{ km s}^{-1}$. The grayscale ^{12}CO image runs from 0 to 40 K.km/s, while the ^{13}CO contours are at 1, 6, 11, 16 K.km/s.

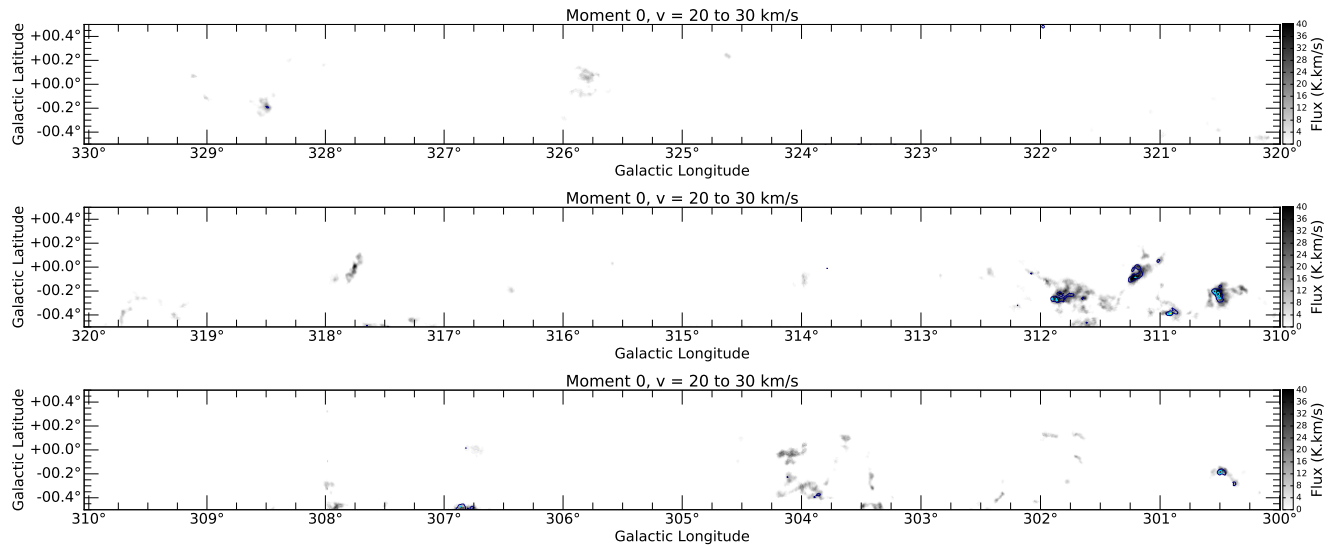


Figure 39. Moment 0 images for $l = 300\text{--}330^\circ$ calculated over the velocity interval $v = +20$ to $+30 \text{ km s}^{-1}$. The grayscale ^{12}CO image runs from 0 to 40 K.km/s, while the ^{13}CO contours are at 1, 6, 11, 16 K.km/s. None of the other data cubes demonstrate significant emission in this velocity range.

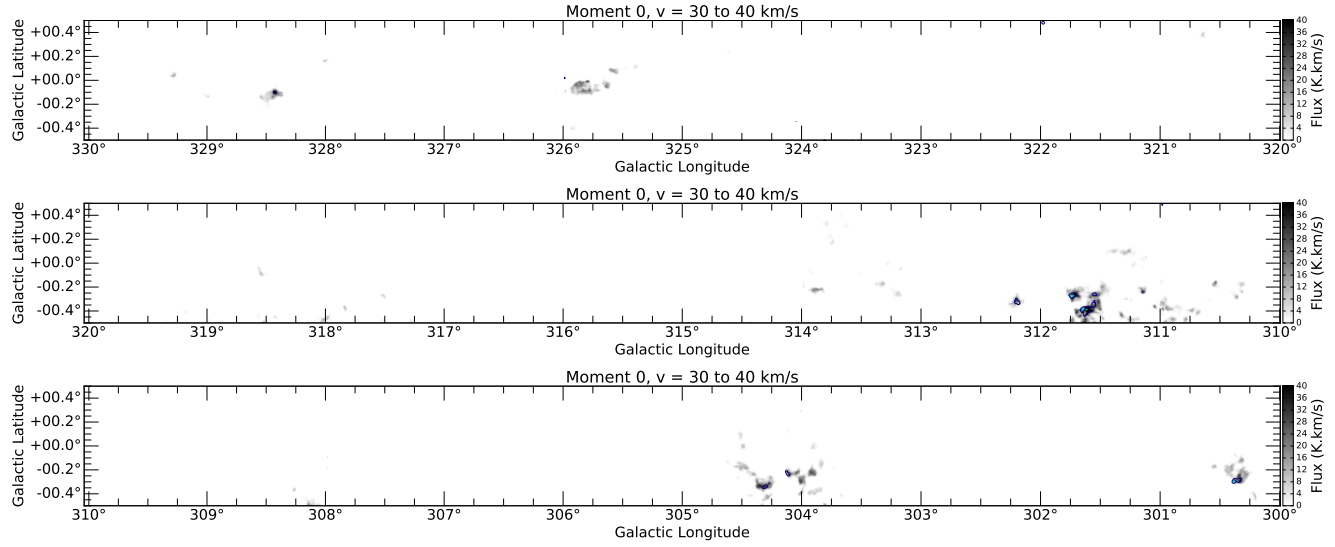


Figure 40. Moment 0 images for $l = 300\text{--}330^\circ$ calculated over the velocity interval $v = +30$ to $+40 \text{ km s}^{-1}$. The grayscale ^{12}CO image runs from 0 to 40 K.km/s, while the ^{13}CO contours are at 1, 6, 11, 16 K.km/s. None of the other data cubes demonstrate significant emission in this velocity range.

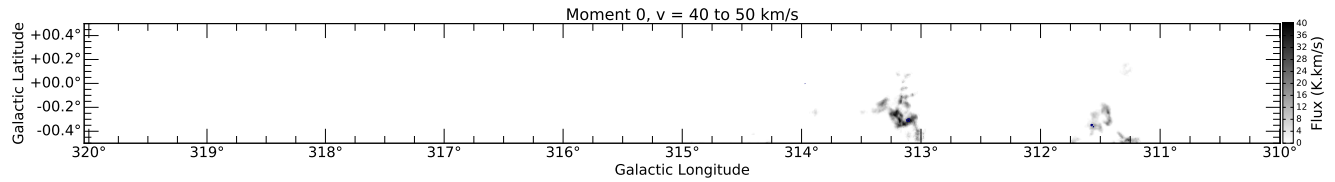


Figure 41. Moment 0 images for $l = 310\text{--}320^\circ$ calculated over the velocity interval $v = +40$ to $+50 \text{ km s}^{-1}$. The grayscale ^{12}CO image runs from 0 to 40 K.km/s, while the ^{13}CO contours are at 1, 6, 11, 16 km s^{-1} . None of the other data cubes demonstrate significant emission in this velocity range.

Table 3 C¹⁸O clump statistics within the $330 \leq l \leq 340^\circ$ block (see Section 4.3). For each clump we provide a Clump ID based upon its Galactic coordinates l , b and V_{LSR} , while Δl , Δb and ΔV indicate the clump FWHM extensions along the Galactic longitude, latitude, and velocity axes respectively. The clump radius, R , is reported in arcsec; the area A is that covered by the clump in the moment zero map; and A_{fwhm} is the area of an ellipse with semi-axes Δl and Δb . The near and far distances to the cloud centroid are listed in kpc as D^N and D^F respectively, calculated using the model in §4.2. The mean and peak clump brightness temperatures are given by $\overline{T}_{\text{MB}}^{18}$ and $\widehat{T}_{\text{MB}}^{18}$ respectively; the mean and peak column densities, $\overline{N_{\text{H}_2}}$ and $\widehat{N_{\text{H}_2}}$, are calculated as described in §4.3. Finally we report the mass of each clump, calculated at both the near (M_{18}^N) and far (M_{18}^F) distances.

Clump ID	Coordinates		V_{LSR}	Δl	Δb	ΔV	R	A	A_{fwhm}	D^N	D^F	$\overline{T}_{\text{MB}}^{18}$	$\widehat{T}_{\text{MB}}^{18}$	$\overline{N_{\text{H}_2}}$	$\widehat{N_{\text{H}_2}}$	M_{18}^N	M_{18}^F
	l deg.	b deg.	km/s	arcsec	km/s	arcsec	arcsec	10^3arcsec^2		kpc	K			10^{21}cm^{-2}		$10^2 M_\odot$	
MCO_330.227-0.019	330.227	-0.019	-42.7	120	86	1.0	76	18	32	3.3	11.5	0.9	1.1	5.9	7.0	5	62
MCO_330.394-0.052	330.394	-0.052	-41.8	218	129	1.0	107	36	88	3.2	11.6	0.9	1.1	5.8	7.0	9	123
MCO_330.410+0.323	330.410	0.323	-97.0	187	76	1.5	91	26	44	6.8	8.0	1.0	1.5	9.2	18.9	49	67
MCO_330.685-0.377	330.685	-0.377	-67.6	374	280	3.3	169	90	329	4.7	10.1	1.1	1.7	12.1	33.5	104	491
MCO_330.685+0.181	330.685	0.181	-63.0	115	78	1.0	74	17	28	4.4	10.4	1.0	1.2	9.3	13.3	14	76
MCO_330.710-0.419	330.710	-0.419	-65.7	209	213	2.3	160	81	140	4.6	10.3	1.1	2.0	15.4	38.5	115	577
MCO_330.802+0.231	330.802	0.231	-45.5	343	229	1.3	170	91	246	3.4	11.4	1.0	1.5	7.6	16.1	36	395
MCO_330.827-0.510	330.827	-0.510	-64.8	152	91	1.6	106	35	43	4.5	10.3	1.3	2.3	15.8	33.3	50	259
MCO_330.894-0.377	330.894	-0.377	-64.8	71	148	2.1	112	40	33	4.5	10.3	1.3	2.3	20.6	52.4	73	381
MCO_330.894-0.477	330.894	-0.477	-66.6	134	160	2.1	137	59	68	4.6	10.2	1.1	1.9	18.1	32.7	101	494
MCO_330.902-0.352	330.902	-0.352	-57.4	75	71	1.0	61	12	17	4.1	10.7	0.9	1.2	9.7	13.8	8	58
MCO_330.910+0.156	330.910	0.156	-45.5	94	113	0.9	83	22	33	3.4	11.4	0.9	1.1	7.6	12.8	8	94
MCO_330.944-0.427	330.944	-0.427	-43.6	71	61	1.3	63	13	14	3.3	11.5	1.0	1.4	11.6	21.7	7	86
MCO_330.977-0.202	330.977	-0.202	-92.4	247	220	3.5	183	105	171	6.2	8.7	1.1	2.5	20.4	82.5	364	708
MCO_331.002+0.315	331.002	0.315	-57.4	117	178	1.6	132	55	66	4.1	10.7	1.3	2.6	17.5	45.4	71	487
MCO_331.052-0.435	331.052	-0.435	-65.7	215	192	3.2	186	109	129	4.6	10.3	1.4	3.2	29.8	95.0	298	1511
MCO_331.069+0.248	331.069	0.248	-44.6	154	258	1.1	154	75	125	3.4	11.5	1.1	1.6	9.0	18.1	34	390
MCO_331.085-0.052	331.085	-0.052	-47.3	71	92	0.0	76	18	21	3.5	11.3	1.0	1.3	6.6	8.2	7	67
MCO_331.102-0.219	331.102	-0.219	-90.6	125	156	2.2	107	36	61	6.1	8.8	1.1	1.8	16.8	29.7	98	208
MCO_331.135-0.094	331.135	-0.094	-47.3	112	86	1.1	88	24	30	3.5	11.3	0.9	1.1	7.8	13.5	10	106
MCO_331.152-0.252	331.152	-0.252	-87.8	345	137	2.2	157	77	149	5.9	9.0	1.1	1.8	15.0	47.0	175	417
MCO_331.160-0.485	331.160	-0.485	-71.2	192	154	3.9	170	91	93	4.9	10.0	1.7	3.8	51.9	151.5	493	2078
MCO_331.160+0.165	331.160	0.165	-78.6	79	128	1.1	68	14	32	5.3	9.6	0.9	1.0	6.4	12.2	11	37
MCO_331.177-0.052	331.177	-0.052	-46.4	83	81	1.1	70	15	21	3.5	11.4	0.9	1.1	7.8	13.4	6	68
MCO_331.219-0.477	331.219	-0.477	-72.2	193	205	2.8	150	71	125	4.9	10.0	1.1	1.6	12.9	44.3	98	400
MCO_331.227-0.294	331.227	-0.294	-50.1	75	118	1.8	63	13	28	3.7	11.2	1.0	1.3	9.0	20.6	7	62
MCO_331.227+0.415	331.227	0.415	-48.2	75	82	1.1	66	14	19	3.6	11.3	0.9	1.0	6.8	11.4	5	51
MCO_331.310-0.202	331.310	-0.202	-90.6	115	91	3.4	104	34	33	6.0	8.9	1.1	1.9	20.3	60.3	111	240
MCO_331.327-0.335	331.327	-0.335	-67.6	97	104	2.2	93	27	32	4.7	10.2	1.2	2.2	24.7	43.0	64	307
MCO_331.327-0.385	331.327	-0.385	-68.5	242	129	2.1	157	77	98	4.7	10.2	1.2	2.0	18.5	44.8	140	653
MCO_331.327+0.415	331.327	0.415	-47.3	50	107	1.8	70	15	17	3.6	11.4	1.0	1.2	8.7	17.7	7	76
MCO_331.344+0.131	331.344	0.131	-46.4	189	342	1.3	210	139	203	3.5	11.4	1.1	1.7	12.2	22.6	91	969

Table 3. Continued from previous page.

Clump ID	Coordinates		V _{LSR}	Δl	Δb	ΔV	R	A	A _{fwhm}	D ^N	D ^F	$\overline{T}_{\text{MB}}^{18}$	$\widehat{T}_{\text{MB}}^{18}$	$\overline{N}_{\text{H}_2}$	\widehat{N}_{H_2}	M ₁₈ ^N	M ₁₈ ^F
	<i>l</i> deg.	<i>b</i> deg.	km/s	arcsec	km/s	arcsec		10 ³ arcsec ²	kpc		K	10 ²¹ cm ⁻²	10 ²¹ cm ⁻²	10 ² M _⊙	10 ² M _⊙		
MCO_331.360+0.006	331.360	0.006	-49.2	83	80	1.1	76	18	21	3.7	11.3	1.1	1.7	13.0	22.2	14	130
MCO_331.360-0.294	331.360	-0.294	-97.0	117	148	2.0	81	21	55	6.6	8.4	1.0	1.6	9.6	15.6	37	61
MCO_331.369-0.352	331.369	-0.352	-67.6	145	225	2.6	121	46	103	4.7	10.2	1.0	1.7	13.2	26.6	58	280
MCO_331.369-0.444	331.369	-0.444	-71.2	75	138	0.8	85	23	32	4.9	10.0	1.0	1.4	7.5	13.8	18	75
MCO_331.410+0.140	331.410	0.140	-46.4	311	136	1.4	176	97	133	3.5	11.4	1.2	2.1	14.0	33.9	73	781
MCO_331.419-0.035	331.419	-0.035	-84.1	50	76	1.5	56	10	12	5.6	9.3	1.0	1.1	11.7	18.5	16	44
MCO_331.435-0.294	331.435	-0.294	-87.8	61	90	1.0	66	14	17	5.8	9.1	1.0	1.3	8.2	14.2	17	40
MCO_331.444-0.369	331.444	-0.369	-65.7	190	191	2.8	173	95	114	4.6	10.4	1.2	2.4	16.9	51.0	147	754
MCO_331.444-0.369	331.444	-0.369	-98.8	71	75	1.1	68	14	17	6.7	8.2	1.0	1.3	9.0	15.6	26	38
MCO_331.444-0.269	331.444	-0.269	-106.2	83	97	1.4	85	23	25	6.4	6.4	1.0	1.2	10.7	22.3	43	43
MCO_331.469-0.302	331.469	-0.302	-71.2	200	112	0.9	94	28	70	4.9	10.1	1.0	1.4	8.2	15.8	24	102
MCO_331.510-0.119	331.510	-0.119	-89.6	330	293	4.0	270	229	304	6.0	9.0	1.1	2.8	25.7	88.2	913	2085
MCO_331.535-0.110	331.535	-0.110	-90.6	336	184	4.8	226	161	195	6.0	8.9	1.2	2.6	26.2	96.1	670	1480
MCO_331.544-0.294	331.544	-0.294	-66.6	169	172	1.1	83	22	91	4.6	10.3	1.0	1.4	8.5	19.3	17	86
MCO_331.544-0.377	331.544	-0.377	-99.8	95	84	1.2	76	18	25	6.8	8.1	1.0	1.3	8.9	13.3	33	46
MCO_331.552-0.310	331.552	-0.310	-98.8	157	133	2.0	125	50	66	6.7	8.2	1.1	1.9	15.0	28.6	147	222
MCO_331.560-0.152	331.560	-0.152	-101.6	243	112	2.1	125	50	86	7.2	7.8	1.0	1.5	11.3	24.8	125	149
MCO_331.660+0.490	331.660	0.490	-53.8	115	48	1.4	76	18	17	3.9	11.0	1.4	2.4	16.9	38.7	21	163
MCO_331.685-0.169	331.685	-0.169	-51.9	245	89	1.5	115	41	69	3.8	11.1	1.0	1.8	11.0	30.8	29	247
MCO_331.702-0.044	331.702	-0.044	-86.9	77	107	1.7	85	23	26	5.8	9.2	1.0	1.3	9.8	22.0	32	82
MCO_331.719-0.269	331.719	-0.269	-51.0	375	97	1.7	150	71	115	3.8	11.2	1.2	2.2	11.7	29.5	52	456
MCO_331.744-0.210	331.744	-0.210	-50.1	145	65	1.9	91	26	30	3.7	11.3	1.1	1.8	13.9	28.1	22	202
MCO_331.752-0.085	331.752	-0.085	-86.9	118	101	1.2	83	22	38	5.8	9.2	0.9	1.2	7.2	12.3	22	58
MCO_331.777+0.431	331.777	0.431	-56.5	148	110	0.0	93	27	51	4.1	10.9	1.1	1.6	7.2	11.0	14	102
MCO_331.785+0.048	331.785	0.048	-48.2	274	147	1.3	163	84	127	3.6	11.4	1.1	1.8	11.2	22.7	54	530
MCO_331.794-0.010	331.794	-0.010	-54.7	198	77	1.6	104	34	48	4.0	11.0	1.1	1.6	12.2	22.2	29	222
MCO_331.802-0.144	331.802	-0.144	-51.9	164	85	1.1	104	34	44	3.8	11.2	1.0	1.6	9.4	18.9	21	176
MCO_331.877-0.127	331.877	-0.127	-52.8	137	183	2.0	158	78	79	3.9	11.1	1.3	2.3	20.9	44.5	108	886
MCO_331.885+0.048	331.885	0.048	-90.6	95	99	1.6	78	19	29	6.0	9.0	1.0	1.3	9.7	20.1	29	65
MCO_331.944-0.102	331.944	-0.102	-53.8	129	124	1.6	121	46	50	3.9	11.1	1.1	1.8	14.6	28.6	46	361
MCO_331.944-0.077	331.944	-0.077	-98.8	118	64	1.0	74	17	24	6.6	8.4	1.0	1.2	8.0	13.5	26	42
MCO_332.002-0.160	332.002	-0.160	-51.9	166	142	2.5	115	41	74	3.8	11.2	1.0	1.6	10.0	25.6	27	227
MCO_332.019-0.152	332.019	-0.152	-103.4	148	136	2.3	133	56	63	7.4	7.7	1.1	1.7	15.4	34.6	204	221
MCO_332.052-0.010	332.052	-0.010	-89.6	131	122	1.6	104	34	50	5.9	9.1	1.0	1.3	9.1	20.0	48	113
MCO_332.060+0.481	332.060	0.481	-43.6	129	82	1.5	99	31	33	3.4	11.7	1.4	2.3	18.0	42.3	27	329
MCO_332.110-0.435	332.110	-0.435	-59.3	205	121	2.5	123	48	78	4.2	10.8	1.2	2.2	20.2	48.4	76	493
MCO_332.144-0.110	332.144	-0.110	-53.8	302	278	3.4	199	124	264	3.9	11.1	1.0	1.9	10.4	31.0	88	701
MCO_332.152+0.081	332.152	0.081	-89.6	186	213	2.0	157	77	124	5.9	9.1	1.0	1.7	15.6	32.5	185	443

Table 3. Continued from previous page.

Clump ID	Coordinates		V _{LSR}	Δl	Δb	ΔV	R	A	A _{fwhm}	D ^N	D ^F	$\overline{T}_{\text{MB}}^{18}$	$\widehat{T}_{\text{MB}}^{18}$	$\overline{N_{\text{H}_2}}$	$\widehat{N_{\text{H}_2}}$	M ₁₈ ^N	M ₁₈ ^F
	<i>l</i> deg.	<i>b</i> deg.	km/s	arcsec	km/s	arcsec	10 ³ arcsec ²	10 ³ arcsec ²	kpc	K	K	10 ²¹ cm ⁻²	10 ²¹ cm ⁻²	10 ²¹ cm ⁻²	10 ² M _⊙		
MCO_332.185+0.115	332.185	0.115	-51.0	176	265	1.2	131	54	147	3.8	11.3	1.0	1.6	7.7	15.9	26	232
MCO_332.327-0.127	332.327	-0.127	-51.9	310	223	2.1	201	127	217	3.8	11.2	1.1	1.8	13.0	38.3	107	914
MCO_332.327+0.490	332.327	0.490	-65.7	154	76	1.1	85	23	37	4.6	10.5	1.1	1.7	10.1	21.4	21	110
MCO_332.327-0.385	332.327	-0.385	-51.9	68	91	1.5	58	11	20	3.8	11.2	0.9	1.2	8.3	16.5	6	49
MCO_332.360-0.444	332.360	-0.444	-50.1	138	143	2.2	131	54	62	3.7	11.3	1.5	2.9	18.7	45.0	62	568
MCO_332.394-0.094	332.394	-0.094	-50.1	166	132	1.7	135	58	69	3.7	11.3	1.3	2.3	16.0	36.1	56	518
MCO_332.394+0.106	332.394	0.106	-49.2	484	361	2.1	264	219	549	3.7	11.4	1.0	1.8	8.7	18.6	114	1086
MCO_332.427-0.510	332.427	-0.510	-56.5	122	88	1.4	90	25	34	4.1	11.0	1.2	2.2	14.9	27.9	28	198
MCO_332.477-0.144	332.477	-0.144	-51.9	178	174	2.0	142	63	98	3.8	11.2	1.1	1.9	13.9	27.6	57	486
MCO_332.510+0.323	332.510	0.323	-48.2	188	92	0.4	74	17	54	3.6	11.4	0.9	1.0	5.9	10.9	6	58
MCO_332.519-0.169	332.519	-0.169	-53.8	86	88	2.0	81	21	24	3.9	11.1	1.2	1.8	15.2	29.5	22	172
MCO_332.552-0.127	332.552	-0.127	-49.2	187	138	2.0	136	59	81	3.7	11.4	1.2	2.2	16.5	40.3	58	551
MCO_332.610+0.023	332.610	0.023	-97.0	68	61	1.0	61	12	13	6.4	8.7	1.0	1.2	9.1	14.0	19	36
MCO_332.627+0.290	332.627	0.290	-48.2	81	57	1.0	61	12	15	3.6	11.5	1.1	1.5	10.5	15.9	7	71
MCO_332.652-0.202	332.652	-0.202	-47.3	235	116	2.1	122	47	85	3.6	11.5	1.1	2.1	12.5	30.2	33	340
MCO_332.669+0.265	332.669	0.265	-51.9	64	115	1.9	61	12	23	3.8	11.3	0.9	1.2	7.3	12.9	6	48
MCO_332.702+0.173	332.702	0.173	-52.8	130	190	2.2	122	47	78	3.9	11.2	1.0	1.5	9.7	21.9	30	251
MCO_332.769-0.477	332.769	-0.477	-55.6	136	144	1.7	108	37	61	4.0	11.1	1.1	2.1	13.5	31.5	36	268
MCO_332.769+0.048	332.769	0.048	-72.2	112	102	1.3	85	23	36	4.9	10.2	0.9	1.2	8.3	13.4	20	86
MCO_332.794-0.019	332.794	-0.019	-97.0	201	262	3.3	212	141	166	6.3	8.8	1.1	2.2	16.5	44.5	413	790
MCO_332.794-0.235	332.794	-0.235	-45.5	88	72	1.4	72	16	20	3.5	11.6	1.2	1.7	14.7	29.6	13	141
MCO_332.927-0.269	332.927	-0.269	-61.1	198	57	1.0	88	24	35	4.3	10.8	1.0	1.3	7.6	13.3	15	95
MCO_332.935-0.010	332.935	-0.010	-50.1	109	66	1.5	74	17	23	3.8	11.4	0.9	1.1	8.4	18.0	9	81
MCO_332.944-0.027	332.944	-0.027	-71.2	149	131	1.7	90	25	61	4.9	10.3	0.9	1.2	8.9	18.2	23	104
MCO_332.969-0.302	332.969	-0.302	-52.8	183	292	2.4	168	89	168	3.9	11.2	1.1	1.7	11.8	29.8	70	584
MCO_332.969-0.052	332.969	-0.052	-50.1	138	100	1.6	90	25	44	3.8	11.4	1.0	1.5	11.4	23.8	18	164
MCO_333.010-0.444	333.010	-0.444	-57.4	113	118	1.7	100	32	42	4.2	11.0	1.2	1.7	14.3	29.6	34	239
MCO_333.019-0.510	333.019	-0.510	-62.0	189	70	2.5	107	36	42	4.4	10.8	1.1	1.9	15.5	33.0	47	283
MCO_333.019-0.444	333.019	-0.444	-54.7	100	135	2.5	111	39	42	4.0	11.1	1.2	1.8	19.8	43.2	54	419
MCO_333.027-0.494	333.027	-0.494	-55.6	153	109	3.5	123	48	52	4.1	11.1	1.4	2.7	44.3	80.6	153	1142
MCO_333.027-0.144	333.027	-0.144	-43.6	100	126	0.1	76	18	40	3.4	11.8	0.9	1.2	5.9	7.5	5	65
MCO_333.044-0.419	333.044	-0.419	-52.8	189	161	3.6	151	72	96	3.9	11.2	1.1	1.7	18.8	61.6	91	753
MCO_333.052-0.077	333.052	-0.077	-43.6	58	146	0.9	78	19	27	3.4	11.8	1.0	1.4	8.3	15.1	8	95
MCO_333.077-0.469	333.077	-0.469	-55.6	145	209	3.9	166	86	95	4.1	11.1	1.8	4.4	69.5	161.1	434	3252
MCO_333.085+0.015	333.085	0.015	-46.4	79	95	0.9	74	17	24	3.5	11.6	1.0	1.2	7.8	14.5	7	79
MCO_333.127-0.510	333.127	-0.510	-57.4	248	150	5.7	163	84	117	4.2	11.0	1.1	2.5	19.5	70.2	124	870
MCO_333.135-0.427	333.135	-0.427	-52.8	244	217	4.1	228	163	166	3.9	11.3	1.6	4.7	53.4	235.1	584	4843
MCO_333.160-0.102	333.160	-0.102	-90.6	351	395	2.5	275	238	436	5.9	9.3	1.0	1.7	13.5	36.2	491	1213

Table 3. Continued from previous page.

Clump ID	Coordinates		V _{LSR}	Δl	Δb	ΔV	R	A	A _{fwhm}	D ^N	D ^F	$\overline{T}_{\text{MB}}^{18}$	$\widehat{T}_{\text{MB}}^{18}$	$\overline{N}_{\text{H}_2}$	\widehat{N}_{H_2}	M ₁₈ ^N	M ₁₈ ^F
	<i>l</i> deg.	<i>b</i> deg.	km/s	arcsec	km/s	arcsec		10 ³ arcsec ²		kpc	K			10 ²¹ cm ⁻²	10 ² M _⊙		
MCO_333.160+0.448	333.160	0.448	-63.0	77	109	1.1	83	22	27	4.4	10.7	1.0	1.2	10.7	14.8	20	117
MCO_333.177-0.094	333.177	-0.094	-47.3	150	115	2.0	117	43	54	3.6	11.6	1.0	1.5	13.6	29.9	33	344
MCO_333.185-0.002	333.185	-0.002	-48.2	199	134	1.4	128	51	84	3.7	11.5	1.0	1.4	8.3	18.7	25	248
MCO_333.219-0.377	333.219	-0.377	-51.0	249	267	4.8	172	94	209	3.8	11.4	1.1	1.9	14.8	44.0	88	786
MCO_333.219-0.327	333.219	-0.327	-60.2	94	99	1.4	90	25	29	4.3	10.9	1.2	1.7	13.9	27.4	28	181
MCO_333.219-0.135	333.219	-0.135	-47.3	124	85	1.7	88	24	33	3.6	11.6	1.0	1.4	11.8	19.9	16	168
MCO_333.219+0.356	333.219	0.356	-62.0	58	148	1.0	81	21	27	4.4	10.8	1.0	1.3	7.2	19.4	13	76
MCO_333.227+0.240	333.227	0.240	-50.1	137	196	1.2	139	61	84	3.8	11.4	1.2	1.9	12.4	24.4	47	434
MCO_333.244+0.206	333.244	0.206	-50.1	177	143	1.4	135	58	80	3.8	11.4	1.2	2.2	15.0	32.9	54	496
MCO_333.244+0.440	333.244	0.440	-63.9	113	191	1.7	115	41	68	4.5	10.7	1.0	1.4	9.0	17.7	33	186
MCO_333.269-0.044	333.269	-0.044	-70.3	141	212	1.8	145	67	94	4.8	10.4	1.0	1.2	9.4	22.7	64	296
MCO_333.294+0.090	333.294	0.090	-51.0	289	308	2.1	206	133	279	3.8	11.4	1.1	1.9	13.1	31.9	111	991
MCO_333.302-0.510	333.302	-0.510	-58.4	259	131	3.5	168	88	107	4.2	11.0	1.2	2.0	25.9	55.5	178	1208
MCO_333.310-0.402	333.310	-0.402	-53.8	173	124	4.7	156	77	68	4.0	11.2	1.8	4.5	67.1	199.5	354	2843
MCO_333.310-0.435	333.310	-0.435	-51.9	253	139	4.2	170	91	111	3.9	11.3	1.2	2.8	24.4	67.0	146	1250
MCO_333.310-0.027	333.310	-0.027	-48.2	88	77	1.5	76	18	21	3.7	11.5	1.0	1.2	10.7	19.1	11	113
MCO_333.319+0.206	333.319	0.206	-45.5	141	68	1.0	88	24	30	3.5	11.7	1.1	2.0	9.9	26.6	13	144
MCO_333.319-0.094	333.319	-0.094	-89.6	103	100	1.0	88	24	32	5.8	9.4	0.9	1.1	7.0	12.2	25	65
MCO_333.335-0.369	333.335	-0.369	-52.8	228	165	4.3	201	127	118	3.9	11.3	1.9	4.8	65.9	198.1	563	4675
MCO_333.335-0.260	333.335	-0.260	-51.0	132	163	2.0	93	27	68	3.8	11.4	1.0	1.4	10.8	23.1	19	166
MCO_333.344-0.452	333.344	-0.452	-55.6	248	186	4.9	187	110	145	4.1	11.1	1.1	1.7	16.8	41.4	134	1003
MCO_333.369-0.477	333.369	-0.477	-47.3	85	116	0.5	85	23	31	3.6	11.6	1.2	1.9	8.5	13.0	11	112
MCO_333.385-0.335	333.385	-0.335	-49.2	232	191	3.9	194	119	139	3.7	11.5	1.1	1.9	24.8	71.3	179	1707
MCO_333.394-0.135	333.394	-0.135	-47.3	206	88	1.0	96	29	57	3.6	11.6	0.9	1.1	7.2	13.5	12	122
MCO_333.402-0.219	333.402	-0.219	-62.0	90	65	1.4	70	15	18	4.4	10.8	1.1	1.7	13.3	25.3	17	104
MCO_333.427+0.423	333.427	0.423	-64.8	172	107	1.2	99	31	58	4.5	10.7	1.0	1.4	8.6	17.4	24	131
MCO_333.485-0.185	333.485	-0.185	-45.5	194	180	4.7	150	71	110	3.5	11.7	1.3	2.8	33.2	90.1	128	1419
MCO_333.485-0.494	333.485	-0.494	-56.5	267	181	2.7	183	105	152	4.1	11.1	1.1	2.1	15.7	40.3	123	894
MCO_333.485+0.123	333.485	0.123	-105.3	181	220	0.7	136	59	125	7.0	8.2	1.1	1.7	8.3	13.7	103	145
MCO_333.502-0.144	333.502	-0.144	-46.4	148	132	4.1	136	59	61	3.6	11.7	1.2	1.9	23.6	67.6	77	822
MCO_333.510-0.252	333.510	-0.252	-51.9	147	133	2.6	133	56	62	3.9	11.3	1.6	3.4	35.2	87.8	129	1109
MCO_333.527-0.119	333.527	-0.119	-50.1	145	168	3.7	137	59	77	3.8	11.4	1.0	1.9	14.6	36.6	54	500
MCO_333.527-0.177	333.527	-0.177	-50.1	137	139	2.2	122	47	60	3.8	11.4	1.0	1.6	15.6	31.7	46	420
MCO_333.535-0.277	333.535	-0.277	-51.0	150	198	2.9	158	78	93	3.8	11.4	1.6	3.8	39.0	99.8	196	1743
MCO_333.569-0.052	333.569	-0.052	-48.2	212	405	7.6	230	167	270	3.7	11.6	1.1	2.2	15.8	50.4	155	1538
MCO_333.585-0.310	333.585	-0.310	-48.2	306	178	4.0	172	94	172	3.7	11.6	1.2	3.1	18.2	63.8	101	998
MCO_333.594-0.169	333.594	-0.169	-47.3	122	157	3.0	134	57	60	3.6	11.6	1.1	2.0	21.3	43.8	69	716
MCO_333.594-0.077	333.594	-0.077	-43.6	182	225	2.5	169	90	129	3.4	11.8	1.1	1.8	15.5	40.9	71	854

Table 3. Continued from previous page.

Clump ID	Coordinates		V _{LSR}	Δl	Δb	ΔV	R	A	A _{fwhm}	D ^N	D ^F	$\overline{T}_{\text{MB}}^{18}$	$\widehat{T}_{\text{MB}}^{18}$	$\overline{N_{\text{H}_2}}$	$\widehat{N_{\text{H}_2}}$	M_{18}^N	M_{18}^F
	<i>l</i> deg.	<i>b</i> deg.	km/s	arcsec	km/s	arcsec	10 ³ arcsec ²	10 ³ arcsec ²	kpc	K	1.2	2.7	27.4	79.4	150	1435	
MCO_333.602-0.219	333.602	-0.219	-49.2	208	160	3.5	169	90	105	3.7	11.5	1.2	2.7	27.4	79.4	150	1435
MCO_333.627+0.023	333.627	0.023	-85.0	172	193	2.8	162	83	105	5.6	9.7	1.1	2.0	16.4	55.4	186	557
MCO_333.660-0.144	333.660	-0.144	-50.1	160	236	2.3	185	108	119	3.8	11.5	1.2	2.3	21.8	46.0	147	1357
MCO_333.660+0.365	333.660	0.365	-37.2	139	94	0.7	99	31	41	3.0	12.2	1.2	1.8	9.4	15.3	12	188
MCO_333.660-0.135	333.660	-0.135	-89.6	143	106	1.1	96	29	48	5.8	9.4	1.0	1.2	8.0	14.8	34	90
MCO_333.669+0.031	333.669	0.031	-86.9	98	71	3.8	90	25	22	5.7	9.6	1.1	1.8	21.7	54.1	77	220
MCO_333.677-0.027	333.677	-0.027	-51.9	71	142	1.8	90	25	31	3.9	11.4	0.9	1.1	7.9	19.3	13	113
MCO_333.685+0.356	333.685	0.356	-37.2	66	132	1.4	86	23	27	3.0	12.2	1.2	1.8	12.9	25.1	12	198
MCO_333.719+0.348	333.719	0.348	-36.3	120	120	1.7	112	40	45	3.0	12.3	1.4	2.5	21.1	44.7	32	553
MCO_333.744-0.227	333.744	-0.227	-48.2	565	153	3.9	262	215	271	3.7	11.6	1.4	3.4	29.8	104.4	379	3764
MCO_333.752-0.310	333.752	-0.310	-51.0	752	294	5.2	358	404	695	3.8	11.4	1.1	2.0	17.8	53.3	462	4114
MCO_333.777-0.094	333.777	-0.094	-89.6	189	119	1.7	103	33	71	5.8	9.4	1.0	1.3	8.9	19.5	44	116
MCO_333.785+0.323	333.785	0.323	-35.4	178	189	1.3	169	90	106	2.9	12.3	1.4	2.7	17.0	41.9	57	1022
MCO_333.819-0.152	333.819	-0.152	-97.0	152	178	2.9	129	52	85	6.2	9.0	1.0	1.2	9.2	20.2	82	171
MCO_333.902-0.002	333.902	-0.002	-89.6	53	136	1.1	68	14	23	5.8	9.5	1.0	1.1	6.1	7.3	13	35
MCO_333.910+0.031	333.910	0.031	-87.8	90	87	0.9	68	14	25	5.7	9.6	0.9	1.1	6.6	12.6	14	38
MCO_333.969+0.156	333.969	0.156	-49.2	95	100	0.9	81	21	30	3.7	11.5	1.1	1.4	8.9	15.3	11	108
MCO_333.977+0.056	333.977	0.056	-50.1	226	124	1.1	123	48	88	3.8	11.5	1.0	1.2	6.9	13.2	21	191
MCO_334.027+0.323	334.027	0.323	-63.9	201	150	1.4	132	55	95	4.5	10.8	1.0	1.6	8.5	15.8	42	239
MCO_334.035-0.144	334.035	-0.144	-89.6	107	82	1.0	70	15	28	5.8	9.5	1.0	1.2	8.2	13.8	19	49
MCO_334.044-0.052	334.044	-0.052	-86.9	83	52	1.7	56	10	14	5.7	9.6	0.9	1.0	10.6	18.0	15	43
MCO_334.060+0.340	334.060	0.340	-59.3	100	108	1.8	97	30	34	4.3	11.0	1.1	1.9	12.7	27.0	30	202
MCO_334.060+0.023	334.060	0.023	-87.8	241	249	2.9	171	92	188	5.7	9.6	1.0	1.4	8.9	20.9	117	327
MCO_334.060+0.256	334.060	0.256	-84.1	188	148	0.4	86	23	87	5.5	9.8	1.0	1.1	6.2	7.1	20	61
MCO_334.077+0.223	334.077	0.223	-51.0	122	78	0.9	78	19	30	3.8	11.5	1.0	1.3	8.2	14.3	10	89
MCO_334.110-0.319	334.110	-0.319	-49.2	202	127	1.4	128	51	80	3.7	11.6	0.9	1.1	9.0	14.4	28	270
MCO_334.119+0.398	334.119	0.398	-61.1	230	162	2.4	158	78	117	4.4	10.9	1.1	1.8	15.7	33.3	103	646
MCO_334.127+0.315	334.127	0.315	-63.0	115	99	1.4	103	33	36	4.5	10.8	1.1	1.8	11.1	21.6	32	190
MCO_334.127-0.177	334.127	-0.177	-88.7	164	53	0.0	76	18	27	5.8	9.5	0.9	1.1	5.9	7.0	16	43
MCO_334.144+0.231	334.144	0.231	-63.0	149	149	1.2	139	61	70	4.5	10.8	1.2	2.1	10.9	28.0	59	345
MCO_334.144+0.356	334.144	0.356	-61.1	281	166	3.1	176	97	147	4.4	10.9	1.1	1.8	19.2	44.2	157	979
MCO_334.185+0.048	334.185	0.048	-42.7	135	124	1.6	129	52	53	3.4	11.9	1.3	2.6	17.3	46.8	45	565
MCO_334.219-0.210	334.219	-0.210	-50.1	341	182	2.0	202	129	196	3.8	11.5	1.1	1.8	13.1	31.9	107	983
MCO_334.252-0.127	334.252	-0.127	-87.8	114	99	0.3	93	27	35	5.7	9.6	1.1	1.4	7.2	13.5	28	78
MCO_334.302-0.302	334.302	-0.302	-49.2	92	130	4.4	90	25	37	3.7	11.6	1.0	1.3	10.5	19.3	16	156
MCO_334.327-0.135	334.327	-0.135	-87.8	147	85	1.2	103	33	39	5.7	9.6	1.0	1.5	9.1	21.6	43	123
MCO_334.344-0.369	334.344	-0.369	-87.8	85	91	1.4	72	16	24	5.7	9.6	0.9	1.0	6.7	12.0	16	44
MCO_334.394+0.048	334.394	0.048	-92.4	117	67	1.1	74	17	25	5.9	9.4	1.0	1.5	9.1	16.0	24	60

Table 3. Continued from previous page.

Clump ID	Coordinates		V _{LSR}	Δl	Δb	ΔV	R	A	A _{fwhm}	D ^N	D ^F	$\overline{T}_{\text{MB}}^{18}$	$\widehat{T}_{\text{MB}}^{18}$	$\overline{N}_{\text{H}_2}$	\widehat{N}_{H_2}	M ₁₈ ^N	M ₁₈ ^F
	<i>l</i> deg.	<i>b</i> deg.	km/s	arcsec	km/s	arcsec	10 ³ arcsec ²		10 ³ arcsec ²	kpc	K	10 ²¹ cm ⁻²	10 ²¹ cm ⁻²	10 ²¹ cm ⁻²	10 ² M _⊙		
MCO_334.452-0.252	334.452	-0.252	-42.7	292	210	3.1	218	149	193	3.4	12.0	1.0	1.7	15.0	47.4	113	1404
MCO_334.510+0.006	334.510	0.006	-109.0	136	54	1.1	78	19	23	7.1	8.2	1.0	1.2	7.8	14.4	33	44
MCO_334.535+0.098	334.535	0.098	-48.2	159	124	0.7	86	23	62	3.7	11.6	1.0	1.3	6.2	8.8	9	86
MCO_334.627-0.285	334.627	-0.285	-47.3	144	135	1.5	120	45	61	3.7	11.7	1.1	1.6	13.2	24.9	35	359
MCO_334.660+0.431	334.660	0.431	-67.6	188	410	1.7	226	161	242	4.7	10.7	1.2	2.4	14.9	45.1	234	1196
MCO_334.669+0.023	334.669	0.023	-33.5	202	134	0.9	148	68	85	2.8	12.5	1.2	2.0	9.9	20.7	24	468
MCO_334.710+0.023	334.710	0.023	-86.9	75	118	1.0	68	14	28	5.7	9.7	0.9	1.1	7.7	12.4	16	46
MCO_334.760+0.490	334.760	0.490	-64.8	166	187	1.6	141	62	97	4.6	10.8	1.0	1.5	10.8	22.0	61	342
MCO_334.810-0.135	334.810	-0.135	-47.3	261	76	1.1	107	36	63	3.7	11.7	0.9	1.2	7.5	13.3	16	163
MCO_334.985+0.431	334.985	0.431	-63.9	158	87	1.2	88	24	43	4.5	10.9	0.9	1.2	7.8	13.4	17	99
MCO_335.010-0.052	335.010	-0.052	-95.2	81	90	1.1	78	19	23	6.1	9.3	1.0	1.3	10.0	15.9	30	72
MCO_335.069-0.444	335.069	-0.444	-40.9	153	175	1.6	130	53	84	3.3	12.1	1.1	1.7	13.4	31.9	34	459
MCO_335.102+0.415	335.102	0.415	-62.0	237	125	1.3	134	57	93	4.4	11.0	1.1	1.7	10.4	23.5	51	313
MCO_335.127-0.469	335.127	-0.469	-40.9	112	108	1.5	107	36	38	3.3	12.1	1.4	2.9	20.9	39.9	36	485
MCO_335.135-0.419	335.135	-0.419	-40.0	214	123	0.9	124	49	83	3.3	12.2	1.1	1.7	8.7	17.3	20	274
MCO_335.152+0.148	335.152	0.148	-63.9	93	109	1.1	90	25	32	4.5	10.9	1.0	1.3	8.3	15.0	19	109
MCO_335.177-0.260	335.177	-0.260	-47.3	270	181	1.8	163	84	154	3.7	11.8	1.0	1.7	11.3	24.5	56	575
MCO_335.202-0.094	335.202	-0.094	-46.4	335	453	3.8	242	185	476	3.6	11.8	1.0	1.7	9.3	31.1	99	1050
MCO_335.235-0.369	335.235	-0.369	-40.9	158	186	1.8	156	77	92	3.3	12.1	1.1	2.0	11.7	25.5	43	579
MCO_335.302+0.415	335.302	0.415	-63.0	380	111	2.1	155	76	133	4.5	10.9	1.1	1.6	10.9	26.6	74	435
MCO_335.310-0.369	335.310	-0.369	-40.9	91	127	0.8	76	18	36	3.3	12.1	0.9	1.0	5.9	10.8	5	68
MCO_335.444-0.244	335.444	-0.244	-45.5	152	119	1.7	125	50	57	3.6	11.9	1.1	1.9	14.6	36.6	41	448
MCO_335.444+0.123	335.444	0.123	-41.8	87	158	1.0	103	33	43	3.4	12.1	1.1	1.4	7.8	15.2	13	167
MCO_335.460-0.252	335.460	-0.252	-43.6	201	95	2.1	125	50	60	3.5	12.0	1.1	1.8	15.6	40.3	41	486
MCO_335.585-0.219	335.585	-0.219	-45.5	227	131	0.5	136	59	93	3.6	11.9	1.2	1.7	8.4	16.2	28	304
MCO_335.602+0.181	335.602	0.181	-51.0	89	150	1.4	102	32	42	3.9	11.6	1.1	1.6	11.6	20.6	25	221
MCO_335.602-0.310	335.602	-0.310	-48.2	78	170	1.5	97	30	42	3.7	11.7	1.0	1.2	9.8	21.6	18	176
MCO_335.660-0.194	335.660	-0.194	-45.5	106	151	0.1	97	30	50	3.6	11.9	1.0	1.2	6.6	8.1	11	123
MCO_335.702+0.190	335.702	0.190	-51.9	163	87	1.4	106	35	45	4.0	11.5	1.2	2.2	13.8	29.4	33	283
MCO_335.744+0.040	335.744	0.040	-48.2	129	141	0.7	113	41	57	3.8	11.7	1.1	1.5	7.5	12.8	19	183
MCO_335.760-0.369	335.760	-0.369	-40.9	337	117	1.3	148	69	124	3.3	12.2	1.0	1.3	8.9	19.7	30	401
MCO_335.769-0.102	335.769	-0.102	-46.4	193	177	1.0	120	45	107	3.7	11.8	1.0	1.2	7.0	13.6	19	195
MCO_335.810+0.156	335.810	0.156	-51.9	182	145	2.0	148	69	83	4.0	11.6	1.2	2.4	14.2	41.8	68	578
MCO_335.827-0.110	335.827	-0.110	-46.4	98	196	0.5	107	36	60	3.7	11.9	1.0	1.2	6.5	11.0	14	144
MCO_336.119-0.069	336.119	-0.069	-106.2	73	128	1.4	90	25	29	6.6	8.9	1.1	1.5	10.1	21.6	49	89
MCO_336.127+0.248	336.127	0.248	-36.3	139	183	1.6	127	50	80	3.1	12.5	1.0	1.5	7.8	17.3	16	268
MCO_336.144-0.094	336.144	-0.094	-42.7	100	115	0.8	85	23	36	3.5	12.1	1.0	1.2	6.7	13.9	8	97
MCO_336.194+0.006	336.194	0.006	-40.0	80	64	0.9	68	14	16	3.3	12.3	1.0	1.3	8.7	14.6	6	83

Table 3. Continued from previous page.

Clump ID	Coordinates		V _{LSR}	Δl	Δb	ΔV	R	A	A _{fwhm}	D ^N	D ^F	$\overline{T}_{\text{MB}}^{18}$	$\widehat{T}_{\text{MB}}^{18}$	$\overline{N_{\text{H}_2}}$	$\widehat{N_{\text{H}_2}}$	M ₁₈ ^N	M ₁₈ ^F
	<i>l</i> deg.	<i>b</i> deg.	km/s	arcsec	km/s	arcsec	arcsec	10 ³ arcsec ²		kpc	K			10 ²¹ cm ⁻²	10 ² M _⊙		
MCO_336.202+0.190	336.202	0.190	-46.4	149	146	1.4	135	58	68	3.7	11.9	1.3	2.5	13.7	38.8	47	488
MCO_336.252+0.190	336.252	0.190	-48.2	100	107	1.7	96	29	34	3.8	11.8	1.2	1.8	16.5	33.9	30	289
MCO_336.277-0.019	336.277	-0.019	-42.7	433	160	1.2	153	74	218	3.5	12.1	1.1	2.0	8.0	16.2	31	380
MCO_336.277+0.406	336.277	0.406	-113.6	115	96	0.0	68	14	35	7.2	8.4	1.0	1.2	6.2	7.9	20	28
MCO_336.285+0.181	336.285	0.181	-47.3	93	121	1.8	100	32	35	3.7	11.8	1.2	1.8	15.9	36.2	31	308
MCO_336.327+0.181	336.327	0.181	-48.2	106	123	1.5	94	28	41	3.8	11.8	1.1	1.6	14.9	23.6	26	254
MCO_336.369+0.190	336.369	0.190	-48.2	103	178	1.3	120	45	57	3.8	11.8	1.2	1.7	11.3	24.6	32	310
MCO_336.369-0.035	336.369	-0.035	-128.3	129	130	3.3	121	46	53	6.7	6.7	1.0	1.5	13.3	38.5	119	119
MCO_336.410+0.198	336.410	0.198	-48.2	111	115	1.7	107	36	40	3.8	11.8	1.1	1.7	15.3	33.1	35	336
MCO_336.419-0.269	336.419	-0.269	-89.6	107	81	1.1	68	14	27	5.8	9.8	0.9	1.0	6.4	12.3	13	39
MCO_336.485+0.048	336.485	0.048	-131.0	84	91	1.8	79	20	24	6.8	6.8	1.0	1.3	10.2	20.9	41	41
MCO_336.502+0.131	336.502	0.131	-41.8	129	75	0.4	79	20	30	3.4	12.2	1.0	1.3	6.8	11.7	7	88
MCO_336.594+0.098	336.594	0.098	-41.8	50	109	0.4	70	15	17	3.4	12.2	1.2	1.9	8.7	15.4	7	86
MCO_336.619+0.165	336.619	0.165	-103.4	61	118	1.5	70	15	23	6.4	9.2	1.0	1.2	9.8	18.1	27	55
MCO_336.710+0.231	336.710	0.231	-74.9	72	103	1.4	79	20	23	5.1	10.5	1.0	1.4	10.6	20.3	24	102
MCO_336.752-0.235	336.752	-0.235	-98.8	76	54	1.5	61	12	13	6.2	9.4	1.0	1.3	11.8	20.5	23	54
MCO_336.827+0.015	336.827	0.015	-115.4	70	73	1.5	68	14	16	7.2	8.4	1.1	1.8	15.7	28.7	52	70
MCO_336.827+0.123	336.827	0.123	-83.2	94	87	3.0	93	27	26	5.5	10.1	1.0	1.7	20.2	45.6	72	247
MCO_336.835-0.210	336.835	-0.210	-78.6	109	90	1.3	83	22	31	5.3	10.4	1.0	1.3	9.8	20.0	26	100
MCO_336.852+0.265	336.852	0.265	-100.7	85	52	1.4	58	11	14	6.3	9.3	0.9	1.2	8.7	13.2	16	36
MCO_336.869+0.281	336.869	0.281	-69.4	64	65	1.5	66	14	13	4.9	10.8	1.1	1.5	13.1	23.4	18	90
MCO_336.877-0.202	336.877	-0.202	-83.2	163	100	2.5	116	42	51	5.5	10.2	1.2	2.1	17.7	51.4	99	340
MCO_336.877-0.019	336.877	-0.019	-74.9	203	134	2.8	103	33	86	5.1	10.5	1.1	1.7	16.7	34.6	64	271
MCO_336.885-0.027	336.885	-0.027	-77.7	89	126	3.2	108	37	35	5.2	10.4	1.1	1.9	21.5	56.3	95	377
MCO_336.910-0.044	336.910	-0.044	-122.8	103	86	2.2	94	28	28	7.0	7.0	1.1	1.7	16.8	40.5	101	101
MCO_336.910-0.177	336.910	-0.177	-74.0	211	105	2.5	120	45	70	5.1	10.6	1.0	1.5	13.0	30.8	66	287
MCO_336.910+0.098	336.910	0.098	-81.4	72	124	1.1	76	18	28	5.4	10.2	0.9	1.1	8.7	12.7	20	72
MCO_336.927-0.202	336.927	-0.202	-81.4	97	63	0.8	66	14	19	5.4	10.2	1.1	1.7	7.8	11.5	13	49
MCO_336.952-0.252	336.952	-0.252	-73.1	223	183	2.7	88	24	128	5.0	10.6	0.9	1.2	6.9	13.1	19	83
MCO_336.985+0.431	336.985	0.431	-54.7	166	151	1.6	136	59	79	4.2	11.5	1.4	3.3	14.4	38.9	64	488
MCO_336.985-0.035	336.985	-0.035	-122.8	171	196	2.8	175	96	105	7.7	7.7	1.2	2.0	19.4	59.0	487	487
MCO_336.994-0.144	336.994	-0.144	-118.2	72	84	1.4	68	14	19	7.5	8.1	0.9	1.1	7.5	17.8	27	31
MCO_337.002+0.106	337.002	0.106	-79.5	258	102	2.9	145	67	83	5.3	10.3	1.0	1.5	14.0	34.8	116	437
MCO_337.044-0.085	337.044	-0.085	-119.1	522	148	4.9	211	140	243	7.8	7.8	1.0	1.7	14.2	35.7	530	530
MCO_337.119-0.019	337.119	-0.019	-116.3	164	137	2.3	148	68	71	7.3	8.4	1.2	2.0	18.7	51.5	295	397
MCO_337.135-0.152	337.135	-0.152	-76.8	95	192	2.6	116	42	57	5.2	10.5	1.0	1.6	19.8	42.9	99	402
MCO_337.152-0.410	337.152	-0.410	-43.6	235	109	1.8	147	68	81	3.6	12.1	1.1	1.6	12.9	28.6	49	559
MCO_337.177-0.060	337.177	-0.060	-67.6	190	278	4.8	199	124	166	4.8	10.9	1.1	2.0	20.9	72.4	261	1348

Table 3. Continued from previous page.

Clump ID	Coordinates		V _{LSR} km/s	Δl arcsec	Δb arcsec	ΔV km/s	R arcsec	A 10^3arcsec^2	A _{fwhm} 10^3arcsec^2	D ^N kpc	D ^F	$\overline{T}_{\text{MB}}^{18}$ K	$\widehat{T}_{\text{MB}}^{18}$ K	$\overline{N}_{\text{H}_2}$ 10^{21}cm^{-2}	\widehat{N}_{H_2} 10^{21}cm^{-2}	M ₁₈ ^N $10^2 M_{\odot}$	M ₁₈ ^F
	<i>l</i> deg.	<i>b</i> deg.															
MCO_337.177-0.177	337.177	-0.177	-120.9	129	115	1.9	97	30	47	7.8	7.8	1.1	1.6	15.7	29.1	124	124
MCO_337.185+0.106	337.185	0.106	-65.7	124	53	1.8	72	16	21	4.7	11.0	0.9	1.1	7.9	13.8	12	68
MCO_337.194-0.010	337.194	-0.010	-76.8	106	95	1.7	93	27	31	5.2	10.5	1.0	1.4	11.7	24.1	37	152
MCO_337.269+0.390	337.269	0.390	-45.5	107	162	1.1	110	38	55	3.7	12.0	1.1	1.6	9.4	20.6	21	225
MCO_337.277-0.244	337.277	-0.244	-89.6	79	105	0.7	76	18	26	5.8	9.9	1.0	1.3	7.0	13.5	18	54
MCO_337.285-0.177	337.285	-0.177	-53.8	166	144	2.5	106	35	75	4.1	11.6	1.0	1.5	12.1	31.3	32	250
MCO_337.285-0.010	337.285	-0.010	-109.0	134	65	1.8	83	22	27	6.7	9.0	1.0	1.3	10.7	26.9	46	82
MCO_337.294+0.081	337.294	0.081	-109.9	129	179	3.4	135	58	72	6.8	8.9	1.0	1.5	11.1	28.2	128	224
MCO_337.319-0.385	337.319	-0.385	-56.5	119	231	1.3	139	60	87	4.3	11.4	1.2	2.5	12.2	34.2	59	423
MCO_337.344-0.152	337.344	-0.152	-73.1	463	194	6.8	197	122	282	5.0	10.6	0.9	1.2	12.8	30.8	173	772
MCO_337.419-0.410	337.419	-0.410	-43.6	418	131	2.0	222	155	172	3.6	12.1	1.2	2.5	14.7	70.4	129	1471
MCO_337.419-0.310	337.419	-0.310	-44.6	66	117	1.1	74	17	24	3.6	12.1	1.0	1.3	7.4	14.0	7	81
MCO_337.427+0.073	337.427	0.073	-62.0	56	74	1.5	61	12	13	4.5	11.2	1.0	1.3	11.8	20.4	12	75
MCO_337.427-0.260	337.427	-0.260	-43.6	148	80	1.1	97	30	37	3.6	12.1	0.9	1.2	8.0	13.4	13	153
MCO_337.469-0.244	337.469	-0.244	-62.0	128	154	0.9	66	14	62	4.5	11.2	0.9	0.9	6.2	11.2	8	46
MCO_337.510-0.302	337.510	-0.302	-54.7	254	149	3.5	97	30	119	4.2	11.5	1.1	1.9	8.9	20.1	20	155
MCO_337.519+0.173	337.519	0.173	-91.5	61	155	2.7	83	22	30	5.8	9.9	0.9	1.1	9.4	19.1	31	87
MCO_337.519-0.127	337.519	-0.127	-79.5	80	73	1.5	63	13	18	5.3	10.4	0.9	1.1	7.1	12.7	11	42
MCO_337.527-0.210	337.527	-0.210	-56.5	193	389	1.7	197	122	236	4.3	11.4	1.2	2.9	15.0	39.1	146	1047
MCO_337.527-0.244	337.527	-0.244	-54.7	189	84	2.4	103	33	50	4.2	11.5	1.2	2.2	13.7	33.5	35	267
MCO_337.527+0.115	337.527	0.115	-120.9	76	93	1.1	76	18	22	7.8	7.8	1.1	1.7	10.3	17.6	50	50
MCO_337.544+0.073	337.544	0.073	-113.6	149	71	1.1	63	13	33	7.0	8.8	0.9	1.1	6.8	12.4	18	29
MCO_337.594-0.410	337.594	-0.410	-42.7	93	59	1.0	63	13	17	3.5	12.2	1.0	1.2	7.5	12.8	5	62
MCO_337.619-0.077	337.619	-0.077	-51.0	156	99	3.1	113	41	49	4.0	11.7	1.1	1.9	21.3	50.1	61	521
MCO_337.635-0.102	337.635	-0.102	-58.4	158	98	2.4	113	41	49	4.4	11.4	1.1	1.6	17.1	34.1	58	392
MCO_337.652+0.131	337.652	0.131	-74.9	188	54	2.0	93	27	32	5.1	10.6	0.9	1.1	8.4	18.8	26	112
MCO_337.669-0.194	337.669	-0.194	-53.8	49	65	1.6	53	9	10	4.1	11.6	1.0	1.4	16.2	23.8	11	86
MCO_337.669+0.281	337.669	0.281	-42.7	383	181	1.1	147	68	218	3.5	12.2	1.0	1.2	8.3	17.9	31	364
MCO_337.677+0.140	337.677	0.140	-49.2	92	108	1.3	93	27	31	3.9	11.8	1.0	1.7	11.1	22.9	20	183
MCO_337.685-0.027	337.685	-0.027	-54.7	98	181	4.4	131	54	56	4.2	11.5	1.0	1.7	22.1	48.4	92	699
MCO_337.685+0.490	337.685	0.490	-83.2	127	127	1.2	100	32	51	5.5	10.2	1.0	1.3	8.0	19.6	33	116
MCO_337.694-0.077	337.694	-0.077	-49.2	143	149	4.3	152	73	67	3.9	11.8	1.2	2.6	35.8	91.4	175	1603
MCO_337.719+0.056	337.719	0.056	-47.3	114	178	4.5	129	52	64	3.8	11.9	1.1	1.7	20.5	61.1	68	669
MCO_337.735+0.023	337.735	0.023	-77.7	128	176	1.6	106	35	71	5.3	10.5	1.0	1.3	10.7	23.9	46	181
MCO_337.794-0.085	337.794	-0.085	-51.0	180	134	3.4	145	67	76	4.0	11.7	1.1	1.8	18.1	43.5	85	730
MCO_337.835-0.394	337.835	-0.394	-41.8	471	332	2.0	298	279	491	3.5	12.2	1.1	2.3	10.1	34.3	152	1862
MCO_337.860-0.035	337.860	-0.035	-92.4	241	61	0.5	93	27	46	5.9	9.9	1.0	1.3	7.1	11.6	29	82
MCO_337.869+0.031	337.869	0.031	-59.3	83	95	0.9	66	14	25	4.4	11.3	1.0	1.3	7.5	12.5	9	57

Table 3. Continued from previous page.

Clump ID	Coordinates		V _{LSR}	Δl	Δb	ΔV	R	A	A _{fwhm}	D ^N	D ^F	$\overline{T}_{\text{MB}}^{18}$	$\widehat{T}_{\text{MB}}^{18}$	$\overline{N_{\text{H}_2}}$	$\widehat{N_{\text{H}_2}}$	M ₁₈ ^N	M ₁₈ ^F
	<i>l</i> deg.	<i>b</i> deg.	km/s	arcsec	km/s	arcsec	10 ³ arcsec ²	10 ³ arcsec ²	kpc	K		10 ²¹ cm ⁻²	10 ²¹ cm ⁻²	10 ²¹ cm ⁻²	10 ² M _⊙	10 ² M _⊙	
MCO_337.877-0.027	337.877	-0.027	-57.4	64	75	1.5	61	12	15	4.3	11.4	0.9	1.0	7.1	12.0	7	48
MCO_337.902-0.494	337.902	-0.494	-41.8	203	187	2.4	157	77	119	3.5	12.2	1.1	2.2	15.6	40.6	65	793
MCO_337.902-0.060	337.902	-0.060	-51.9	172	121	2.1	93	27	66	4.1	11.7	0.9	1.2	9.0	18.7	18	145
MCO_337.919-0.144	337.919	-0.144	-87.8	120	133	1.8	99	31	50	5.7	10.1	1.0	1.4	9.5	21.5	42	130
MCO_337.944-0.219	337.944	-0.219	-42.7	100	75	1.4	78	19	24	3.6	12.2	1.0	1.6	10.0	21.4	11	123
MCO_337.944-0.077	337.944	-0.077	-91.5	86	61	1.6	63	13	16	5.9	9.9	1.0	1.1	9.3	13.8	18	50
MCO_337.969+0.048	337.969	0.048	-40.9	108	194	3.9	136	59	66	3.5	12.3	1.0	1.5	18.5	43.7	57	718
MCO_337.977+0.040	337.977	0.040	-76.8	50	54	1.5	48	7	9	5.2	10.5	0.9	1.2	11.6	17.1	10	41
MCO_337.985+0.048	337.985	0.048	-124.6	88	100	1.4	90	25	28	7.8	7.8	1.2	1.9	12.9	25.6	87	87
MCO_337.994-0.119	337.994	-0.119	-87.8	78	57	2.0	63	13	14	5.7	10.1	1.0	1.2	9.3	18.9	17	52
MCO_338.002-0.094	338.002	-0.094	-52.8	165	267	3.6	128	51	139	4.1	11.6	0.9	1.3	8.4	17.5	32	257
MCO_338.002+0.098	338.002	0.098	-74.0	65	126	1.6	74	17	26	5.1	10.7	0.9	1.0	9.4	17.5	18	80
MCO_338.027+0.023	338.027	0.023	-47.3	181	143	2.5	102	32	81	3.8	11.9	1.0	1.3	9.9	21.6	21	201
MCO_338.027-0.052	338.027	-0.052	-56.5	60	110	1.0	63	13	21	4.3	11.5	0.9	1.0	7.0	12.3	7	51
MCO_338.044+0.065	338.044	0.065	-72.2	84	70	1.6	72	16	18	5.0	10.7	0.9	1.2	10.5	19.3	19	86
MCO_338.060-0.002	338.060	-0.002	-40.9	193	258	3.9	228	163	157	3.5	12.3	1.3	3.1	31.6	123.6	271	3428
MCO_338.102+0.156	338.102	0.156	-34.4	107	112	2.2	97	30	38	3.1	12.7	0.9	1.2	11.7	29.1	14	246
MCO_338.110-0.085	338.110	-0.085	-74.0	64	87	1.0	70	15	17	5.1	10.7	0.9	1.2	8.4	13.2	15	64
MCO_338.119-0.169	338.119	-0.169	-89.6	91	55	1.8	58	11	16	5.8	10.0	0.9	1.0	7.7	12.9	12	37
MCO_338.202-0.510	338.202	-0.510	-38.1	172	204	1.9	123	48	111	3.3	12.5	0.9	1.4	7.9	18.7	18	259
MCO_338.285-0.485	338.285	-0.485	-38.1	73	110	1.7	76	18	25	3.3	12.5	0.9	1.1	8.0	12.3	7	99
MCO_338.294+0.106	338.294	0.106	-37.2	306	148	4.0	164	85	142	3.3	12.5	1.0	1.5	16.1	39.1	63	941
MCO_338.377-0.419	338.377	-0.419	-40.0	340	109	1.3	159	79	116	3.4	12.4	1.0	1.6	9.4	20.1	38	500
MCO_338.377-0.002	338.377	-0.002	-40.0	83	52	1.9	58	11	14	3.4	12.4	0.9	1.1	10.5	19.6	6	76
MCO_338.385+0.165	338.385	0.165	-34.4	71	123	1.1	63	13	27	3.1	12.7	0.9	1.1	7.5	13.1	4	67
MCO_338.444+0.006	338.444	0.006	-28.9	115	135	2.8	106	35	49	2.7	13.1	1.0	1.4	13.5	35.3	15	356
MCO_338.460+0.015	338.460	0.015	-41.8	125	103	4.5	121	46	41	3.5	12.3	1.1	1.6	25.2	64.2	64	767
MCO_338.544-0.019	338.544	-0.019	-97.0	120	115	1.7	81	21	43	6.1	9.7	1.0	1.2	8.8	14.0	30	76
MCO_338.552-0.194	338.552	-0.194	-120.0	76	119	1.7	83	22	29	7.3	8.5	1.1	1.7	11.9	24.1	60	82
MCO_338.577+0.040	338.577	0.040	-21.6	68	67	1.4	61	12	14	2.2	13.7	0.9	1.1	8.8	13.9	2	84
MCO_338.602-0.010	338.602	-0.010	-24.3	126	127	2.1	104	34	50	2.4	13.4	1.0	1.4	12.6	30.9	11	343
MCO_338.635-0.460	338.635	-0.460	-40.9	130	91	1.0	78	19	37	3.5	12.3	0.9	1.1	7.1	12.2	7	90
MCO_338.660+0.148	338.660	0.148	-48.2	147	80	1.3	86	23	37	3.9	11.9	1.0	1.4	8.0	14.0	13	117
MCO_338.677-0.335	338.677	-0.335	-33.5	141	89	0.1	81	21	39	3.0	12.8	1.0	1.2	6.2	7.8	5	92
MCO_338.744-0.360	338.744	-0.360	-47.3	230	174	1.2	133	56	126	3.9	12.0	1.0	1.3	8.0	14.6	29	281
MCO_338.769+0.465	338.769	0.465	-65.7	158	84	2.3	116	42	42	4.8	11.1	1.2	2.0	20.0	44.2	85	455
MCO_338.785-0.469	338.785	-0.469	-41.8	123	58	0.8	72	16	22	3.6	12.3	1.0	1.1	6.8	11.8	6	73
MCO_338.802+0.048	338.802	0.048	-34.4	100	156	2.1	113	41	49	3.1	12.7	1.0	1.6	12.3	27.0	21	356

Table 3. Continued from previous page.

Clump ID	Coordinates		V _{LSR}	Δl	Δb	ΔV	R	A	A _{fwlm}	D ^N	D ^F	$\overline{T}_{\text{MB}}^{18}$	$\widehat{T}_{\text{MB}}^{18}$	$\overline{N}_{\text{H}_2}$	\widehat{N}_{H_2}	M ₁₈ ^N	M ₁₈ ^F
	<i>l</i> deg.	<i>b</i> deg.	km/s	arcsec	km/s	arcsec		10 ³ arcsec ²		kpc	K			10 ²¹ cm ⁻²	10 ² M _⊙		
MCO_338.827+0.431	338.827	0.431	-60.2	90	82	1.1	74	17	23	4.5	11.3	1.1	1.7	13.3	22.1	20	128
MCO_338.835-0.344	338.835	-0.344	-122.8	150	159	2.3	120	45	75	7.5	8.4	1.0	1.4	13.3	29.3	147	183
MCO_338.844+0.398	338.844	0.398	-59.3	90	97	1.8	93	27	27	4.5	11.4	1.3	2.4	19.9	46.0	47	305
MCO_338.852-0.485	338.852	-0.485	-38.1	198	122	1.2	110	38	76	3.3	12.5	1.0	1.2	6.4	11.0	12	165
MCO_338.894+0.348	338.894	0.348	-57.4	103	112	1.1	76	18	36	4.4	11.5	1.0	1.3	8.2	15.2	12	85
MCO_338.910+0.373	338.910	0.373	-27.1	149	93	2.6	113	41	44	2.6	13.2	1.1	1.6	20.4	46.5	25	638
MCO_338.910+0.490	338.910	0.490	-65.7	156	62	2.1	83	22	30	4.8	11.1	1.0	1.3	13.0	26.4	28	151
MCO_338.919-0.510	338.919	-0.510	-38.1	96	82	1.5	81	21	25	3.3	12.5	1.2	2.0	15.7	39.5	16	224
MCO_338.919-0.435	338.919	-0.435	-40.0	317	100	2.0	117	43	100	3.5	12.4	1.0	1.4	7.7	19.1	17	224
MCO_338.969+0.240	338.969	0.240	-57.4	124	66	0.4	78	19	26	4.4	11.5	1.2	1.7	7.9	16.0	13	86
MCO_338.977-0.219	338.977	-0.219	-118.2	235	144	1.1	124	49	106	7.1	8.8	1.0	1.4	8.4	19.8	90	138
MCO_338.994+0.406	338.994	0.406	-59.3	303	308	4.2	187	110	293	4.5	11.4	1.0	1.7	10.1	25.8	98	633
MCO_339.052-0.277	339.052	-0.277	-44.6	251	280	1.5	170	91	222	3.7	12.1	1.0	1.5	9.6	22.2	53	564
MCO_339.052+0.123	339.052	0.123	-82.3	75	112	1.8	85	23	26	5.5	10.4	1.0	1.4	12.5	26.7	37	133
MCO_339.085-0.160	339.085	-0.160	-120.0	103	84	1.8	74	17	27	7.2	8.7	0.9	1.0	7.0	11.7	27	39
MCO_339.102+0.123	339.102	0.123	-81.4	71	77	1.6	70	15	17	5.5	10.4	1.0	1.2	11.1	20.3	22	81
MCO_339.110-0.227	339.110	-0.227	-32.6	75	100	1.5	74	17	24	3.0	12.9	0.9	1.1	7.9	14.1	5	99
MCO_339.119-0.285	339.119	-0.285	-97.0	127	56	0.9	68	14	23	6.1	9.8	1.0	1.3	7.0	13.9	16	42
MCO_339.169-0.410	339.169	-0.410	-40.0	85	57	1.3	63	13	15	3.5	12.4	1.0	1.4	10.0	14.4	7	86
MCO_339.210-0.044	339.210	-0.044	-20.6	89	73	1.7	70	15	20	2.1	13.8	0.9	1.2	10.6	19.4	3	135
MCO_339.227-0.010	339.227	-0.010	-108.0	103	90	1.7	91	26	29	6.6	9.3	1.1	1.4	14.9	25.9	74	149
MCO_339.235-0.435	339.235	-0.435	-40.9	468	164	2.0	229	166	241	3.5	12.4	1.1	1.8	12.4	28.6	113	1376
MCO_339.277+0.340	339.277	0.340	-33.5	67	138	1.4	86	23	29	3.1	12.8	1.0	1.4	10.1	21.3	10	170
MCO_339.460+0.040	339.460	0.040	-19.7	89	98	2.3	72	16	27	2.1	13.8	0.9	1.1	11.5	23.4	4	156
MCO_339.485-0.510	339.485	-0.510	-40.0	222	69	1.7	86	23	48	3.5	12.4	1.0	1.5	6.5	11.9	8	102
MCO_339.535-0.510	339.535	-0.510	-93.3	55	48	2.4	51	8	8	6.0	10.0	1.0	1.6	12.3	28.4	16	44
MCO_339.544-0.152	339.544	-0.152	-37.2	295	143	1.4	188	111	132	3.3	12.6	1.1	1.7	12.6	25.4	68	971
MCO_339.560+0.073	339.560	0.073	-111.7	378	109	2.1	144	65	130	6.7	9.2	1.0	1.6	11.6	34.1	149	280
MCO_339.777-0.044	339.777	-0.044	-25.2	187	69	1.5	94	28	41	2.5	13.4	0.9	1.2	7.8	17.8	6	172
MCO_339.852-0.427	339.852	-0.427	-39.0	163	145	1.3	142	63	74	3.5	12.5	1.1	1.8	11.6	25.7	39	501
MCO_339.910-0.102	339.910	-0.102	-53.8	146	109	2.0	127	50	50	4.3	11.7	1.3	2.4	19.7	55.2	80	597
MCO_339.910+0.065	339.910	0.065	-124.6	101	99	2.2	74	17	31	7.4	8.5	1.0	1.2	9.3	19.7	38	51
MCO_339.952-0.177	339.952	-0.177	-53.8	125	142	1.6	104	34	56	4.3	11.7	1.2	1.9	11.0	22.5	30	226
MCO_339.969-0.444	339.969	-0.444	-90.6	104	97	1.1	94	28	32	5.9	10.1	1.3	2.2	14.6	29.1	61	183
MCO_339.985-0.135	339.985	-0.135	-54.7	85	265	3.6	100	32	71	4.3	11.6	1.1	1.7	13.4	29.5	35	252
MCO_339.985+0.090	339.985	0.090	-26.2	45	192	1.3	81	21	27	2.6	13.4	1.0	1.5	9.3	16.3	6	152
MCO_339.994-0.327	339.994	-0.327	-38.1	41	93	2.8	53	9	12	3.4	12.5	1.1	2.0	12.7	21.4	6	79